UNIVERSITY OF CALIFORNIA
RIVERSIDE

Study of Emergent Quantum Phases in Two-Dimensional van der Waals Materials

A Dissertation submitted in partial satisfaction
of the requirements for the degree of

Doctor of Philosophy

in

Materials Science and Engineering

by

Xiong Huang

September 2022

Dissertation Committee:

Dr. Yongtao Cui, Chairperson
Dr. Jing Shi
Dr. Nathaniel Gabor

The Dissertation of Xiong Huang is approved:

Committee Chairperson

University of California, Riverside

Acknowledgements

I'm very lucky to work in Dr. Cui's group at UC Riverside for the past four years. I arrived at Riverside in a hot summer of August 2018. When I first entered the lab space of room MSE055, a lot of things look so familiar, such as the Nanonis SPM controller and the helium-4 cryostat. My experience in a scanning tunneling microscopy group helps me to quickly fit into the research here. However, there are a lot of new knowledge that I must learn, such as microwave technology and 2D materials. I started to learn the fundamental of microwave knowledge by drawing the schematic diagram for our microwave electronic box of 1 GHz when Dr. Cui asked us to build a box working at 10 GHz. I learnt to do some MIM scanning at the Bruker Dimension Icon system at room temperature. Later, in 2019, I had the chance to work on low-temperature MIM for topological insulator WTe_2 devices. Then we moved to collaborations with UW Seattle and RPI groups at the end of 2019 on two different projects at the same time. Soon we had a flood in the lab at the beginning of 2020 and then came the COVID-19 pandemic in that March. The experience during that time is memorable and so valuable that I started to have some confidence in research. I started to enjoy research since I can manage the time for my measurements, such as maintenance of liquid helium level for the cryostat. Sometimes it was so competitive to conduct research since other groups were working in a same topic. The moment of seeing data with unexpected results is so exciting for me in the lab. It has been such a long journey with so many late-night and weekend working. How time flies that I am writing for my final thesis.

I must express my sincere appreciation for my adviser Dr. Yongtao Cui for his patient guidance and encouragement for all the time. And of course, everything started from the offer which he gave me after our Skype interview in 2017 when I was down to my lowest. From him, I learnt how to ask and approach a scientific question. I wish I could be a person like him in the future.

I would like to thank my parents who always wish me to do well in study and work and, the most important, health and happiness. And to my big family members (such as my sister, my uncle, my aunt, and their families), I do regain a belief for a better life after the phone calls with you. I'm lucky to have so many good friends and classmates whom I met throughout the years. Despite some disagreement, they do respect my decision to start a new graduate study in the US. We will meet again somewhere in the near future.

I want to thank people in Cui's group. Dr. Yanmeng Shi encourages me to apply for Yongtao's group in 2017. Mina helped me lot when I first arrived UCR, and we had a lot of time to learn and work together. For Ben and Brian, I would like to thank them for cooperation on the low-temperature SPM system. I thank Dr. Yadong Xu for his knowledge on 2D devices. For people working in the next door, Dr. Wei Yuan and Tang Su, we had so many times for grocery shopping together and all the funny chats. I would like to thank my best friends, Dr. Erfu Liu and his wife Ms. Hongmei Gao, for all the happy hiking hours and the delicious food served in their apartment. I thank my roommates and my kind landlords. I would like to thank my classmates (especially to Yiqing Chen, Boqun Liang, Ying Chen…) in UCR and good luck to their research. I want to thank for all the people

working in the MSE building who helped me and I know it would be a very long list (to name a few, Jacky, Mark, Jeremiah, Cliff, Jason…).

My great appreciations go to our collaborators. For the first MIM scans on WTe2 samples from Prof. David Cobden and his group members (Bosong Sun, Wenjin Zhao and Elliott Runburg) at UW Seattle. The challenging project on $MnBi_2Te_4$ from Prof. Xiaodong Xu's group, including Dmitry Ovchinnikov, Zhong Lin, Jiaqi Cai, Zaiyao Fei, Tiancheng Song, Minhao He and others. For the TMD moire experiments, I thank for support from Prof. Sufei Shi and his group members, Shengnan Miao, Tianmeng Wang, Dongxue Chen, Zhen Lian, Zhipeng Li, Yuze Meng and other new members there. For theoretical support, my thanks go to Prof. Di Xiao and Dr. Chong Wang. On the graphene moire image project, I thank Prof. Z. X. Shen and his MIM research group and Prof. Haomin Wang and his graphene growth group (Lingxiu Chen and Shujie Tang). Forgive me if I miss any names here.

At last, I would like to thank the professors I met in UCR. For Prof. Joshua Lui, Igor Barsukov, Nathaniel Gabor, Jing Shi, Peng Wei, Kirill Shtengel, Ran Cheng, Ming Liu, Ruoxue Yan and many others. Special thanks to Prof. Joshua Lui, Nathaniel Gabor, Jing Shi and Ran Cheng for acting as my Oral Qualifying Committee members.

Of course, I won't finish my research study without the funding resources, including a seed fund from SHINES (an EFRC from DOE), NSF and Hellman Fellowship through supporting Dr. Cui.

June 6, 2022

Xiong Huang

Acknowledgement of Previously Published Materials

(† Equal contribution; * Corresponding author)

1. **Xiong Huang**†, Tianmeng Wang†, Shengnan Miao†, Chong Wang†, Zhipeng Li, Zhen Lian, Takashi Taniguchi, Kenji Watanabe, Satoshi Okamoto, Di Xiao*, Su-Fei Shi*, Yong-Tao Cui*, *Correlated Insulating States at Fractional Fillings of the WS_2/WSe_2 Moiré Lattice*, ***Nature Physics*** 17, 715–719 (2021).

2. Shengnan Miao†, Tianmeng Wang†, **Xiong Huang** †, Dongxue Chen†, Zhen Lian, Chong Wang, Mark Blei, Takashi Taniguchi, Kenji Watanabe, Sefaattin Tongay, Zenghui Wang*, Di Xiao, Yong-Tao Cui*, Su-Fei Shi* *Strong Interaction between Interlayer Excitons and Correlated Electrons in WSe_2/WS_2 Moiré Superlattice*, ***Nature Communications*** 12, 3608 (2021).

3. **Xiong Huang** †, Lingxiu Chen†, Shujie Tang, Chengxin Jiang, Chen Chen, Huishan Wang, Zhi-Xun Shen, Haomin Wang, Yong-Tao Cui*, *Imaging Dual-Moiré Lattices in Twisted Bilayer Graphene Aligned on Hexagonal Boron Nitride Using Microwave Impedance Microscopy*, ***Nano Letters*** 21 (10), 4292-4298(2021).

4. Dmitry Ovchinnikov†, **Xiong Huang**†, Zhong Lin†, Zaiyao Fei†, Jiaqi Cai, Tiancheng Song, Minhao He, Qianni Jiang, Chong Wang, Hao Li, Yayu Wang, Yang Wu, Di Xiao, Jiun-Haw Chu, Jiaqiang Yan*, Cui-Zu Chang*, Yong-Tao Cui*, Xiaodong Xu*, *Intertwined Topological and Magnetic Orders in Atomically Thin Chern Insulator $MnBi_2Te_4$*, ***Nano Letters*** 21 (6), 2544-2550(2021).

5. Dongxue Chen†, Zhen Lian†, **Xiong Huang**†, Ying Su†, Mina Rashetnia, Lei Ma, Li Yan, Mark Blei, Li Xiang, Takashi Taniguchi, Kenji Watanabe, Sefaattin Tongay, Dmitry Smirnov, Zenghui Wang*, Chuanwei Zhang*, Yong-Tao Cui*, Su-Fei Shi*, *Excitonic Insulator in Heterojunction Moiré Superlattice*, accepted by ***Nature Physics***.

6. Dongxue Chen†, Zhen Lian†, **Xiong Huang**†, Ying Su†, Mina Rashetnia, Li Yan, Mark Blei, Takashi Taniguchi, Kenji Watanabe, Sefaattin Tongay, Zenghui Wang, Chuanwei Zhang*, Yong-Tao Cui*, Su-Fei Shi*, *Tuning Moiré Excitons and Correlated Electronic States through Layer Degree of Freedom*, under review in ***Nature Communications***.

The co-author, Yong-tao Cui, listed in all publications directed and supervised the research by which forms the basis for this dissertation.

ABSTRACT OF THE DISSERTATION

Study of Emergent Quantum Phases in Two-Dimensional van der Waals Materials

by

Xiong Huang

Doctor of Philosophy, Graduate Program in Materials Science and Engineering
University of California, Riverside, September 2022
Dr.Yongtao Cui, Chairperson

The discovery of one-atom thick graphene layer has marked the starting era of two-dimensional (2D) van der Waals (vdW) materials. Since then, various electronic properties, such as semi-metal, semiconductor, insulator, superconductor, and magnet, have been discovered with materials in the 2D form. Recently, with the rapid development in device fabrication, artificial superlattices can be created using building blocks of 2D materials. This offers researchers novel control over materials to create novel quantum states which do not exist in their bulk parent. These emergent materials offer better tunability compared with their bulk relatives, such as carrier density tunning, band structure and topology engineering.

One seminal work is the observation of unexpected strong correlation effect and superconductivity in ~1.1° twisted bilayer graphene in 2018. A rising research field, moiré physics, has emerged as a platform for quantum simulation. Flat electronic bands can form in these twisted 2D samples, which can give birth to various interesting quantum

phenomena, for example, superconductivity, Mott insulators, ferromagnetism, and quantum anomalous hall effect. In this thesis, I will summary our efforts in studying moiré physics using microwave impedance microscopy (MIM), including direct visualization of the moiré pattern in graphene-based heterostructures and observation of correlated insulating states at fractional carrier fillings in a WSe_2/WS_2 moiré superlattice. Our results demonstrate MIM as a powerful tool towards exploring emergent quantum states in such semiconducting moiré superlattices. We further explore correlated electronic states and moiré exciton in the TMD moiré system with layer degree of freedom. A robust excitonic insulator has been observed in 1L/2L WSe_2/WS_2 moiré superlattice with the population of correlated electron-hole pairs in different WSe_2 layers. Another highly pursued topic is searching for intrinsic magnetic topological insulators (TI) where topology meets magnetism. Together with transport measurements and magnetic characterization, we perform MIM study on $MnBi_2Te_4$ thin flakes which is predicted as an intrinsic magnetic TI. This material provides a good platform to study the interplay between magnetic state and topological order in this material. The band crossing effect together with the emergence of topological edge states are observed during the magnetic-field driven topological phase transition. Our results highlight the importance of combination of multi-modal probes to determine the magnetic state, topological order, and bulk electronic property in a magnetic topological insulator.

Contents

List of Figures

List of Tables

Chapter 1 Introduction

Since the successful isolation of monolayer graphene and the demonstration of quantum Hall effect, research on two-dimensional (2D) van der Waals materials have been in the spotlight. Using such a simple Scotch tape method, extremely high quality 2D layers can be obtained to realize various quantum phases. Stimulated by this discovery, research along this direction has been focused on obtaining exotic 2D layers through either top-down (mechanical exfoliation) or bottom-up (e.g., chemical vapor deposition or molecular-beam epitaxy) methods. Compared with the demanding chemical doping in a bulk material, it's quite simple to use electrical gates to tune the carrier density in a 2D layer. Besides, electronic properties of 2D materials are susceptible to strain effect with practical pressure. Electronic states, such as semi-metal, semiconductor, insulator, superconductor, magnet, and topological insulator have been realized in the 2D form. Soon after that, the idea of making heterostructures using these 2D layers have emerged which can further expand our knowledge of how electrons interact and new phases of matter manifest.

Creating heterostructures can have several benefits. Combining materials of different electronic properties could lead to observation of exotic quantum phases. For example, an interface coupling of 2D magnets with spin-orbit coupling could induce an interfacial Dzyaloshinskii-Moriya interactions and give birth to a topologically protected spin textures, named skyrmions. Skyrmions hold promise for high-density and low-energy-consumption information processing devices. The introduction of magnetism into a topological insulator has the potential to realize quantum anomalous Hall effect with

dissipationless edge conduction. Research along these directions have been focused on realization of these emergent phases at higher temperatures as required by applications.

Making heterostructures can generate a moiré pattern which could strongly modulate the electron-electron interaction in the system. A moiré superlattice can be generated by twisting two layers of a same material or stacking two different layers without a twist. It's the periodic alignment of atoms in the two constituent layers and the interlayer hybridization will create a periodic potential for charges. It has been demonstrated in a "*magic-angle*" twisted bilayer graphene system, that interaction-induced insulating states and superconductivity can be achieved. The moiré superlattice generates flat moiré energy bands for electrons and strongly enhances the electron-electron interaction. Band topology can also be modified during the moiré band engineering process. Thus, moiré heterostructures have been proposed and demonstrated as a quantum simulator to realize various quantum phases on demand.

These exotic quantum phases in 2D heterostructures naturally have pronounced electronic inhomogeneity due to strong electron-electron interactions and competing between electronic orders. Also, the current fabrication technique will induce defects which might easily destroy the interested electronic order. Especially, in moiré heterostructures based on 2D van dar Waals semiconducting layers, the large electrode-sample contact resistance has posed challenges for direct resistance measurement using electronic transport. To probe the elusive quantum states, a study with sufficient spatial resolution and getting rid of the extrinsic factors (such as fabrication artifacts) is highly desired.

Nowadays, scanning probe methods have been widely used to probe sample electronic properties at the nanoscale. Among them, scan microwave impedance microscopy (MIM) has been under rapid development to measure local sample conductivity and permittivity. In its unique reflection-type measurement, minimum sample preparation is required. The same experiment instrumentation as traditional atomic force microscope makes it readily to be incorporated in a scanning probe platform. These could greatly promote MIM in sample characterization process. With its capability to probe sample electronic properties at the nanoscale, scanning MIM has been successfully demonstrated to study 2D emergent quantum phases.

Here, in my graduate study, I've working on study of various 2D quantum materials using scanning MIM. I will first talk about fundamental concepts and the instrumentation in MIM. In Chapter 3, I will talk about our research to image dual-moiré pattern in a tri-layer stack graphene-based moiré heterostructures. We demonstrate a high spatial resolution (<2 nm) MIM imaging technique which will strongly benefit the research in moiré physics. Then (Chapter 4) I will present our study of correlated insulating states in a semiconducting moiré superlattice. The observed correlated insulating states at fractional fillings of the moiré superlattice suggests unexpected strong and long-range electron-electron interactions in this system and prominent modulation of the optical properties for the material. In the Chapter 5, I will focus on our recent research about tuning moiré excitons and correlated electronic states through layer degree of freedom in 1L/**M**L (**M** = 1,2,3) WS_2/WSe_2 heterojunctions. Our study demonstrates the highly interfacial nature of the moiré potential and the electronic correlation strength can be tuned by additional WSe_2

layers. In Chapter 6, we report the observation of a correlated excitonic insulator phase in 1L/2L WS_2/WSe_2 moiré superlattices. At a total half filling of the moiré superlattice, the coexistence of electrons and holes in two separate WSe_2 layers has been confirmed by optical measurements. The insulating nature of this new phase has been studied by MIM in single-gated or dual-gated devices where a new dual-gated device structure has been utilized. In the Chapter 7, I will talk about our MIM study (collaborated with transport measurements and magnetic characterization) on an emergent intrinsic magnetic topological insulator. Our work highlights the importance of the interplay between topological and magnetic order in this system. A clear observation of band crossing effect and topological conduction marks the topological phase transition during the magnetic-field induced magnetic state evolution. In the last Chapter, I will briefly talk about our recent progress of MIM work in dual-gate device and have some outlook of what this enables us to explore systems with additional control knobs—electric displacement field.

Chapter 2 Scanning Microwave Impedance Microscopy

Revolution in materials has helped to expand the limits of human endeavor and achievement. Recent advances in quantum materials have demonstrated promising potentials to enable next-generation technology for information storage and processing. The key is to harvest the quantum nature of electronic states in novel material systems through investigating the fundamental physics and exploring new methods to manipulate their properties. Since the successful isolation of monolayer graphene, two-dimensional (2D) van der Waals (vdW) materials have become a wonderful playground to realize various emergent quantum phenomena beyond conventional understandings. Its reduced dimensionality confines electronic states strictly into two dimensions, significantly enhancing the quantum nature, and the weak vdW interlayer coupling further allows new possibilities to form and control novel device structures, for example, by stacking multiple vdW monolayers to assemble a heterostructure. My research toward the PhD degree has been focused on the study of 2D electronic states using scanning probe microscopy. I mainly use scanning microwave impedance microscopy (MIM) to investigate the quantum states on the nanoscale. This chapter is by no means a comprehensive knowledge of the MIM technique, and the interested readers are referred to Ref [1–6].

2.1 Fundamentals of Microwave Impedance Microscopy

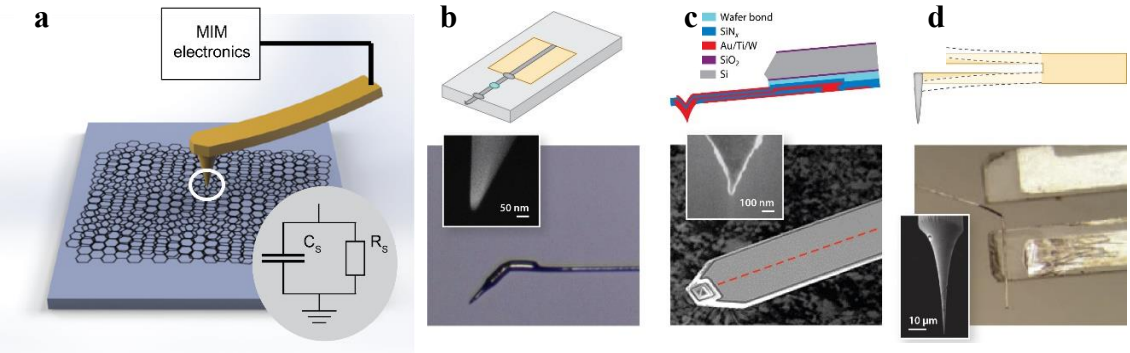

Figure 2.1 Scanning MIM and probes. a, A simple schematic for scanning MIM measurement. Three commonly used MIM probes: **b**, Rocky Mountain probe; **c**, stripline-type MIM probe. **d**, Quartz tuning fork based MIM probes. Panel **b** adapted with permission from REF 2, Annual Reviews. Panel **c** adapted with permission from REF 13, copyright IOP Publishing; Panel **d** adapted with permission from REF 7, copyright IOP Publishing.

Microwave is an electromagnetic radiation defined with a frequency ranging from 300 MHz to 300 GHz and a wavelength of 1 m to 1 mm. The photon energy for a microwave is ranging from 1.24 ueV to 1.24 meV which is very small compared with the optical excitations. Thus, the interaction between microwave radiation and materials is more like a classical process. The electric response of the material to the external ac fields is characterized by the complex permittivity ε:

$$\varepsilon = \varepsilon' + i(\varepsilon'' + {}^{\sigma}/_{\omega})$$

Where ε' and $\varepsilon^{"}$ are the real and imaginary parts of the dielectric constant, σ is the conductivity and $\omega = 2\pi f$ is the angular frequency. In MIM (Fig. 2.1a), a sharp metallic tip is brought into proximity to the sample's surface with an applied microwave voltage. An ac coupling between the tip and sample can induce periodic dielectric polarization or local currents (on the nanoscale) to flow under the tip in the sample. The displacement current with a magnitude and phase is determined by the tip-sample admittance (defined

as $Y = 1/Z$, the inverse of impedance). An ac measurement of the tip-sample admittance can provide local information of the material, such as the dielectric and conductive properties. This is particularly useful as a direct resistance measurement (current against voltage) is not available in situations when achieving a low tip-sample contact resistance is challenging (Schottky barrier at the contact region) or unavailable (protective insulating layer on top of sample surface).

In a scanning MIM measurement, a typical tip size (~100 nm) is orders of magnitude smaller than the microwave wavelength. In the microwave near-field regime (in the quasi-static limit), the tip-sample admittance can be descripted by a lump-element model as shown in the inset of **Fig. 2.1a**, where the imaginary part (capacitance C) and the real part (1/R) depend on the sample electric properties. Specifically, C and 1/R are proportional to ε' and σ, respectively. In typical measurements, the optimal frequency ω is determined when the imaginary and real admittance are comparable [3]:

$$\omega C \approx {}^{1}/_{R} \;\rightarrow\; \omega\varepsilon' \approx \sigma.$$

For materials with a typical resistivity ($1/\sigma$) ranging from 10 to $10^5\ \Omega\cdot$cm and $\varepsilon'\sim 1-10\varepsilon_0$, the optimal measuring frequency is within the microwave frequency range of $0.1-10$ GHz [1]. From the equation above, a higher frequency should be used to probe a larger sample conductivity.

2.1.1 MIM Probe Design

Traditional metallized atomic force microscopy (afm) probes (unshielded) have a large stray field coupling between the cantilever body and surrounding environment. The contributed large admittance will dominate the tip-sample admittance of our research

interest and thus need to be eliminated by special probe design. There are different ways to circumvent this problem. Micro-fabricated multilayer-structure cantilevers consisting of a fully shielded microwave stripline (see **Fig. 2.1c**) have been successfully employed in MIM measurements and they are commercially available[1]. As shown in **Fig. 2.1b**, special conductive afm probes with a tall shank of a metal tip[2] can mitigate the stray field coupling. A tuning-fork based bare metal tip (**Fig. 2.1d**) has also been used with a high-aspect-ratio to minimize the stray field coupling [7]. The first two probes are readily compatible with commercial afm scanning control systems as they share the same cantilever design. For the tuning-fork based probe [8], its self-sensing capability and high quality factor have enabled excellent performance in MIM measurements especially in a cryogenic environment [7].

2.1.2 Impedance Matching and Measurement Schematic

The tip-sample admittance is usually measured in a reflection mode (transmission-mode MIM has been demonstrated can be found in Ref [9]). A microwave excitation is routed to the metal probe and the reflected signal which is due to the change in tip-sample admittance is used to generate the MIM signals[3]. In the transmission of a microwave, there will be some power loss in the form of reflection due to any unbalanced impedance at any point. For a uniform transmission line, the characteristic impedance is always Z_0 (usually 50 Ω) which is defined by the ration of the amplitudes of the voltage and current along that line. The reflection coefficient Γ at a joint point between a uniform transmission line and a load impedance (Z_L) will be

[1] From PrimeNano Inc.
[2] From Rocky Mountain Nachnology LLC.
[3] In-phase (MIM-Re) and out-phase (MIM-Im) as discussed later.

$$\Gamma = \frac{Z_L - Z_0}{Z_L + Z_0}. \qquad \text{(Note [4])}$$

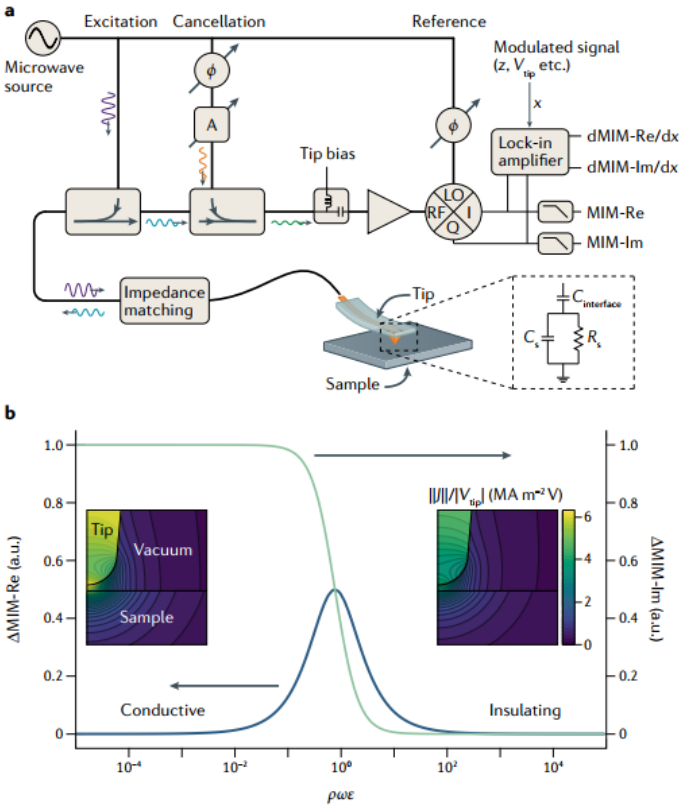

Figure 2.2 MIM circuits and response curves. a, A detailed (but still simplified) schematic overview for MIM measurement. **b**, Simulated MIM response curves as a function of sample resistivity ρ. Panel **a** and **b** adapted with permission from REF 1, copyright Springer Nature.

The reflected power P can be calculated as $P \propto \Gamma^2$. By solving the equation of $\frac{\partial P}{\partial Z_L} = 0$, we learn that the change in the flection for a given small change in Z_L is largest when $Z_L = Z_0$. To maximize the microwave power at the tip-sample junction, an impedance matching network will be used to transform the probe's impedance close to Z_0 to enhance the measurement sensitivity. Details about the matching network for probes we

[4] See appendices at the end of this chapter for characteristic impedance for a transmission line and impedance matching.

used will be discussed in **Section 2.2**. **Figure 2.2a** shows the detailed schematic overview for a MIM measurement while some parts[5] will be inside the cryostat in low-temperature measurements. By using directional couplers, the reflected signal is isolated from the input. A cancel signal (both magnitude and phase can be tunable) will be added to exclude any background signal before reaching the amplifier for higher gain. The amplified signal is further demodulated using an IQ mixer to generate two MIM channels (MIM-Im and -Re). The function of the IQ mixer can be considered as a lock-in amplifier working at microwave frequency with a reference signal (generated directly from the microwave source) to distinguish the in- and out-phase components. A further low-frequency modulation in the tip-sample admittance can be introduced by modulating tip-sample distance Z_{ts} or sample carrier density with an ac gate voltage V_{gate}, *etc*. Then the modulated MIM signals are demodulated by a lock-in amplifier to obtain a robust MIM measurement against any background signal drift.

2.1.3 Understanding MIM Signals

In general, MIM probes have a large overall self-admittance which is much larger than the tip-sample admittance ($Y_{probe} \gg Y_{t-s}$). The overall self-admittance of the probe Y_{probe} is constant during scanning. Thus, the MIM-Im/Re signals are good indicators for the imaginary/real variations of tip-sample admittance [4]. A direct correspondence is established with a known proportionality constant (amplified constant). The two parts (Y_{probe} and Y_{t-s}) are in parallel configuration and the total admittance of the probe-sample

[5] These include the sample and tip with matching, two directional couplers, a bias tee, and a low-temperature preamplifier.

Y_{total} is basically a summation, i.e., $Y_{total} = Y_{probe} + Y_{t-s}$. With an impedance matching network, Y_{total} is transformed to $Y_0 = 1/Z_0$ to enhance the measurement sensitivity. We can refer the admittance after the introduction of a matching network to be $f_{mat}(Y_{total})$. The reflection coefficient can be calculated as the following

$$\Gamma = \frac{Z_L - Z_0}{Z_L + Z_0} = \frac{{}^{1}/_{f_{mat}(Y_{total})} - {}^{1}/_{Y_0}}{{}^{1}/_{f_{mat}(Y_{total})} + {}^{1}/_{Y_0}} = \frac{Y_0 - f_{mat}(Y_{total})}{Y_0 + f_{mat}(Y_{total})}.$$

We define the MIM signal as M, the incident microwave signal as A (both are complex with an amplitude and a phase). Thus, the measured MIM signal can be obtained as

$$M = A \cdot e^{i\phi} \cdot \Gamma = Ae^{i\phi} \cdot \frac{Y_0 - f_{mat}(Y_{total})}{Y_0 + f_{mat}(Y_{total})},$$

where ϕ is the phase difference with respect to the input signal and will be pre-determined as a constant in the measurement. What really matters here is the reflection coefficient Γ as a function of Y_{t-s}. With $Y_{total} \approx Y_0$ and $Y_{probe} \gg Y_{t-s}$, an approximation for the MIM signal can be expressed as

$$M = A \cdot e^{i\phi} \cdot \Gamma\left(Y_{probe} + Y_{t-s}\right) \approx A \cdot e^{i\phi} \cdot [\Gamma\left(Y_{probe}\right) + \Gamma'|_{Y=Y_{probe}}(Y) \cdot Y_{t-s}],$$

$$M \approx C_{gain} \cdot Y_{t-s} + const.$$

where C_{gain}depends on the actual experimental setup (consisting of any amplifier used) and is a constant. Thus, the imaginary (MIM-Im) and real (MIM-Re) parts of M are linearly proportional to the imaginary and real parts of the Y_{t-s}, respectively. The variation of the tip-sample admittance can be measured as

$$\Delta(\mathrm{MIM-Im}) = C_{gain} \cdot Im(\Delta(Y_{t-s})),$$

$$\Delta(\mathrm{MIM-Re}) = C_{gain} \cdot Re(\Delta(Y_{t-s})).$$

A quantitative correlation of the tip-sample admittance Y_{t-s} to the local complex permittivity $(\varepsilon' + i(\varepsilon'' + {}^{\sigma}/_{\omega}))$ can be hard in the solution to a Maxwell's equations with

correct boundary conditions and requiring a highly symmetric geometry for the tip and sample. With the modern computation power, using finite-element analysis (FEA) methods, it's now practical to directly compute the tip-sample admittance in the quasi-static limit for arbitrary tip-sample geometry [10]. Instructions on performing a FEA analysis can be found elsewhere [6]. A numerical determination of the tip-sample admittance can be calculated as a function of the local sample properties, such as the local conductivity[6], which we refer as the microwave response curves as shown in **Fig. 2.2b**. Within the dynamical sensing range, the MIM-Im signal increases monotonically with respect to the local conductivity, while the MIM-Re signal peaks at an intermediate conductivity value. The general shape of the response curves can be qualitatively understood in the following way. When the sample is highly insulating (a low conductivity), it acts as a good dielectric material and the admittance is dominated by the capacitance part. The electric field can easily penetrate the sample and the admittance is low. With an increasing conductivity, the screening of the microwave electric field becomes more evident as oscillation current can be induced. The sample effectively couples to the tip apex and forms a large capacitance, leading to a high tip-sample admittance at the high conductivity limit. In the range of intermediate conductivity, the dielectric energy loss in the material will be maximized and this leads to a MIM-Re peak value. When the sample becomes very conductive, the microwave electric field is completely screened by the sample and the overall energy dissipation is minimum at this limit. Particularly, the MIM-Im channel is a good qualitatively measure of the local

[6] For the quantum materials we are interested in, conductivity variations are most prevalent.

conductivity: a higher/lower MIM-Im signal indicates a larger/smaller local conductivity in the sample.

To be pointed out that, the spatial resolution for an MIM measurement is determined by the profile of the microwave electric field between the tip and sample. It depends on the tip apex geometry and can be estimated in the FEA simulation for a given sample structure.

2.2 MIM Instrumentation

2.2.1 Experimental Setup for a Cryogenic MIM Measurement

A schematic diagram for the actual instrumentation used in our research is similar as that in **Fig. 2.2a**. The scanning head (including tip and sample), impedance matching network, two directional couplers, bias Tee and a low-noise pre-amplifier are placed under cryogenic temperature. A helium-4 cryostat (base temperature ~2.5 K [7]) with a superconducting magnet (a maximum vertical B field at 9 T) is used for the measurements at cryogenic temperature. The system has a commercial SPM control platform (Nanonis RC5). The matching network is usually attached to the probe itself. To achieve high signal-to-noise performance, a high-gain HEMT preamplifier[8] (working at 0.3-14 GHz) is placed inside the cryostat. We have made two microwave electronics working at 1-3 GHz and 5-12 GHz, respectively. After the second-stage microwave amplifier, the signal is further

[7] The sample is cooled by helium exchange gas to a typical temperature around 8 K. It can reach the base temperature with pumping the "1K-pot" space and keeping the needle valve open.
[8] A high-electron-mobility-transistor (HEMT).

amplified in the DC stage before entering a low-frequency lock-in[9] to generate the MIM-Im and MIM-Re signals.

2.2.2 MIM Electronics [6]

The instrumental gain is 106 dB ($2x10^5$) at 1kHz bandwidth. Assuming an input power of -20 dBm, a 1aF capacitance change at the tip produces ~30 mV in the input:

$$\Delta v_{Out} = v_{in}^{+} \cdot \Delta S_{11} \cdot G = 22\, mV_{rms} \cdot 7 \times 10^{-6} \cdot 2 \times 10^{5} = 30 \text{ mV}$$

2.2.3 Tuning Fork Based MIM Probes

Scanning MIM with its capability to characterize the local electronic properties of a sample strongly relies on the MIM probe development. Commercial stripline-type cantilevers have been widely used in contact-mode scanning MIM measurements which requires applying a large force to maintain the tip-sample contact. Besides the common tip wearing effect in the contact-mode measurement which strongly affect the MIM signals, there are other considerations which should be considered. As a large background signal is nulled out with a common-mode cancellation, the obtained MIM signals are just a measure of the relative change in the admittance rather than the absolute value. The background signal may drift overtime and is susceptible to temperature or other experimental variations (such as applied magnetic field). Obtaining a direct measure of the local sample permittivity in a drift-free and more reliable way has been demonstrated in tapping-mode MIM measurements. In tapping-mode measurements, the tip is excited to oscillated near its resonance. Thus, a modulation of the tip-sample admittance is introduced and the demodulated MIM signals are thus robust against background drift and are good indication

[9] Depends on the frequency of the modulation. In tunning-fork based MIM, it's the resonance frequency (~32.7 kHz) of the quartz.

of the absolute admittance. Stripline-type cantilever probe requires an additional laser deflection feedback loop to control the force applied and thus tip-sample oscillation. Due to the multi-layer structure, it is just a fair oscillator with a limited quality factor. This strongly limits its sensitivity to small vibration in tip-sample interaction or other experimental variations (thermal expansion effect or relaxation under an applied magnetic field).

Recently, the idea of quartz tuning fork (TF) based tapping mode scanning [8,11] has been introduced in alternative MIM measurements [7]. Quartz tuning fork, a single crystal with piezoelectric effect, has very low internal dissipation during resonant oscillation and an extremely high quality factor Q can be achieved[10]. With its self- sensing capability, a good MIM performance can be achieved in a stable fashion. Furthermore, it can be incorporated into a scanning tunneling microscopy setup since they share a similar structure.

[10] With a metal wire attached on one prong, the Q can be high as 200 000 in vacuum at low temperatures.

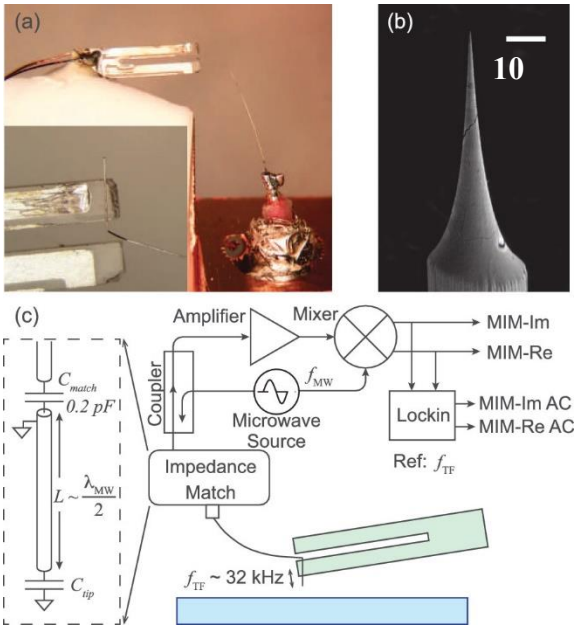

Figure 2.3 TF-based MIM probe and circuits. a, Image for a tuning fork based MIM probe. **b**, SEM image for the tip apex. **c**, circuit diagram with impedance matching for this probe. Panel **a-c** adapted with permission from REF 7, copyright IOP Publishing.

MIM probe based of this type consists of a small diameter metal wire which is glued to the end of one prong of the quartz TF as shown in Fig. 2.3. Following the commonly used chemical etching method[11], a tungsten tip with a sharp apex has been used (Fig. 2.3b) and the special geometry with a large aspect ratio will strongly suppress the stray coupling between the tip and its surroundings. The other end of the wire is soldered to the center conductor of a transmission line (a semi-rigid coax cable). The coax cable is connected to the microwave circuits via a small capacitor (~0.2 pF) in series[12]. An impedance matching network is formed by the formation of a half-wavelength resonator with the metal wire, the coax cable, and the series capacitor (Fig. 2.3c). The microwave electric field will be

[11] Tungsten wires (25 um diameter) with gold coating are etched in KOH solutions (~1 mol/L) with DC ~1.2 V.

[12] A large surface-mount resistor (100 Mohm) has been placed in parallel to the capacitor to enable a DC voltage applied to the metal tip if needed.

maximized at the tip apex and enhance the sensitivity of tip-sample admittance. The length of the tungsten wire is ~10 cm and a fundamental resonant frequency of ~1.07 GHz is achieved. Higher-order resonances such as ~10 GHz have been used to probe samples with a conductivity higher than the dynamic sensing range of 1 GHz. A similar matching network can be used for probes from Rocky Mountain LLC since the cantilever here is made from a metal wire.

A quartz tuning fork consists of two prongs connected at one end and form a resonator with its resonance frequency determined by its geometry [12]. The first fundamental oscillation is a symmetric motion of the two prongs in the plane of the tuning fork (~32 kHz). Quartz crystal is a piezoelectric material which can generate mechanical oscillation under an electric excitation and conversely, generate electric charges by the mechanical deformation. The quartz we purchased has a pair of prepared electrodes on its surface with special patterns. Applying an ac voltage (close to resonance frequency) to one electrode will introduce resonant motion of the prongs and the mechanical deformation will generate an electric current at the other electrode. The actual magnitude of the mechanical oscillation is proportional to the current value. The TF current signal can be detected by using a transimpedance (current to voltage) amplifier. The converted voltage signal is further fed to a phase-locked loop amplifier for the track of the minute change of the resonance (usually resonant frequency shift) as the tip is interacting with sample surface. With a feedback control, a fixed positive resonance frequency-shift (~1 Hz out of

32.5 kHz) will maintain the tip-sample interaction with a constant repulsive force[13]. In our low-temperature measurements, we usually set the tip oscillation with an amplitude of ~7 nm with a closest tip-sample distance of ~2 nm using such a control system. By modulation the tip-sample distance, the MIM signals will also be modulated at the resonant frequency and are further demodulated by a lock-in amplifier. Throughout the research in this thesis, we simply refer the MIM-Im and MIM-Re are the demodulated MIM signals, which are good indicators of the absolute tip-sample admittance.

2.2.4 Matching Network for Stripline-Type Probe

The matching network for the stripline -type MIM probe can be found elsewhere [6] (see **Fig. 2.4**). For the configuration we use a stub tuning impedance matching as shown in **Fig. 2.4g**. We choose a quarter wavelength ($\lambda/4$) transmission line attached directly to the probe. An open-end tuning stub is used and trimming the stub cable in length will select desired matching frequency. A successful matching network will require any joint places to be minimized to reduce unnecessary reflection.

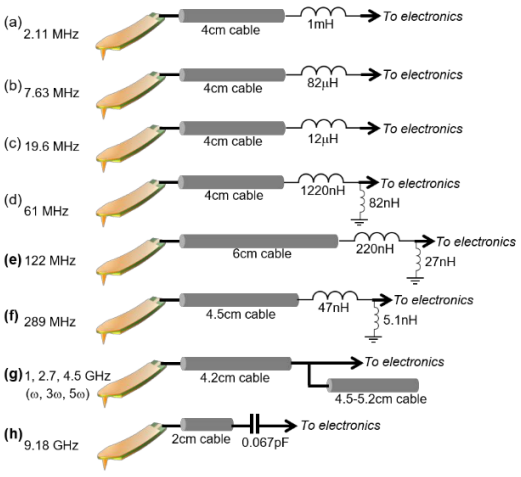

Figure 2.4 Matching networks for stripline-type MIM probe. Impedance matching network of different frequencies for a stripline-type MIM probe. Panel **a-h** adapted with permission from REF 6, copyright Xiaoyu Wu, University of Texas, Austin.

[13] In frequency-modulated atomic force microscopy, a repulsive tip-sample force will usually shift the resonance to a higher value.

2.2.5 Locating 2D Material Thin Flakes

After placing the sample and MIM probe in the insert, we will use an optical microscope to locate the sample in air by approaching the tip towards sample and moving the sample stage in XY-scan plane. Once the tip finds the sample as shown in the image of the microscope, it will be withdrawn by a certain amount of distance. The whole insert will be closed by a can and load into the cryostat. Once reaching helium temperatures, we will manually approach the tip by another amount of distance and leave the rest of the tip-sample gap to be finished by automatically approaching (typical auto-approach in SPM). Usually, the tip will land the sample chip with an xy-plane distance of about several um as we align at room temperature due to thermal drift during cooling.

2.2.6 MIM Measurement for Scan Images and Point Spectroscopy

The most important thing for a MIM measurement is to determine the phase for the MIM-Im and MIM-Re channels. This can be done by scanning the tip between a very conductive region (metal contact) or very insulating region (SiO2/Si substrate). From the conventional MIM response curves, we know that the contrast only shows in MIM-Im channel but not in MIM-Re. By changing the phase of the microwave reference signal to the IQ-mixer, this condition can be met, and the calibration is acquired. During an MIM measurement, a spatial scan can be obtained to visualize inhomogeneity in the local electronic properties. In a sample device incorporated with electrostatic gating, carrier density can be tuned, and a series of spatial images will provide spatial evolution of electronic states of the sample. Point spectroscopy can also be measured by parking the tip at selected positions. MIM signals will be recorded with variation of experiment

parameters, such as carrier density and temperature. In point spectroscopy measurements, a calibration can also be done by changing the reference phase to fulfill the requirement of the response curves by taking the MIM data when sample are very conductive or very insulating as reference points.

Appendices

Waveguides – Transmission Line and Characteristic Impedance[14]

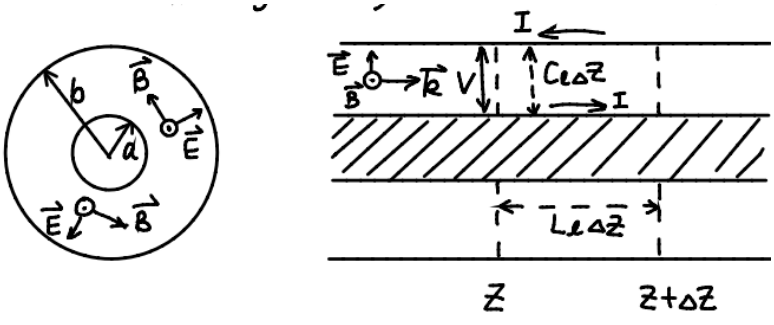

A transmission line consists of a center conductor and an outside shielding layer, such as a coaxial cable geometry. Define the direction for E and B. V is voltage difference between the two conductors. I is the current flowing in the conductor (reverse in the outside). c_u and l_u are the capacitance and conductance per unit length. For a short section of transmission line from z to $z + \Delta z$. V and I will be functions of z and t (time). During a short time interval Δt, there will be changes on the conductors. For inner conductor,

$$\Delta q = I(z)\Delta t - I(z + \Delta z)\Delta t = -\frac{\partial I}{\partial z}\Delta z \Delta t$$

Change in q will induce a change in V due to the capacitance:

$$\Delta q = c_u \Delta z \Delta V$$

[14] From YT Cui's class notes.

$$c_u \Delta z \Delta V = -\frac{\partial I}{\partial z} \Delta z \Delta t$$

$$\frac{\partial V}{\partial t} = -\frac{1}{c_u} \frac{\partial I}{\partial z}$$

Considering the self-inductance, the change in I over time will induce a change in V over distance:

$$V(z + \Delta z) - V(z) = -l_u \frac{\partial I}{\partial t} \Delta z$$

$$\frac{\partial V}{\partial z} = -l_u \frac{\partial I}{\partial t}$$

Combine both equations,

$$\frac{\partial^2 V}{\partial z^2} = l_u c_u \frac{\partial^2 V}{\partial t^2}$$

$$\frac{\partial^2 I}{\partial z^2} = l_u c_u \frac{\partial^2 I}{\partial t^2}$$

Which are 1D wave propagation.

The speed of wave is $c^* = \frac{1}{\sqrt{l_u c_u}}$ and $k = \frac{\omega}{c^*} = \frac{2\pi}{\lambda}$

$$V(z,t) = V_0 e^{i(kz - \omega t)}$$

$$I(z,t) = I_0 e^{i(kz - \omega t)}$$

Plug in $\frac{\partial V}{\partial t} = -\frac{1}{c_u} \frac{\partial I}{\partial z}$ and we get

$$-i\omega V_0 = -\frac{1}{c_u} ikI_0$$

$$\frac{V_0}{I_0} = \frac{1}{c^* c_u} = \sqrt{\frac{l_u}{c_u}} = Z_0$$

Z_0 is the characteristic impedance for the transmission line.

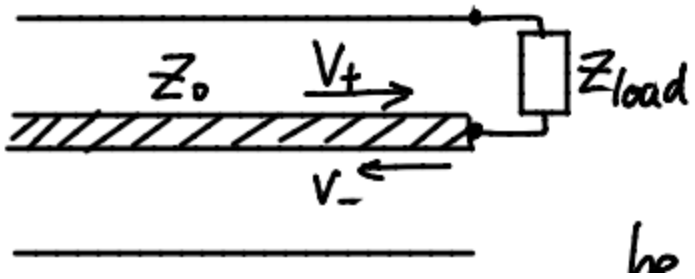

Consider a load Z_{load} is connected between the two conductors at one end.

The incident wave V_+ will be partially reflected. The reflection can be solved by the boundary condition.

$V_+ = {V_+}^0 e^{i(kz-\omega t)}$ and $I_+ = {I_+}^0 e^{i(kz-\omega t)}$

and reflection: $V_- = {V_-}^0 e^{i(-kz-\omega t)}$ and $I_- = {I_-}^0 e^{i(-kz-\omega t)}$

$$V_{load} = V_+ + V_-$$

$$I_{load} = I_+ - I_-$$

$$Z_{load} = \frac{V_{load}}{I_{load}} = \frac{{V_+}^0 e^{i(kz-\omega t)} + {V_-}^0 e^{i(-kz-\omega t)}}{{I_+}^0 e^{i(kz-\omega t)} - {I_-}^0 e^{i(-kz-\omega t)}}$$

Since $\frac{V_+}{I_+} = \frac{V_-}{I_-} = Z_0$,

$$\frac{Z_{load}}{Z_0} = \frac{{V_+}^0 e^{ikz} + {V_-}^0 e^{-ikz}}{{V_+}^0 e^{ikz} - {V_-}^0 e^{-ikz}}$$

The reflection $r \equiv |\frac{V_-}{V_+}|$, so

$$\frac{Z_{load}}{Z_0} = \frac{1+r}{1-r}$$

And

$$r = \frac{Z_{load} - Z_0}{Z_{load} + Z_0}$$

$$R = r^2 = (\frac{Z_{load} - Z_0}{Z_{load} + Z_0})^2$$

Typical values of the characteristic impedance for different transmission lines:

TV antenna 300 ohm, cable 75 ohm.

For most scientific instruments, Z_0= 50 ohm, depends on the specific geometry of the transmission line.

Additional reference [13].

References

[1] M. E. Barber, E. Y. Ma, and Z. X. Shen, *Microwave Impedance Microscopy and Its Application to Quantum Materials*, Nat. Rev. Phys. **4**, 61 (2022).

[2] Z. Chu, L. Zheng, and K. Lai, *Microwave Microscopy and Its Applications*, Annu. Rev. Mater. Res. **50**, 105 (2020).

[3] Y.-T. Cui and E. Yue Ma, *Capacitance Spectroscopy of Semiconductors*, Vol. 3 (Jenny Stanford Publishing, 2018).

[4] E. Yue Ma, *EMERGING ELECTRONIC STATES AT BOUNDARIES AND DOMAIN WALLS IN QUANTUM MATERIALS*, PhD Thesis (2016).

[5] Z. Chu, *Imaging Photo-Carrier Dynamics and Correlated States in Two-Dimensional Semiconductors Committee*, PhD Thesis (2021).

[6] X. Wu, *Development and Applications of Microwave Impedance Microscopy for Imaging Emergent Properties in Quantum Materials*, PhD Thesis (2018).

[7] Y.-T. Cui, E. Y. Ma, and Z.-X. Shen, *Quartz Tuning Fork Based Microwave Impedance Microscopy*, Rev. Sci. Instrum. **87**, 063711 (2016).

[8] H. Edwards, L. Taylor, W. Duncan, and A. J. Melmed, *Fast, High-Resolution Atomic Force Microscopy Using a Quartz Tuning Fork as Actuator and Sensor*, J. Appl. Phys. **82**, 980 (1997).

[9] L. Zheng, D. Wu, X. Wu, and K. Lai, *Visualization of Surface-Acoustic-Wave Potential by Transmission-Mode Microwave Impedance Microscopy*, Phys. Rev. Appl. **9**, 1 (2018).

[10] K. Lai, W. Kundhikanjana, M. Kelly, and Z. X. Shen, *Modeling and Characterization of a Cantilever-Based near-Field Scanning Microwave Impedance Microscope*, Rev. Sci. Instrum. **79**, 063703 (2008).

[11] F. J. Giessibl, *High-Speed Force Sensor for Force Microscopy and Profilometry Utilizing a Quartz Tuning Fork*, Appl. Phys. Lett. **73**, 3956 (1998).

[12] J.-M. Friedt and É. Carry, *Introduction to the Quartz Tuning Fork*, Am. J. Phys. **75**, 415 (2007).

[13] Y. Yang, K. Lai, Q. Tang, W. Kundhikanjana, M. A. Kelly, K. Zhang, Z. X. Shen, and X. Li, *Batch-Fabricated Cantilever Probes with Electrical Shielding for Nanoscale Dielectric and Conductivity Imaging*, J. Micromechanics Microengineering **22**, (2012).

Chapter 3 Imaging Dual-Moiré Lattices in Twisted Bilayer Graphene Aligned on Hexagonal Boron Nitride Using Microwave Impedance Microscopy

Moiré superlattices (MSL) formed in van der Waals materials have become a promising platform to realize novel two-dimensional electronic states. Angle-aligned trilayer structures with two interfaces can form two sets of MSLs which could potentially interfere. Here, we present direct imaging of the moiré patterns in both monolayer and twisted bilayer graphene aligned on hBN, using combined microwave impedance microscopy (MIM) and conductive atomic force microscopy (cAFM). Correlation of the two techniques reveals the contrast mechanism for the achieved ultrahigh spatial resolution (<2 nm). Dual-moiré superlattices with different periodicities have been observed in the later trilayer stack. The smaller MSL breaks the rotational symmetry (C_6) and exhibits abrupt discontinuities at the boundaries of the larger MSL. Using a rigid atomic-stacking model, we demonstrate that the hBN layer considerably modifies the MSL of the twisted bilayer graphene. We further analyze its effect on the reciprocal space spectrum of the dual-moiré system. The content of this research was published in my co-first authored paper, in which my contribution includes MIM measurements, data analysis and manuscript writing.

Huang, X.*, Chen, L.*, Tang, S., Jiang, C., Chen, C., Wang, H., Shen, Z. X., Wang, H. & Cui, Y. T. Imaging Dual-Moiré Lattices in Twisted Bilayer Graphene Aligned on Hexagonal Boron Nitride Using Microwave Impedance Microscopy. *Nano Lett.* **21**, 4292–4298 (2021). [1]

3.1 Moiré Superlattices in 2D Materials and Emergent Quantum Phases

Stacking two layers of atomically thin materials of similar structures at a controlled alignment angle can form a MSL. For example, such a MSL can form in aligned monolayer graphene on hBN or in twisted bilayer graphene (shown in **Fig. 3.1**). In a bilayer stack with a small twisted angle θ, the lattice constants are a_0 and $a_0(1-\delta)$ for the two layers, respectively. The moiré wavelength λ_m can be calculated using the following equation [2]:

$$\lambda_m = a_0(1-\delta) \Big/ \sqrt{2(1-\delta)(1-\cos\theta)+\delta^2},$$

The lattice mismatch (δ) is about several percent for commonly studied materials and the twist angle is usually within several degrees[15]. The MSL could have a periodicity ranging from ten to hundreds of nanometers, much larger than those of individual atomic lattices. The periodic modulation in the MSL can strongly modify the electronic structure of one or both layers and thus providing a promissing platform to explore novel electronic phases in two dimensions. In 0°-aligned monolayer graphene (MLG) on hBN sturcture, the MSL can induce secondary Dirac cones in the electronic band structure of MLG, leading to a fractal structure in the Landau level spectrum, known as the Hofstadter's butterfly as shown in **Fig. 3.1a** [3–5].Magic angle (~1.1°) twisted bilayer graphene can form ultraflat minibands (**Fig. 3.1b**) which host strongly correlated Mott insulator and superconducting states [6–8]. The idea has been further realized in various versions of twisted graphene systems as well as semiconducting transition metal dichalcogenide moiré superlattices [9,10,19–26,11–18]. When a twisted bilayer graphene is further aligned on the hBN layer,

[15] Interestingly, a 30°-twisted bilayer graphene will form a quasicrystal.

ferromagnetism can be induced in the trilayer stack and quantized anomalous Hall effect has been reported, indicating the formation of a Chern insulator state [27,28]. In such aligned trilayer stacks, multiple MSL can potentially form, providing an extra degree of freedom for the electronic band engineering [29–31].

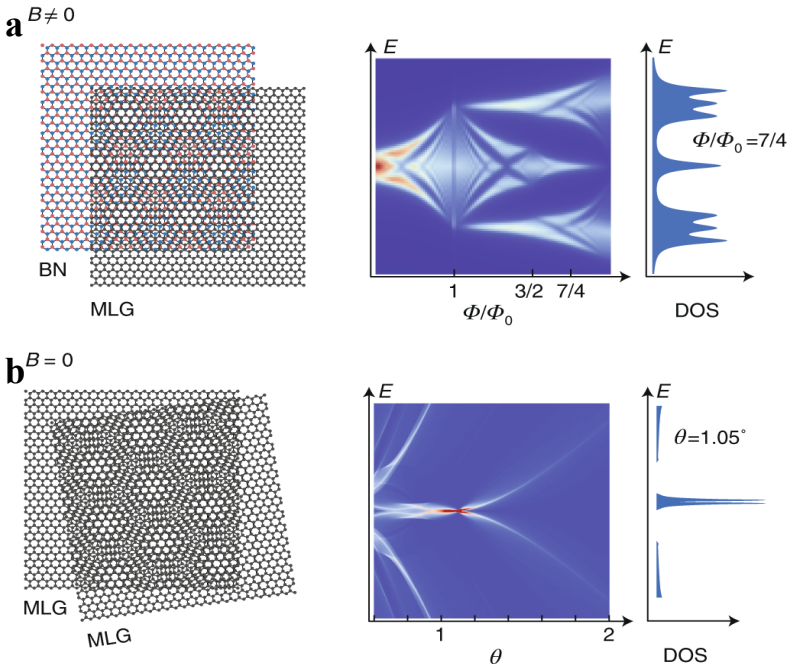

Figure 3.1 Engineering flat bands in van der Waals heterostructures. a, Hofstadter's minibands in aligned monolayer graphene/hBN system under a magnetic field. **b**, Zero-magnetic-field flat bands in twisted bilayer graphene. Panel **a-b** adapted with permission from REF 16, copyright Springer Nature.

It's of great importance to directly image an MSL for characterizing the geometric structure. Spatially resolved techniquues are idea tools for this purpose as they provide direct information in the real space. Traditional imaging techniques such as transmission electron microscopy [32,33] and scanning tunneling microscopy [34–39] have been used to image MSLs but these methods require specialized sample preparation with a low throughput. Different imaging modules based on atomic force microscope [2,26,30,40–45] have been utilized to visulize MSL but to further improve the resolution is still challenging. Here we report the observation of a dual-moiré pattern in a chemical vapor deposition (CVD) grown twisted bilayer graphene (TBG) which is aligned on an BN substrate using

both scanning MIM and cAFM. An ultrahigh spatial resolution has been achieved (better than 2 nm) and no additional sample preparation is required before performing MIM scan. The correlation between two complementary scan images pinpoints the tip-graphene contact resistance as the mechanism for the unexpected ultrahigh resolution. In the TBG-hBN trilayer structure, two sets of MSLs are observed: a larger MSL (~16 nm) due to the 0°-aligned graphene/hBN and a smaller MSL (3–6 nm) due the the TBG. The smaller MSL is distorted and exhibits abrupt discontinuities at the boundaries of the larger MSL. Using a rigid atomic stacking model, these features are recovered by considering all three layers in the formation of the dual-moiré pattern. Our analysis of the dual-moiré pattern in the reciprocal-space suggest a potential modification of the electronic structure of the TBG.

3.2 Sample Preparation and Ultrahigh Resolution Scanning MIM

3.2.1 CVD-Grown Monolayer and Twisted Bilayer Graphene on hBN Substrate

Before the growth of graphene layers, the hBN flakes are mechanically exfoliated onto quartz and annealed at 600 °C in oxygen flow to remove residues. Then the quartz substrate with hBN is placed in a graphite tube and put into the CVD chamber. The CVD growth of twisted bilayer graphene is carried out at 1300 °C. First, a mixture of ethyne and silane in pulsed flow is introduced to form the first polycrystalline graphene layer, and then the mixture is tuned to be in a stable flow to grow the second graphene layer. After that, the substrate cools slowly to room temperature. For the MIM measurement, the sample requires little preparation. For the cAFM measurement, an electrical contact is made to the polycrystalline graphene layer that is continuous in a large area, using silver epoxy in remote locations far from the tip scan regions. In the previous research by our

collaborators [2], single crystalline graphene monolayers have been grown on the hBN substrate with the crystals precisely aligned (twist angle $< 0.05°$). In our study here, the twist angles for the second graphene layer range from $2 - 5°$.

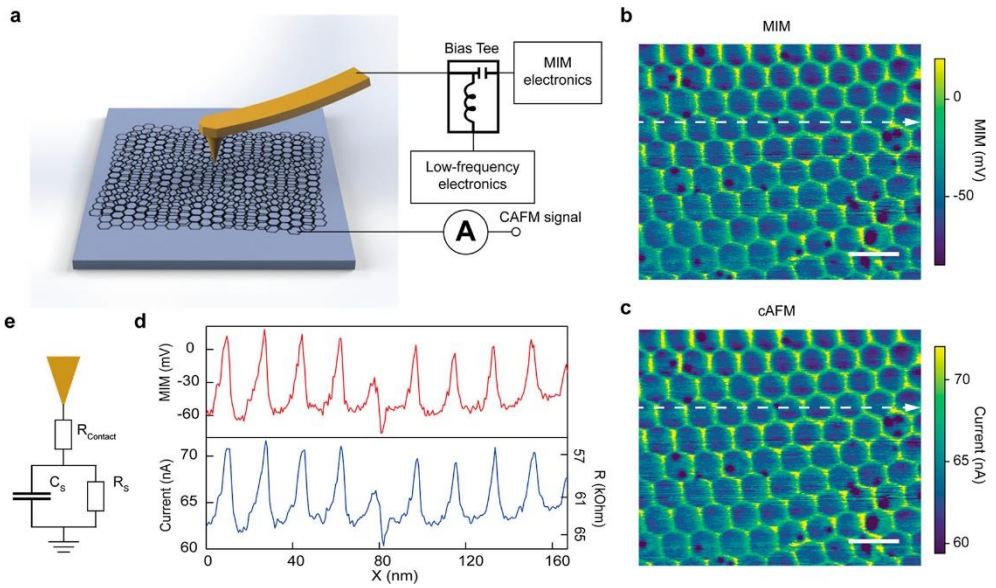

Figure 3.2 High-resolution imaging of moiré pattern in monolayer graphene/hBN sample. a, Schematics of the experimental setup. Simultaneously acquired **(b)** MIM and **(c)** cAFM images. **d**, Extracted line data from **(b)** and **(c)** along the dotted lines. **e**, Effective circuit model for the tip-graphene impedance probed in the contact mode MIM. Scale bars are 20 nm. Panel **a-e** adapted with permission from REF 1, copyright ACS.

3.2.2 MIM and cAFM Measurements of Monolayer Graphene/hBN Structure

First, we demonstrate high-resolution MIM imaging of the MSL in monolayer graphene on hBN. The setup of the measurement is shown in **Fig. 3.2a**. In 0°-aligned graphene/hBN structure, the MSL is calculated to have a periodicity of approximately 14 nm[16]. In the MIM measurement, a shielded cantilever probe[17] is in direct contact with the grapgene layer. A microwave signal (about 0.01 mW at 3 GHz) is routed to the probe, and

[16] Lattice mismatch ~1.8% between graphene and hBN.
[17] The cantilever probes for MIM are purchased from PrimeNano Inc.

the reflected signal is demodulated to generate the MIM signals. In the MIM electronics, a microwave IQ-mixer is used which can be considered as a lock-in working at GHz frequencies.

We are using the Bruker Dimension Icon AFM platform to perform the scanning. It is equiped with an optical microscope on the side which will help us to quickliy locate the hBN flakes which has graphene layers grown ontop. However, monolayer or bilayer graphene are almost invisible in the view of this optical microscope (the substrate here is a thick BN layer ontop of a sapphire chip while in common exfloiation process researchers use silicon chip with an oxidate layer (~300 nm) which enables them to directly visulize the monolayer graphene)[18]. First, a large-range (tens of um) tapping-mode MIM scan will be performed to search for graphene layers. Thanks for MIM's ability to image local conductivity, any graphene crystaline layers will manifest as a regular shape (hexagons) with large contrast in conductivity compared with the neigrbouring BN substrate. But before visualizing the moire patter in G/BN superlattice, continuous contact-mode scan (called AFM cleaning) needs to be done to improve the sample quality. This can be done by simply increase the deflection setpoint (which will increase the applied force between the tip and sample) and monitor the MIM channels during the continuous scan. Eventually, one will see some features in the MIM channels[19]. By carefully conditioning the tip-sample junction (tune the scan parameters), direct visualization of the moire pattern at nanoscale can be achieved.

[18] Please see the seminar paper *Making Graphene Visible*, APL 91, 063124, (2007).
[19] Not in topography channels.

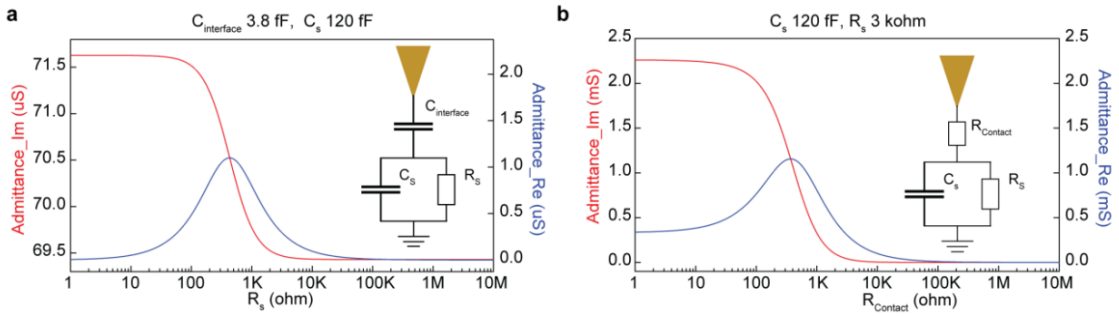

Figure 3.3 Simulated MIM response curves based on two effective circuit models. a, Conventional MIM measurements. The tip-sample dominated by an interface capacitance. **b**, Direct contact MIM measurement with a good electrical conduction for tip-sample junction. The response curves plot the imaginary and real parts of the tip-sample admittance (inverse of impedance) as a function of varying tip-sample contact resistance. Panel **a-b** adapted with permission from REF 1, copyright ACS.

Before moving forward to analysis of the MIM images, one thing will need to be discussed on how to calibrate the MIM channels, i.e. distinguishing the Im and Re channels. In the conventional MIM measurements, the tip-sample impedance is determined by a capacitive coupling due to the insulating spacer which contributes to an interface capacitor in the circuit model (as shown in the inset of **Fig. 3.3a**) with a typical response curve. The signal difference between the insulating and conductive limits of the sample conductivity provides a reference for the maxium MIM-Im contrast one can expect for this model. Usually, a calibration sample (such as patterned Al thin films with a top native oxide layer of several nanometer thick) can be used to obtain a reference value for the maximum MIM-Im contrast. In our direct-contact MIM measurement on graphene moiré systems, the MIM contrast between center and corner of the moiré hexagon is often much larger than the maximum reference contrast measured on the calibration sample, indicating the breakdown of the conventional tip-sample impedance model.

A typical MIM[20] image of a graphene/hBN MSL is shown in **Fig. 3.2b**. It has a honeycomb pattern expected for the MSL which clearly shows the commensurate-incommensurate transition in small angle twisted graphene/hBN as previously visualized by Young's modulus afm images [43]. This image shows a spatial resolution better than 2 nm. Some noticeable distortions are likely due to local strains in the graphene flake formed during the high-temperature growth process. Fourier transform analysis reveals an averaged periodicity of ~16 nm, corresponding to a tensil strain of ~0.15% in the monolayer graphene. It is worth noting that the ultrahigh spatial resolution is unprecedented in conventional MIM experiments, whose resolution is dominated by the actual tip size (~50 nm) [46–48]. Recently, there are groups reporting high resolution in MIM imaging of MSLs [49–51]. Reference [49] identified the formation of a sharp protrusion during the tip condition process in repeated scanning. Reference [50,51] proposed that water meniscus trapped at the tip apex or piezoelectric effect could be responsible for the high spatial resolution. We will show that, by correlating with simultaneously acquired cAFM images, we conclude that the MIM signal contrast is caused by the local variation of tip-sample contact resistance.

The MIM cantilever is a metal probe which can be used for cAFM measurement. For combined MIM and cAFM measurements (shown in **Fig. 3.2a**), an additional low-frequency AC voltage (5 mV at ~7.4 kHz) is coupled through a microwave bias tee and applied to the MIM probe on top of the microwave signal. The current flowing through the

[20] Here we use **MIM** instead of **MIM-Im** or **MIM-Re** to reserve the reference phase issue until further discussion.

tip-sample junstion is amplified and recorderd as the cAFM image. We also performed standalone cAFM measurement (for 4.2°-twisted TBG/hBN device #2) using specialized cAFM probes[21], when only cAFM is measured with applied DC bias: 5-10 mV.

Figure 3.2c plots the cAFM image obtained simultaneously with the MIM image in **Fig. 3.2b**. The two images show strikingly similar patterns and even fine features look almost identical as demonstrated in the linecuts in **Fig. 3.2d**. Such high degree of similarity indicates that the contrast mechanism for the MIM signal is the same as that of cAFM, i.e., the tip-graphene contact resistance. As illustrated in **Fig. 3.2e**, when the tip is in good electric contact with the graphene layer, a contact resistance forms at the tip-graphene junction, which allows the low-frequency current to flow through. It also contributes the total tip-sample impedance at microwave frequency, which modulates the microwave reflection and produces the MIM signal contrast. The high spatial resolution is thus determined by the electrically conductive tip-sample contact interface which can be subnanometers in size depending on the contact quality [41].

In typical MIM measurements, the tip-sample electric contact is usually dominated by a thin insulating spacer layer (such as hBN layers). As a result, the typical MIM response curves, obtained by modeling the tip-sample contact as a capacitance (**Fig. 3.3a**), do not apply to this case. As suggested by the combined MIM-cAFM measurement, tip-sample interface has a contact resistance which is on the order of tens kOhms. The effective circuit model and the corresponding response curves are shown in **Fig. 3.3b**. Note than the span of the tip-sample admittance (y-axis) is much larger than that of theconventional model.

[21] Asylum electrolever tip with conductive coating for nano-electrical measurements.

The MIM signal contrast of the tip-sample admittance from **Figure 3.2b** (after calibration of the signal gain) corresponds to an admittance change of ~6 uS, which agress reasonably well with estimates from cAFM data in **Figure 3.2c**, ~2 uS. The deviation could be due to the uncertainty in the tip geometry used in the calibration procedure.

Unlike cAFM, the MIM measurement does not require a counter electrtode on the sample, making it more versatile to characterize the MSL without going through extensive fabrication processes for making electric leads.

3.3 Dual-Moiré Pattern in TBG/hBN Trilayer Structure

During the CVD growth, a second graphene layer (G2) can grow on top of the first graphene layer (G1) at an angle which varies at different locations. It allows us to image the moiré superstructure of the G2/G1/hBN trilayer stack. Two representative images are shown in **Fig. 3.4** with MIM (**Fig. 3.4a**) and cAFM (**Fig. 3.4b**) both in the contact mode (images of more samples at different twist angles are presented in the Supporting Information). In each image, we identify two sets of MSLs at different length scales. Bright spots form a triangular MSL with a smaller periodicity. The smaller MSL is divided into hexagonal domains by a larger MSL and the periodicity of the smaller MSL is interrupted at the domain boundaries. The observations of the moiré pattern in this trilayer stack suggest the coexistence of two sets of MSLs formed between G2/G1 and G1/hBN.

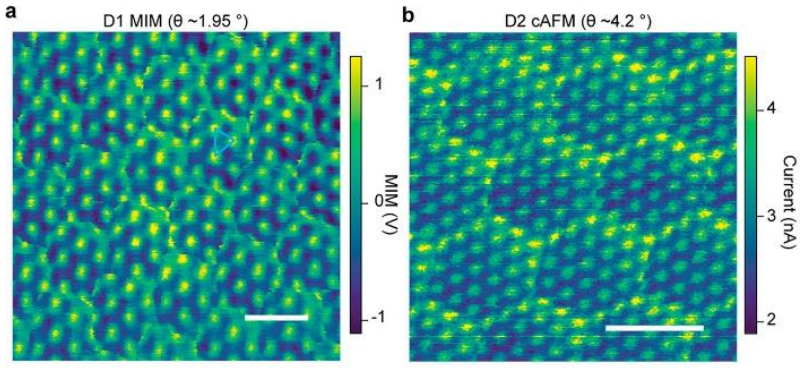

Figure 3.4 Imaging dual-moiré pattern in G2/G1/hBN trilayer stacking. a, MIM image of a trilayer sample D1 ($\theta = 1.95°$). **b**, cAFM image of trilayer sample D2 ($\theta = 4.2°$). Panel **a-b** adapted with permission from REF 1, copyright ACS.

To understand the moiré superstructure formed in such a trilayer stack, we perform analysis based on a rigid atomic stacking model. In this trilayer structure, a G2 layer is stacked at an angle θ relative to the G1 layer which is 0°-aligned on hBN layer. We focus on the range $\theta \geq 1.8°$ so that the periodicity of G2/G1 is much smaller than that of G1/hBN (~14 nm). This scenario has not been explored in previous studies which primarily focused on cases where two moiré periodicities are similar [29–31].

3.4 Numerical Simulation and Analytical Solution for a Trilayer Stack

Firstly, the analysis can be done by numerical simulation. The periodic atomic lattice for each of the three layers in a TBG/hBN structure can be described by the lowest harmonics:

$$f(\vec{r}) = \sum_{i=1}^{3} e^{i\vec{k}_i \cdot \vec{r}}$$

where $\vec{k}_i$ (i=1,2,3) are the unit vectors for individual atomic lattice. Thus $\vec{k}_i \cdot \vec{r}$ represent the phase of the lattice. The formation of moiré patterns depends on the alignment among the phases of the three layers. The center of each moiré-S domain can be identified by the location where the three lattice phases are closest to each other, as shown in Fig. 3.5. The

twist-angle evolution of the moiré-S (periodicity and orientation along three symmetric directions) can be obtained.

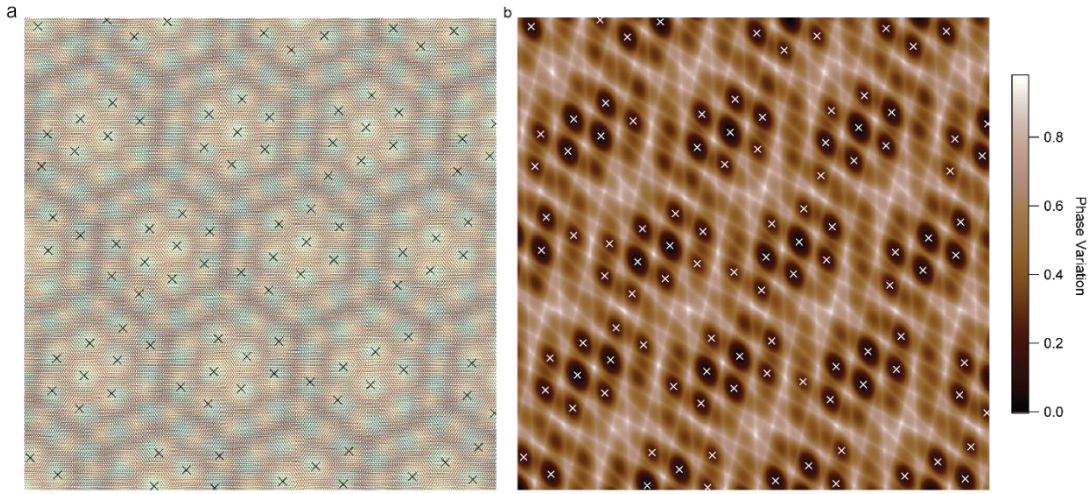

Figure 3.5 Numerical simulation of a trilayer stack. a, Atomic stacking model for twisted bilayer graphene (3.6°) on hBN. Blue atoms for hBN, red atoms for aligned graphene (G1) and green atoms for rotated graphene (G2), respectively. **b**, Calculated phase variation Δ_{phase}. Locations of the minimum values of Δ_{phase} are calculated by fittings and plotted by the markers in both (a) and (b). Panel a-b adapted with permission from REF 1, copyright ACS.

Secondly, the phase variation can be calculated in the following way:

$$\Delta_{phase}(\vec{r}) = (\text{wrap}(\vec{k}_1^{hBN}\cdot\vec{r} - \vec{k}_1^{G1}\cdot\vec{r}))^2 + (\text{wrap}(\vec{k}_2^{hBN}\cdot\vec{r} - \vec{k}_2^{G1}\cdot\vec{r}))^2 + (\text{wrap}(\vec{k}_1^{hBN}\cdot\vec{r} - \vec{k}_1^{G2}\cdot\vec{r}))^2 + (\text{wrap}(\vec{k}_2^{hBN}\cdot\vec{r} - \vec{k}_2^{G2}\cdot\vec{r}))^2 + (\text{wrap}(\vec{k}_1^{G1}\cdot\vec{r} - \vec{k}_1^{G2}\cdot\vec{r}))^2 + (\text{wrap}(\vec{k}_2^{G1}\cdot\vec{r} - \vec{k}_2^{G2}\cdot\vec{r}))^2$$

Here the wrap() function wraps the phase value to the range $[-\pi, \pi)$. The centers of moiré-S domains correspond to the minimum values of Δ_{phase}. To find the analytical expressions for the unit vectors, we find the center locations of adjacent moiré-S domains in the following way. First, it is obvious that $\vec{r} = 0$ corresponds to the minimum location of Δ_{phase} in the (0, 0) moiré-S domain around origin. Second, we solve the local minimum

locations of Δ_{phase} in the (1, 0) and (0, 1) moiré-S domains, respectively. For simplicity, we define $\Delta\vec{k}_i^a = \vec{k}_i^{hBN} - \vec{k}_i^{G1}$, $\Delta\vec{k}_i^b = \vec{k}_i^{hBN} - \vec{k}_i^{G2}$ and $\Delta\vec{k}_i^c = \vec{k}_i^{G1} - \vec{k}_i^{G2}$, where i = 1 or 2.

In the (1, 0) domain, there should be an accumulated phase difference of 2π between G1 and G2 as well as between hBN and G2 along $\Delta\vec{k}_1^b$ and $\Delta\vec{k}_1^c$. Therefore, we can manually add the phase difference to remove the wrap() function and we get:

$$\Delta_{phase\ in\ (1,0)}(\vec{r}) = \left(\Delta\vec{k}_1^a \cdot \vec{r}\right)^2 + \left(\Delta\vec{k}_2^a \cdot \vec{r}\right)^2 + \left(\Delta\vec{k}_1^b \cdot \vec{r} - 2\pi\right)^2 + \left(\Delta\vec{k}_2^b \cdot \vec{r}\right)^2$$
$$+\left(\Delta\vec{k}_1^c \cdot \vec{r} - 2\pi\right)^2 + \left(\Delta\vec{k}_2^c \cdot \vec{r}\right)^2$$

The local minimum location can be obtained by solving $\frac{\partial}{\partial x}\Delta_{phase}(\vec{r}) = 0$ and $\frac{\partial}{\partial y}\Delta_{phase}(\vec{r}) = 0$, which gives

$$\vec{r}_1 = \frac{2\pi \sum_{i,m}[(\Delta\vec{k}_1^b + \Delta\vec{k}_1^c) \cdot (\Delta\vec{k}_i^m \times \hat{z})](\Delta\vec{k}_i^m \times \hat{z})}{\frac{1}{2}\sum_{i,j,m,n} |\Delta\vec{k}_i^m \times \Delta\vec{k}_j^n|^2}$$

where i,j = 1 or 2, m,n = a, b, or c.

Similarly, in the (0, 1) domain, the additional term of 2π should be added to $\Delta\vec{k}_2^b \cdot \vec{r}$ and $\Delta\vec{k}_2^c \cdot \vec{r}$. The local minimum location is

$$\vec{r}_2 = \frac{2\pi \sum_{i,m}[(\Delta\vec{k}_2^b + \Delta\vec{k}_2^c) \cdot (\Delta\vec{k}_i^m \times \hat{z})](\Delta\vec{k}_i^m \times \hat{z})}{\frac{1}{2}\sum_{i,j,l,m} |\Delta\vec{k}_i^m \times \Delta\vec{k}_j^n|^2}$$

where i,j = 1 or 2, m,n = a, b, or c.

The third unit vector is then $\vec{r}_3 = \vec{r}_2 - \vec{r}_1$.

Note that if we pick the hBN layer to be identical as the G1 layer, the trilayer stack should become a G1/G2 bilayer stack. Indeed, by setting $\vec{k}_i^{hBN} = \vec{k}_i^{G1}$ hence $\Delta\vec{k}_i^a = 0$ and $\Delta\vec{k}_i^b = \Delta\vec{k}_i^c$, it can be verified that the analytical expressions for $\vec{r}_1$ and $\vec{r}_2$ reduce to those expected for a bilayer stack. Analytical solution for the evolution of three unit vectors in moiré-S has been obtained.

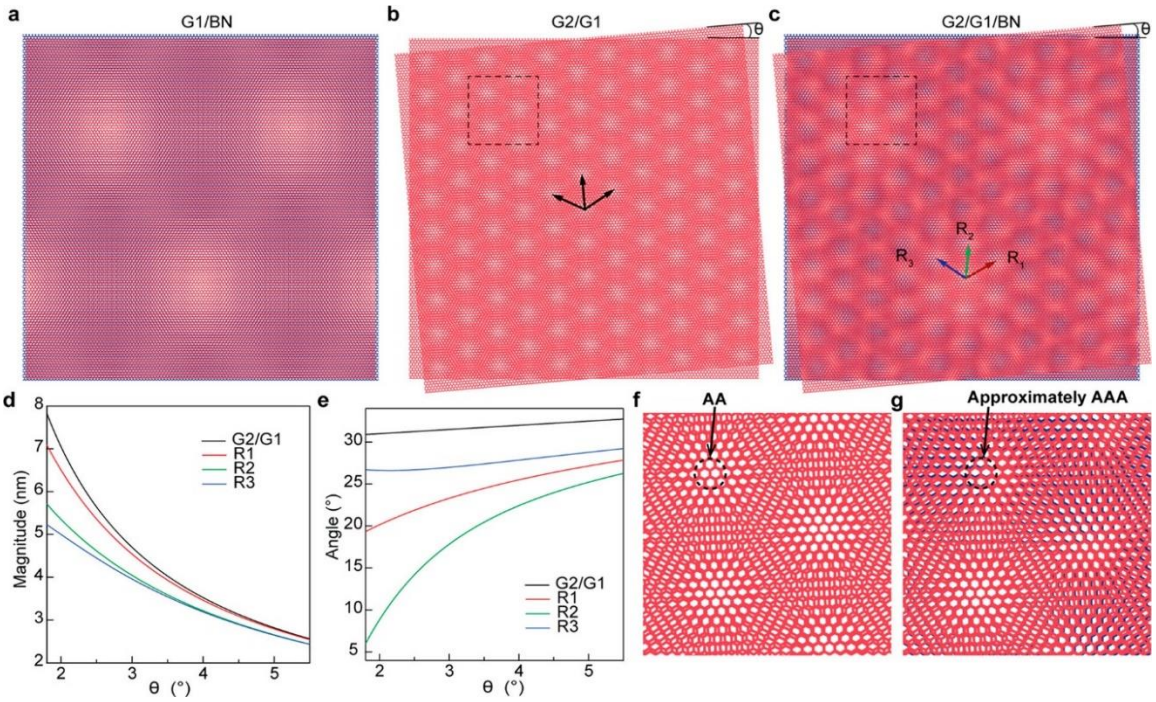

Figure 3.6 Analysis of the moiré patterns in a trilayer stacking. a 0°-aligned graphene/hBN. **b** Twisted bilayer graphene. **c**, Twisted bilayer graphene with the G1 layer aligned on hBN. (**d** and **e**) Magnitudes and orientations of the unit vectors (arrows in **b** and **c**). (**g** and **f**) Zoomed-in images for the dotted regions in panels **b** and **c**. Panel **a-g** adapted with permission from REF 1, copyright ACS.

Figure 3.6 presents our numerical analysis results. In the trilayer structure (**Fig. 3.6c)**, a moiré pattern with a smaller periodicity (moiré-S) is divided into domains with a larger periodicity (moiré-L). Interestingly, while the two sets resemble the MSLs in invidual bilayer structures of G2/G1 (**Fig. 3.6b**) and G1/hBN (**Fig. 3.6a**), it's not a simple

combination of the two. There are two most notable features. First, the moiré-S pattern is along a different direction compared with the G2/G1 pattern with a same twist angle as shown by the arrows in each figure (**Fig. 3.6b** and **3.6c**). Second, the periodicity of moiré-S is interrupted near the domain boundary between two moiré-L hexagons. We further derive the analytical expressions for the three unit vectors of moiré-S (see the Supporting Information at the end of this chapter). For each unit vector, we plot its magnitude and orientation with respect to the corresponding unit vector in G1 as a function of θ in panels d and e of **Fig. 3.6d** and **3.6e**, respectively. We find that, compared to the G2/G1 MSL in which the three unit vectors have equal maagnitudes and are uniformly spaced at 60° apart (the black curves in **Fig. 3.6d** and **3.6e**), the moiré-S unit vectors have smaller and unequal magnitudes and their orientations are also significantly deviated from those in G2/G1. These observations are more pronounced at small twist angles. Such deviations are due to the aligned hBN layer and can be readily seen in the analytical expressions presented. It can be understood in the folowing way. Without a hBN layer, the center of each moiré-S hexagons corresponds to the AA stacking of the two graphene layers (**Fig. 3.6f**). In the presence of the hBN layer, the center now should correspond to a nearly AAA stacking of all three layers where the A-site atoms are cloest to each other (**Fig. 3.6g**), which can be different from where the two A-site atoms from two graphene layers are closest to each other.

3.5 Comparison of Experimental results and Simulations

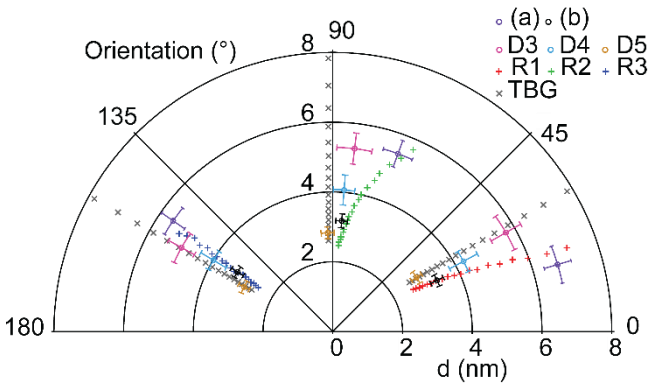

Figure 3.7 Comparison between experimental results and simulations in a polar plot. Unit vectors of the moiré-S lattice for all the samples compared with the modeling values from a trilayer stack (R1, R2, and R3) and from a bilayer stack (TBG). Panel adapted with permission from REF 1, copyright ACS.

Comparing our experimental observations (**Fig. 3.7**) with the modeling results, the two observed periodic patterns correspond to the moiré-S and moiré-L patterns in the model, respectively. In **Figure 3.4**, the moiré-S exhibits a triangular pattern of clear contrast with bright spots corresponding to a low tip-sample contact resistance. According to our analysis, these spots are the nearly AAA stacking regions in the trilayer structure (**Fig. 3.6g**). The moiré-L patterns is marked by boundaries of hexagon domains while the domain boundaries typically show an enhanced signal (a lower tip-sample contact resistance). More strikingly, the moiré-S has notable discontinuities at all moiré-L domain boundaries (see **Fig. 3.4**), exactly expected from our model (**Fig. 3.6**). We analyze the unit vectors of the moiré-S patterns and plot them in a polar plot in **Fig. 3.7**, together with those calculated from our analytical expressions. We further determin the twist angle for all the observed dual-moiré images in different samples[22]. The measurement results agree well with model calculations. In particular, three unit vectors have unequal maagnitudes and

[22] See Supporting Information S2.

nonuniform angular spacings. These features are most pronounced in the case of **Figure 3.4a**, which has a smaller twist angle (~1.95°) corresponding to a larger periodicity.

3.6 Analysis of Dual-Moiré Pattern in the Reciprocal Space

Finally, we demonstrate the signatures of such a dual-moiré pattern in the reciprocal space, focusing on the effect of this diccontinuity at the domain boundaries. MIM image with a large scan range in sample D1 isA used for the fast Fourier transform (FFT) abalysis. In **Figure 3.8a**, the dual-moiré pattern fills the entire area with only a few local variations in the signal intensity. The FFT of **Fig. 3.8a** is shown in **Fig. 3.8b**. The spectrum contains a series of peaks which can be indentified in the following categories. A dashed hexagon centered around the origin corresponds to the moiré-L pattern. Bright spots at large k values correspond to the features from the moiré-S pattern. Because the moiré-S pattern is spatially modulated by the moiré-L boundaries, the moiré-L hexagon is further replicated at each of the bright spots in the moiré-S pattern. Other peaks are the higher-order peaks of these replicas. To betterillustrate their relation, we sketch out only the main features in **Fig. 3.8c**. We note that the moiré-S pattern contains the discontinuities at the moiré-L boundaries. To examine the effect of such discontinuities, we plot the reciprocal vectors ($k'_{moire-S}$, labeled with dashed purple arrows) calculated directly from the unit vectors identified for sample D1 in **Fig. 3.7**. These vectors essentially represent the FFT peaks for a continuous moiré-S pattern without any modulation by the moiré-L pattern. Their positions significantly deviate from the experimentally obtained peak positions ($k_{moire-S}$, labeled with solid purple arrows), and the differences are caused by the by the

discontinuities of the moiré-S pattern across the moiré-L domain boundaries, which are well-described by our analytical calculations presented in the Supporting Information.

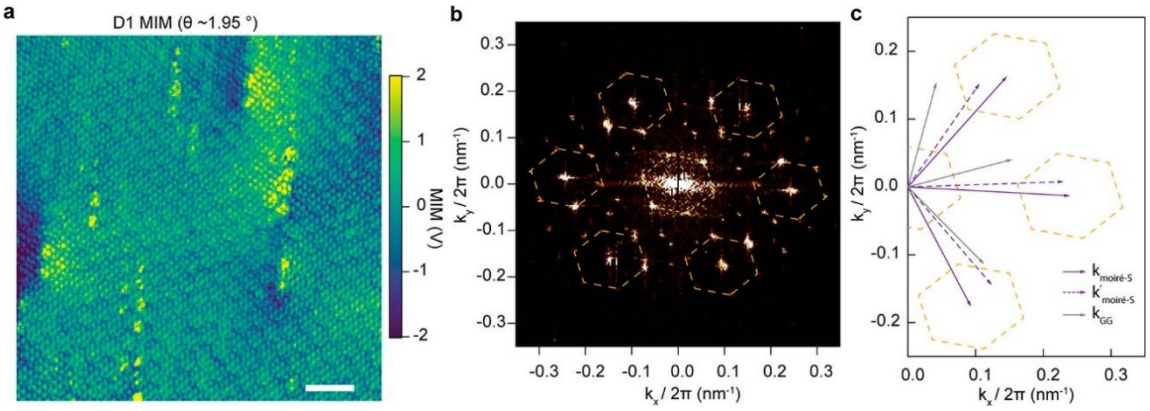

Figure 3.8 Analysis of the dual-moiré pattern in the reciprocal space. a, MIM image of a large area in sample D1. Scale bar: 40 nm. **b**, Fourier transform of the MIM image in panel **a**. **c**, Comparison of the Fourier peaks of the moiré-S lattice extracted from b ($k_{moire-S}$), the calculated reciprocal vectors from the moiré-S unit vectors determined from the real space data in D1 ($k'_{moire-S}$) and reciprocal vectors calculated for 1.95°-twsited bilayer graphene G2/G1 (k_{GG}). Panel **a-c** adapted with permission from REF 1, copyright ACS.

Furthermore, we plot the k_{GG} vectors (gray arrows) corresponding to a twisted bilayer graphene with a twist angle of 1.95°, the same as that determined in the trilayer structure measured in sample D1. From the comparison of k_{GG} with $k_{moire-S}$ and $k'_{moire-S}$, we identify the effect in the k-space structure of the twisted bilayer graphene due to the aligned hBN layer. As discussed before, the aligned hBN layer changes the local moiré-S pattern by a small rotation as well as a distortion that breaks the original 6-fold rotational symmetry, which is reflected in the k-space as the change from k_{GG} to $k'_{moire-S}$. Then the discontinuities at the moiré-L boundaries further shift $k'_{moire-S}$ to $k_{moire-S}$. Similar results in the Fourier transform analysis can be obtained for other samples. The k-space structure probed in our study reflects the spatial modulation of the tip-sample contact resistance which should potentially modify the electronic structure of the twisted bilayer

graphene in the momentum space. Our results inspire further experimental and theoretical studies, such as band structure calculations along these directions.

Supporting Information

S1. Data on Additional Samples

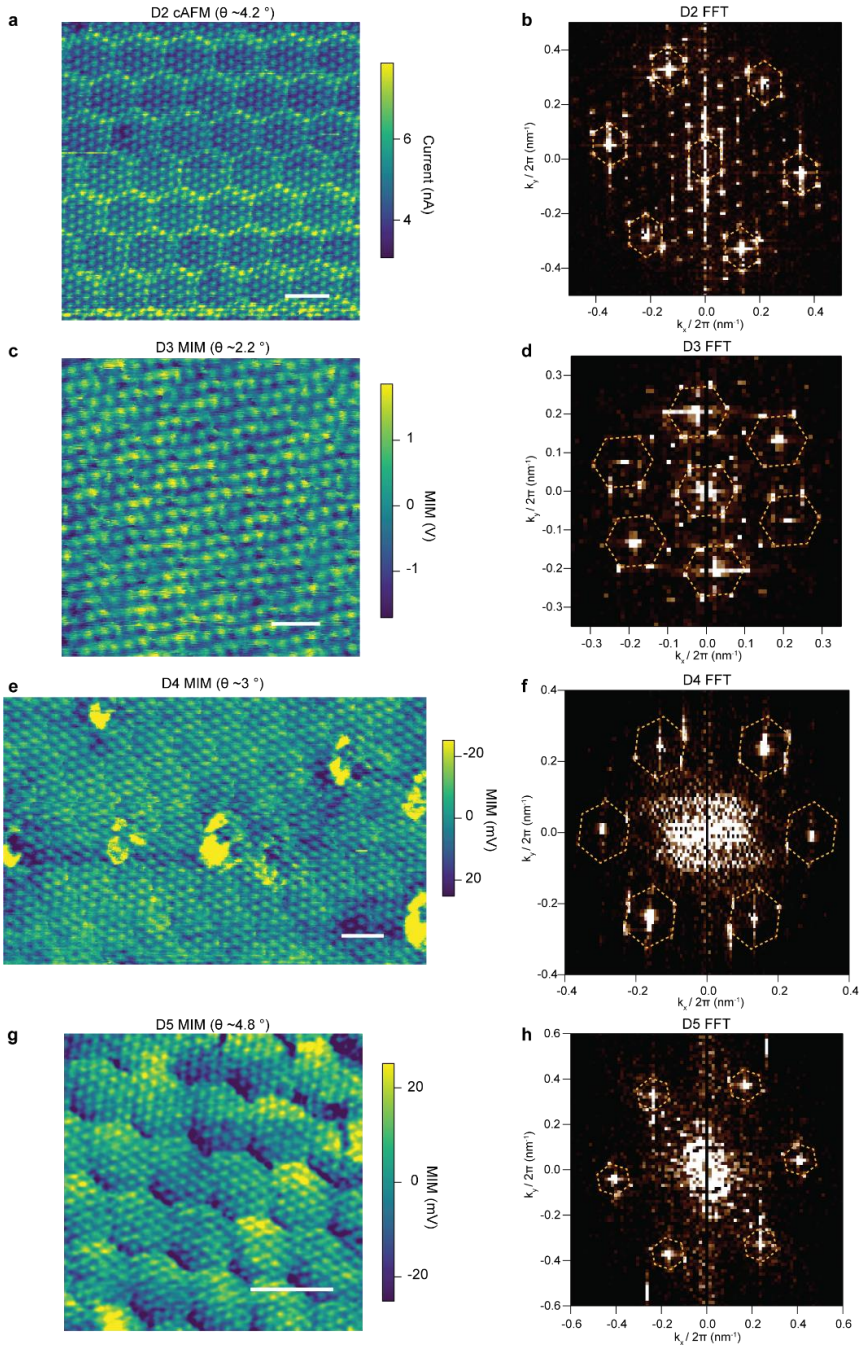

Figure 3S1 MIM/cAFM images for TBG/hBN samples D2-D5. (**a**, **c**, **e** and **g**) and their FFT images (**b**, **d**, **f** and **h**). All scale bars: 15 nm. Panel **a-h** adapted with permission from REF 1, copyright ACS.

S2. FFT Analysis on Dual-Moiré Patterns

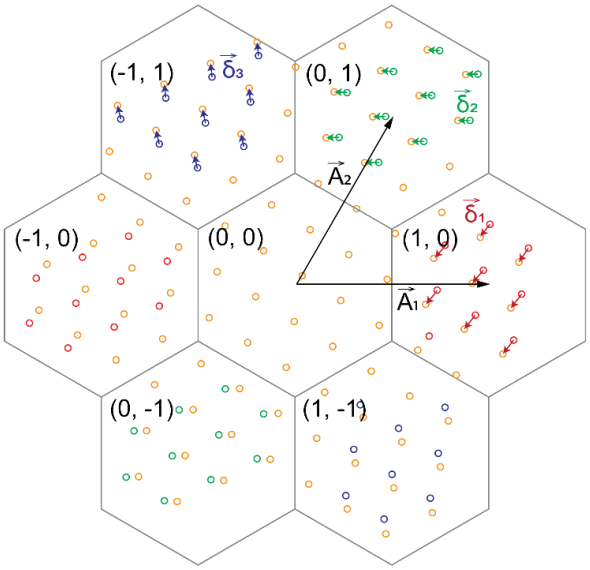

Figure 3S2 FFT analysis of a periodic pattern with discontinuities at the boundaries of the large periodic structure. Orange circles are the lattice extended from domain (0, 0) without including any discontinuities. Red circles are those for hexagon domains (1, 0) and (-1, 0). Green (blue) ones are for domains (0, 1) and (0, -1) ((-1, 1) and (1, -1)). Panel adapted with permission from REF 1, copyright ACS.

In this section, we present the mathematical analysis on the Fourier transform of a dual moiré superstructure in which the moiré-S pattern has discontinuities at the boundaries of the moiré-L unit cell domains.

The periodic structure of the triangular moiré-S lattice can be described by the lowest harmonics of the following form:

$$f(\vec{r}) = \sum_{i=1}^{3} e^{i\vec{k}_i \cdot \vec{r}}$$

with $\vec{k}_1$, $\vec{k}_2$ and $\vec{k}_3 = \vec{k}_2 - \vec{k}_1$ as the three unit vectors of the moiré-S lattice.

Across the boundaries of the moiré-L domains, the discontinuities in the moiré-S lattice can be modelled as two displacement vectors, $\vec{\delta}_1$ and $\vec{\delta}_2$, along the two directions defined by the two unit vectors of the moiré-L lattice, $\vec{A}_1$ and $\vec{A}_2$, respectively. In the (m, n)-th unit cell of the moiré-L lattice, as shown in Fig. S4, the overall accumulated displacement will be:

$$\vec{\delta}_{mn} = m\vec{\delta}_1 + n\vec{\delta}_2$$

Therefore, in general, the moiré-S lattice with discontinuities can be expressed as

$$f(\vec{r}) = \sum_{i=1}^{3} e^{i\vec{k}_i\cdot(\vec{r}-\vec{\delta}_{mn})}$$

for $\vec{r}$ within the (m, n)-th domain. Therefore, the Fourier transform of $f(\vec{r})$ can be obtained by calculating the Fourier transform of each term, $F_i(\vec{k})$. Thus, we have:

$$F_i(\vec{k}) = \iint e^{i\vec{k}_i\cdot(\vec{r}-\vec{\delta}_{mn})} \cdot e^{-i\vec{k}\cdot\vec{r}} d^2\vec{r}$$

where the integral is over the entire plane.

We evaluate the integral by summing the contribution from individual unit cells. Specifically, in the (m, n)-th unit cell which is centered at $\vec{R}_{m,n} = m\cdot\vec{A}_1 + n\cdot\vec{A}_2$, we define a reduced position vector $\vec{r}_0 = \vec{r} - \vec{R}_{m,n}$, and we express the integral in terms of $\vec{r}_0$.

$$F_i(\vec{k}) = \sum_{m,n} F_i^{mn}(\vec{k}) = \sum_{m,n} \iint_{u.c.} e^{i\vec{k}_i\cdot\left(\vec{r}_0+\vec{R}_{m,n}-m\cdot\vec{\delta}_1-n\cdot\vec{\delta}_2\right)} \cdot e^{-i\vec{k}\cdot(\vec{r}_0+\vec{R}_{m,n})} d^2\vec{r}_0$$

$$= \sum_{m,n} e^{i\vec{k}_i\cdot\left(\vec{R}_{m,n}-m\cdot\vec{\delta}_1-n\cdot\vec{\delta}_2\right)-i\vec{k}\cdot\vec{R}_{m,n}} \iint_{u.c.} e^{i(\vec{k}_i-\vec{k})\cdot\vec{r}_0}\, d^2\vec{r}_0$$

$$= \sum_{m,n} e^{i\vec{k}_i\cdot\left(\vec{R}_{m,n}-m\cdot\vec{\delta}_1-n\cdot\vec{\delta}_2\right)-i\vec{k}\cdot\vec{R}_{m,n}}\, F_i^{00}(\vec{k})$$

Note that $F_i^{00}(\vec{k}) \equiv \iint_{u.c.} e^{i(\vec{k}_i-\vec{k})\cdot\vec{r}_0}\, d^2\vec{r}_0$ is simply the integral within the (0, 0)-th unit cell which is a constant independent of *m* and *n*. We then have

$$F_i(\vec{k}) = F_i^{00}(\vec{k}) \sum_{m,n} e^{i\vec{k}_i \cdot \left(\vec{R}_{m,n} - m\cdot\vec{\delta}_1 - n\cdot\vec{\delta}_2\right) - i\vec{k}\cdot\vec{R}_{m,n}}$$

$$= F_i^{00}(\vec{k}) \sum_{m,n} e^{i[(\vec{k}_i - \vec{k})\cdot(m\cdot\vec{A}_1 + n\cdot\vec{A}_2) - m\vec{k}_i\cdot\vec{\delta}_1 - n\vec{k}_i\cdot\vec{\delta}_2]}$$

$$= F_i^{00}(\vec{k}) \sum_{m} e^{im\cdot\left((\vec{k}_i - \vec{k})\cdot\vec{A}_1 - \vec{k}_i\cdot\vec{\delta}_1\right)} \sum_{n} e^{in\cdot\left((\vec{k}_i - \vec{k})\cdot\vec{A}_2 - \vec{k}_i\cdot\vec{\delta}_2\right)}$$

$$= F_i^{00}(\vec{k}) \frac{1 - e^{iM[(\vec{k}_i - \vec{k})\cdot\vec{A}_1 - \vec{k}_i\cdot\vec{\delta}_1]}}{1 - e^{i[(\vec{k}_i - \vec{k})\cdot\vec{A}_1 - \vec{k}_i\cdot\vec{\delta}_1]}} \frac{1 - e^{iN[(\vec{k}_i - \vec{k})\cdot\vec{A}_2 - \vec{k}_i\cdot\vec{\delta}_2]}}{1 - e^{i[(\vec{k}_i - \vec{k})\cdot\vec{A}_2 - \vec{k}_i\cdot\vec{\delta}_2]}}$$

$$\left|F_i(\vec{k})\right| = \frac{\sin\left(\frac{M}{2}[(\vec{k}_i - \vec{k})\cdot\vec{A}_1 - \vec{k}_i\cdot\vec{\delta}_1]\right)}{\sin\left(\frac{1}{2}[(\vec{k}_i - \vec{k})\cdot\vec{A}_1 - \vec{k}_i\cdot\vec{\delta}_1]\right)} \cdot \frac{\sin\left(\frac{N}{2}[(\vec{k}_i - \vec{k})\cdot\vec{A}_2 - \vec{k}_i\cdot\vec{\delta}_2]\right)}{\sin\left(\frac{1}{2}[(\vec{k}_i - \vec{k})\cdot\vec{A}_2 - \vec{k}_i\cdot\vec{\delta}_2]\right)} F_i^{00}(\vec{k})$$

The peak positions of $\left|F_i(\vec{k})\right|$, denoted as $\vec{k}_i'$, satisfy the conditions:

$$(\vec{k}_i - \vec{k}_i')\cdot\vec{A}_1 - \vec{k}_i\cdot\vec{\delta}_1 = 0 \;\;\&\;\; (\vec{k}_i - \vec{k}_i')\cdot\vec{A}_2 - \vec{k}_i\cdot\vec{\delta}_2 = 0$$

Define the reciprocal vectors $\vec{k}_{A1}$ and $\vec{k}_{A2}$ as

$$\vec{k}_{A1} = \frac{\vec{A}_2 \times \vec{e}_z}{\left|\vec{A}_1 \times \vec{A}_2\right|}$$

$$\vec{k}_{A2} = \frac{\vec{e}_z \times \vec{A}_1}{\left|\vec{A}_1 \times \vec{A}_2\right|}$$

And they satisfy the relations $\vec{k}_{A1}\cdot\vec{A}_1 = 1$ and $\vec{k}_{A2}\cdot\vec{A}_2 = 1$. We can then obtain

$$\vec{k}_i - \vec{k}_i' = \vec{k}_{A1}\cdot(\vec{k}_i\cdot\vec{\delta}_1) + \vec{k}_{A2}\cdot(\vec{k}_i\cdot\vec{\delta}_2)$$

or

$$\vec{k}_i' = \vec{k}_i - [\vec{k}_{A1}\cdot(\vec{k}_i\cdot\vec{\delta}_1) - \vec{k}_{A2}\cdot(\vec{k}_i\cdot\vec{\delta}_2)]$$

We can see that the Fourier peak positions of the discontinuous lattice, $\vec{k}_i'$, are shifted from those for a continuous lattice, $\vec{k}_i$, by a vector that depends on the displacement vectors, $\vec{\delta}_1$ and $\vec{\delta}_2$, and the reciprocal vectors corresponding to the moiré-L lattice, $\vec{k}_{A1}$ and $\vec{k}_{A2}$.

Experimentally, we can find $\vec{k}_i'$ from the Fourier transform of the entire image containing large number of moiré-L unit cells, and $\vec{k}_i$ can be determined from the Fourier transform of the data within individual moiré-L unit cells. $\vec{k}_{A1}$ and $\vec{k}_{A2}$ can also be determined by extracting the unit vectors for the moiré-L lattice. From these, we can then determine the displacement vectors, $\vec{\delta}_1$ and $\vec{\delta}_2$. Alternatively, $\vec{\delta}_1$ and $\vec{\delta}_2$ can also be determined by comparing the moiré-S lattice patterns in neighboring moiré-L unit cells. The results from these two methods match very well.

References

[1] X. Huang, L. Chen, S. Tang, C. Jiang, C. Chen, H. Wang, Z. X. Shen, H. Wang, and Y. T. Cui, *Imaging Dual-Moiré Lattices in Twisted Bilayer Graphene Aligned on Hexagonal Boron Nitride Using Microwave Impedance Microscopy*, Nano Lett. **21**, 4292 (2021).

[2] S. Tang et al., *Precisely Aligned Graphene Grown on Hexagonal Boron Nitride by Catalyst Free Chemical Vapor Deposition*, Sci. Rep. **3**, 2666 (2013).

[3] L. A. Ponomarenko et al., *Cloning of Dirac Fermions in Graphene Superlattices*, Nature **497**, 594 (2013).

[4] G. L. Yu et al., *Hierarchy of Hofstadter States and Replica Quantum Hall Ferromagnetism in Graphene Superlattices*, Nat. Phys. **10**, 525 (2014).

[5] B. Hunt et al., *Massive Dirac Fermions and Hofstadter Butterfly in a van Der Waals Heterostructure*, Science (80-.). **340**, 1427 (2013).

[6] R. Bistritzer and A. H. MacDonald, *Moiré Bands in Twisted Double-Layer Graphene*, Proc. Natl. Acad. Sci. U. S. A. **108**, 12233 (2011).

[7] Y. Cao, V. Fatemi, S. Fang, K. Watanabe, T. Taniguchi, E. Kaxiras, and P. Jarillo-Herrero, *Unconventional Superconductivity in Magic-Angle Graphene Superlattices*, Nature **556**, 43 (2018).

[8] Y. Cao et al., *Correlated Insulator Behaviour at Half-Filling in Magic-Angle Graphene Superlattices*, Nature **556**, 80 (2018).

[9] Y. T. Cui et al., *Unconventional Correlation between Quantum Hall Transport Quantization and Bulk State Filling in Gated Graphene Devices*, Phys. Rev. Lett. **117**, 1 (2016).

[10] X. Wu, *Development and Applications of Microwave Impedance Microscopy for Imaging Emergent Properties in Quantum Materials*, PhD Thesis (2018).

[11] X. Huang et al., *Correlated Insulating States at Fractional Fillings of the WS2/WSe2 Moiré Lattice*, Nat. Phys. (2021).

[12] S. Xu et al., *Tunable van Hove Singularities and Correlated States in Twisted Monolayer–Bilayer Graphene*, Nat. Phys. **17**, 619 (2021).

[13] S. Chen et al., *Electrically Tunable Correlated and Topological States in Twisted Monolayer–Bilayer Graphene*, Nat. Phys. **17**, 374 (2021).

[14] Z. Chu et al., *Nanoscale Conductivity Imaging of Correlated Electronic States in WSe2/WS2 Moiré Superlattices*, Phys. Rev. Lett. **125**, 186803 (2020).

[15] C. Shen et al., *Correlated States in Twisted Double Bilayer Graphene*, Nat. Phys. **16**, 520 (2020).

[16] L. Balents, C. R. Dean, D. K. Efetov, and A. F. Young, *Superconductivity and Strong Correlations in Moiré Flat Bands*, Nat. Phys. **16**, 725 (2020).

[17] Y. Xu, S. Liu, D. A. Rhodes, K. Watanabe, T. Taniguchi, J. Hone, V. Elser, K. F. Mak, and J. Shan, *Correlated Insulating States at Fractional Fillings of Moiré Superlattices*, Nature **587**, 214 (2020).

[18] E. C. Regan et al., *Mott and Generalized Wigner Crystal States in WSe2/WS2 Moiré Superlattices*, Nature **579**, 359 (2020).

[19] Y. Tang et al., *Simulation of Hubbard Model Physics in WSe2/WS2 Moiré Superlattices*, Nature **579**, 353 (2020).

[20] Y. Shimazaki, I. Schwartz, K. Watanabe, T. Taniguchi, M. Kroner, and A. Imamoğlu, *Strongly Correlated Electrons and Hybrid Excitons in a Moiré Heterostructure*, Nature **580**, 472 (2020).

[21] X. Liu et al., *Tunable Spin-Polarized Correlated States in Twisted Double Bilayer Graphene*, Nature **583**, 221 (2020).

[22] Y. Cao, D. Rodan-Legrain, O. Rubies-Bigorda, J. M. Park, K. Watanabe, T. Taniguchi, and P. Jarillo-Herrero, *Tunable Correlated States and Spin-Polarized Phases in Twisted Bilayer–Bilayer Graphene*, Nature **583**, 215 (2020).

[23] G. Chen et al., *Evidence of a Gate-Tunable Mott Insulator in a Trilayer Graphene Moiré Superlattice*, Nat. Phys. **15**, 237 (2019).

[24] G. Chen et al., *Signatures of Tunable Superconductivity in a Trilayer Graphene Moiré Superlattice*, Nature **572**, 215 (2019).

[25] C. Jin et al., *Observation of Moiré Excitons in WSe2/WS2 Heterostructure Superlattices*, Nature **567**, 76 (2019).

[26] S. S. Sunku et al., *Photonic Crystals for Nano-Light in Moiré Graphene Superlattices*, Science (80-.). **362**, 1153 (2018).

[27] G. Chen et al., *Tunable Correlated Chern Insulator and Ferromagnetism in a Moiré Superlattice*, Nature **579**, 56 (2020).

[28] H. Polshyn et al., *Electrical Switching of Magnetic Order in an Orbital Chern Insulator*, Nature **588**, 66 (2020).

[29] L. Wang, S. Zihlmann, M. H. Liu, P. Makk, K. Watanabe, T. Taniguchi, A. Baumgartner, and C. Schönenberger, *New Generation of Moiré Superlattices in Doubly Aligned HBN/Graphene/HBN Heterostructures*, Nano Lett. **19**, 2371 (2019).

[30] Z. Wang et al., *Composite Super-Moiré Lattices in Double-Aligned Graphene Heterostructures*, Sci. Adv. **5**, 1 (2019).

[31] M. Andelkovic, S. P. Milovanović, L. Covaci, and F. M. Peeters, *Double Moiré with a Twist: Supermoiré in Encapsulated Graphene*, Nano Lett. **20**, 979 (2020).

[32] J. S. Alden, A. W. Tsen, P. Y. Huang, R. Hovden, L. Brown, J. Park, D. A. Muller, and P. L. McEuen, *Strain Solitons and Topological Defects in Bilayer Graphene*, Proc. Natl. Acad. Sci. U. S. A. **110**, 11256 (2013).

[33] H. Yoo et al., *Atomic and Electronic Reconstruction at the van Der Waals Interface in Twisted Bilayer Graphene*, Nat. Mater. **18**, 448 (2019).

[34] G. Li, A. Luican, J. M. B. Lopes Dos Santos, A. H. Castro Neto, A. Reina, J. Kong, and E. Y. Andrei, *Observation of Van Hove Singularities in Twisted Graphene Layers*, Nat. Phys. **6**, 109 (2010).

[35] M. Yankowitz, J. Xue, D. Cormode, J. D. Sanchez-Yamagishi, K. Watanabe, T. Taniguchi, P. Jarillo-Herrero, P. Jacquod, and B. J. Leroy, *Emergence of Superlattice Dirac Points in Graphene on Hexagonal Boron Nitride*, Nat. Phys. **8**, 382 (2012).

[36] A. Kerelsky et al., *Maximized Electron Interactions at the Magic Angle in Twisted Bilayer Graphene*, Nature **572**, 95 (2019).

[37] Y. Choi et al., *Electronic Correlations in Twisted Bilayer Graphene near the Magic Angle*, Nat. Phys. **15**, 1174 (2019).

[38] Y. Xie, B. Lian, B. Jäck, X. Liu, C. Chiu, K. Watanabe, T. Taniguchi, B. A. Bernevig, and A. Yazdani, *Spectroscopic Signatures of Many-Body Correlations in Magic-Angle Twisted Bilayer Graphene*, Nature **572**, 101 (2019).

[39] Y. Jiang, X. Lai, K. Watanabe, T. Taniguchi, K. Haule, J. Mao, and E. Y. Andrei, *Charge Order and Broken Rotational Symmetry in Magic-Angle Twisted Bilayer Graphene*, Nature **573**, 91 (2019).

[40] L. J. McGilly et al., *Visualization of Moiré Superlattices*, Nat. Nanotechnol. **15**, 580 (2020).

[41] Z. Yu, A. Song, L. Sun, Y. Li, L. Gao, H. Peng, T. Ma, Z. Liu, and J. Luo, *Understanding Interlayer Contact Conductance in Twisted Bilayer Graphene*, Small **16**, (2020).

[42] P. Gallagher et al., *Switchable Friction Enabled by Nanoscale Self-Assembly on Graphene*, Nat. Commun. **7**, 1 (2016).

[43] C. R. Woods et al., *Commensurate–Incommensurate Transition in Graphene on Hexagonal Boron Nitride*, Nat. Phys. **10**, 451 (2014).

[44] S. Zhang et al., *Abnormal Conductivity in Low-Angle Twisted Bilayer Grapheme*, Sci. Adv. **6**, (2020).

[45] Y. Luo, R. Engelke, M. Mattheakis, M. Tamagnone, S. Carr, K. Watanabe, T. Taniguchi, E. Kaxiras, P. Kim, and W. L. Wilson, *In Situ Nanoscale Imaging of Moiré Superlattices in Twisted van Der Waals Heterostructures*, Nat. Commun. **11**, 1 (2020).

[46] K. Lai, W. Kundhikanjana, M. A. Kelly, and Z. X. Shen, *Nanoscale Microwave Microscopy Using Shielded Cantilever Probes*, Appl. Nanosci. **1**, 13 (2011).

[47] Y. T. Cui, E. Y. Ma, and Z. X. Shen, *Quartz Tuning Fork Based Microwave Impedance Microscopy*, Rev. Sci. Instrum. **87**, (2016).

[48] D. A. Scrymgeour, A. Baca, K. Fishgrab, R. J. Simonson, M. Marshall, E. Bussmann, C. Y. Nakakura, M. Anderson, and S. Misra, *Determining the Resolution of Scanning Microwave Impedance Microscopy Using Atomic-Precision Buried Donor Structures*, Appl. Surf. Sci. **423**, 1097 (2017).

[49] K. Lee et al., *Ultrahigh-Resolution Scanning Microwave Impedance Microscopy of Moiré Lattices and Superstructures*, Sci. Adv. **6**, 1 (2020).

[50] D. A. A. Ohlberg et al., *The Limits of near Field Immersion Microwave Microscopy Evaluated by Imaging Bilayer Graphene Moiré Patterns*, Nat. Commun. **12**, 8 (2021).

[51] D. A. A. Ohlberg et al., *Observation of Moiré Superlattices on Twisted Bilayer Graphene by Scanning Microwave Impedance Microscopy*, in *Low-Dimensional Materials and Devices 2020*, edited by N. P. Kobayashi, A. A. Talin, A. V. Davydov, and M. S. Islam (SPIE, 2020), p. 15.

Chapter 4 Correlated Insulating States at Fractional Fillings of the WS_2/WSe_2 Moiré Lattice

4.1 Semiconducting Transitional Metal Dichalcogenide (TMD) Materials and Moiré Superlattices

4.1.1 2H-Phase TMD Materials with Electronic Band Structure and Optical Properties

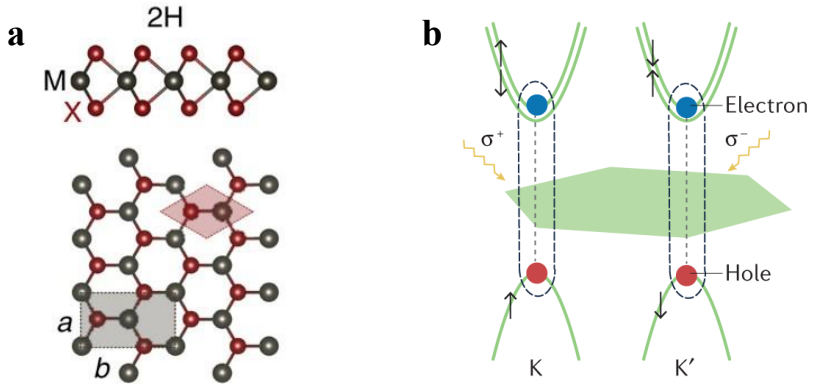

Figure 4.1 Semiconducting TMD materials and band structure. a, Monolayer TMD in 2H-phase. **b**, Bright excitons at K and K' valleys the Brillouin zone. Black arrows indicate the spin configuration of each band. Large (small) spin splitting in valance (conduction) band. Circularly polarized light coupled to excitons at K and K' valleys, respectively. Panel **a** adapted from REF 32, copyright Springer Nature. Panel **b** adapted from REF 6, copyright Springer Nature.

2H-phase TMD materials (here we focus on compounds with M: W, Mo; X: S, Se) are layered semiconducting materials. They are composed of covalently bonded X-W-X layers with an interlayer van der Waals forces. The structure for 2H-phase TMD monolayer is shown in Fig. 4.1a and, when viewed along the out-of-plane direction, it forms a perfect hexagonal lattice with sublattice site X and M atoms [1]. 2H-phase bulk MX_2 crystal has Bernal-stacked monolayers and preserves an inversion symmetry. Bulk MX2 has an indirect energy gap ranging from near infrared to visible light [2,3]. When thinned down to the monolayer limit, they change from indirect to direct bandgap semiconductors with

band extrema locating at K and K' corners of the Brillouin zone [4,5] as shown in Fig. 4.1b. Monolayer MX_2 lacks inversion symmetry and has strong spin-orbit coupling [6]. *d* orbitals from the transitional metal atoms at these *k*-space corners allow strong spin-orbit coupling, thus leading to large valance band spin splitting (~0.2 eV for MoX_2; ~0.4 eV for WX_2). This spin splitting effect in conduction band is smaller. Considering time-reversal symmetry, the spin-splitting has opposite signs between these high symmetric K and K' valleys in the Brillouin zone. The spin and valley degree of freedoms are locked which enables the access of spin information via knowledge of valley.

Under optical excitation, electrons can be pumped from the valance band to conduction band while leaving holes in the valance band (Fig. 4.1b). Since dielectric screening of the electronic Coulomb interaction is reduced in 2D, tightly bonded electron-hole pairs (exciton states) can form and dominate the optical properties of monolayer TMDs. Electrons and holes at the K and K' valleys can form momentum-direct excitons. Two bright exciton states from the optical transition between valance and conduction bands of the same spin state are labeled A/B excitons with a lower/higher energy. Using circularly polarized light (σ^+ or σ^-), electrons can be selectively pumped at K or K' valleys. This has been extensively utilized to study the charge carrier spin status (spin-valley locking) in RMCD [see experiment method] experiments on TMD materials.

4.1.2 Moiré Potential and Electronic Flat Mini Bands

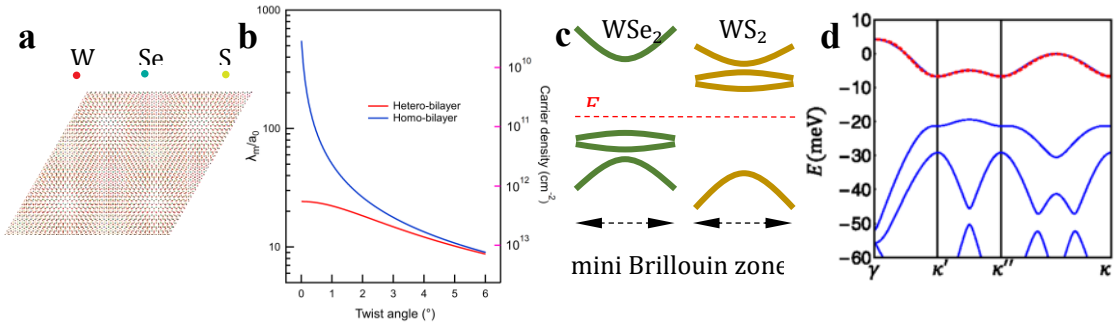

Figure 4.2 Moiré superlattice and band engineering. a, Moiré pattern in an angle-aligned WS_2/WSe_2 hetero-bilayer. **b**, moiré periodicity as a function of twist angle for homo-/hetero bilayer (WS_2/WSe_2 and WSe_2/WSe_2), respectively. Note that the periodicity is plotted in unit of atomic lattice constant. Carrier density is plotted in log scale. **c**, Moiré potential induced flat electronic band in the mini-Brillouin zone for two layers in WS_2/WSe_2. **d**, Calculated electronic valance bands for a 2°-twisted $WSe_2/MoSe_2$ moire superlattice. The highest valance moiré band (red) has a narrow bandwidth ~11 meV. Panel **d** adapted from REF 9, copyright APS.

With developed fabrication techniques, semiconducting TMD materials can be easily shaped into monolayers. Second-harmonic generation (SHG) can be used to determine the individual crystal orientation for making hetero-bilayers while tear-and-stack techniques [7] have been used for homo-bilayers. Twisting TMD homo-bilayer or stacking hetero-bilayer without twist can generate a moiré pattern with a periodicity on nanometer scale. **Fig. 4.2a** shows a moire pattern formed in an aligned WS_2/WSe_2 hetero-bilayer (to be noticed that a larger lattice mismatch is chosen to better illustrate the moire pattern). A moiré pattern here is basically a periodic atomic alignment between two layers. Interlayer hybridization varies in the period of moiré superlattice and creates a new periodic potential for electrons in the system. At small twist angles, the moiré period can be calculated as a function of the lattice mismatch and twist angles in the following equation:

$$\lambda_m \cong a_0/\sqrt{\delta^2 + \theta^2}$$

with lattice mismatch: $\delta = |a_0' - a_0|/a_0$ (a_0 and a_0' are the lattice constants of the two layers) and twist angle: θ. A typical moiré periodicity can be from several nanometer to tens of nanometer, much larger than the pristine atomic lattice periodicity. **Fig. 4.2b** shows the moire periodicity for both homo- and hetero-bilayer TMD systems. It's worth noting that angle-aligned (0 or 60°) TMD hetero-bilayer moiré lattice has a periodicity less sensitive to twist angle disorder. Experimentally, atomic defects are inescapable in TMD monolayers. The cleanest WSe_2 crystals (by self-flux growth method) contain defects with a density of ~10^{11} cm^{-2} Ref [6,8]. With aligned hetero-bilayer (WS_2/WSe_2) or $4 - 5°$ twisted WSe_2 homo-bilayer, the moire density is much higher than that as can be seen from **Fig. 4.2b**.

Usually, the moire potential maxima and minima are centered at high-symmetric sites in the moiré unit cell. This artificial superlattice potential can dramatically modify the electronic properties of the system. The resulting larger periodic potential will fold the energy bands into a mini-Brillouin zone. Energy gap will open at these band crossings of the mini-BZ boundary, as demonstrated in **Fig. 4.2c** for WS_2/WSe_2. Isolated moiré flat bands will form in such a circumstance. Theoretically studies have predicted flat electronic bands in semiconducting TMD moiré systems [9,10], such as an isolated flat valance moire band with a bandwidth of ~11 meV in a 2°-twisted $WSe_2/MoSe_2$ moire superlattice (shown in **Fig. 4.2d** from Ref [9]). The moiré potential can been experimentally observed as modulation of valance band edge by scanning tunneling spectroscopy and can be as large as hundreds of meV [11,12]. Lattice relaxation and strain effects have been observed since TMD layers have a small Young's modulus. The interlayer stacking energy also varies at

positions across the moiré unit cell. Domains with energetically preferred stacking configurations will expand and be separated by domain-wall networks to accommodate the lattice mismatch [13–15]. In a recent STS study on $MoSe_2/WSe_2$ hetero-bilayer, the moiré periodicity ranges from 2 nm to greater than 20 nm and a deeper moiré potential (up to several hundred meV) has been observed than theoretical prediction without considering lattice reconstruction [11]. Such a deep potential will further localize carriers and enhance the correlation effect.

Electronic system with such a flat energy band could present strong correlation effect. The *e*-*e* Coulomb interaction can be estimated as $U \approx {e^2}/{4\pi\varepsilon\lambda_m}$ with the kinetic energy for electrons (band width) as $W \approx {\hbar^2 k^2}/{2m_e^*} \approx {\hbar^2\pi^2}/{2m_e^*\lambda_m^2}$ (m_e^* is the effective electron mass, $\sim 0.5\, m_0$ in monolayer MX_2). Thus, the parameter characterizing the correlation strength is

$$U/W \propto m_e^* \cdot \lambda_m.$$

In TMD moiré systems, a strong correlation effect can be readily realized with sufficiently large $m_e^* \cdot \lambda_m$. In particular, the isolated valance flat-band can be mapped to generalized triangular lattice Hubbard models [9]. Considering the valance moiré flat band in hetero-bilayer TMD, the total degeneracy is two from the valley degree (large spin splitting for valance band). As shown in **Fig. 4.3**, at half filling (one hole per moiré lattice site), the system will tend to avoid double occupancy due to the large on-site

Coulomb repulsion between electrons and hence form a Mott insulating state.

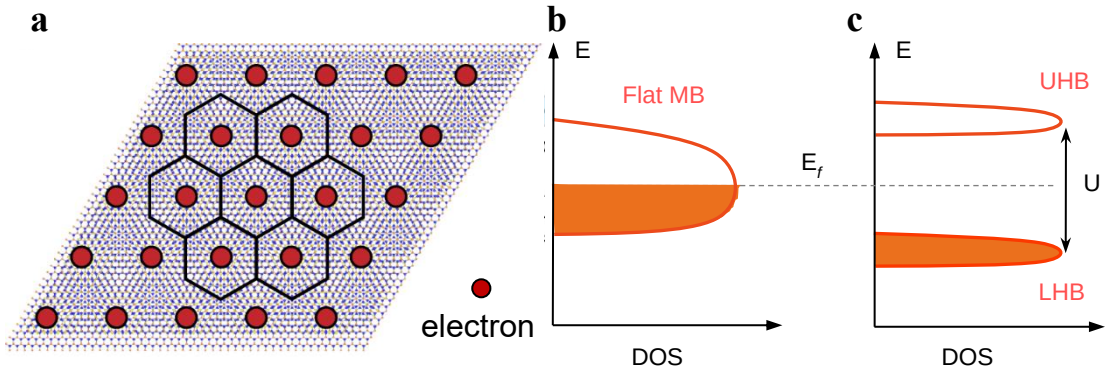

Figure 4.3 Mott insulator and Hubbard bands. a, Moiré superlattice at filled with one charge carriers per lattice site. **b-c**, Half-filled flat moiré band split into two sub bands: upper and lower Hubbard bands. Panel **a** adapted from REF 20, copyright Springer Nature.

4.2 Recent Research on Correlated Insulating States in Semiconducting TMD Moiré System

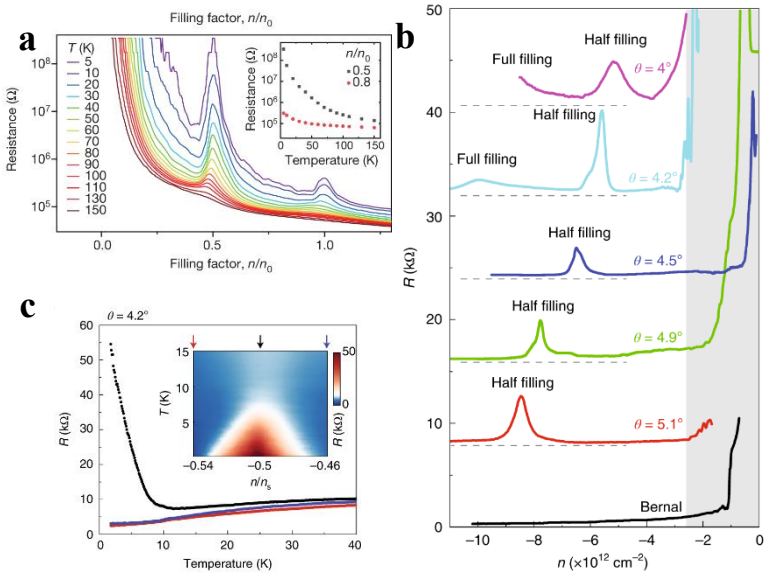

Figure 4.4 Mott insulator states in TMD hetero- and homo-bilayers. a, Two-terminal resistance of a WSe_2/WS_2 moire superlattice as a function of filling in the first valance moire band at different temperatures (1 means full filling). **b**, Sample resistivity of twisted WSe_2 homo-bilayers as function of hole density (measured at 1.8 K). **c**, Resistivity of 4.2°-twisted device as a function of temperature, highlighting the insulating nature of the peak feature. Panel **a** adapted from REF 16, copyright Springer Nature. Panel **b-c** adapted from REF 17, copyright Springer Nature.

Soon after the exciting discovery of correlated insulating states and superconductivity in MATBG in 2018, TMD moiré systems have been predicted as another intriguing platform to realize many-body phenomena with much stronger correlation. Like other 2D materials, TMD moiré system can easily be made into planar device geometry with electro-static gates to change the carrier density. However, the large contact resistance in TMD devices has made it challenging to probe these correlated insulating states via transport measurements. A few groups have managed to probe the Mott insulator states through measuring two-terminal resistance at hole doping side [16,17] [Note 1]. In study [16]

of WSe_2/WS_2 (shown in **Fig. 4.4a**), the temperature-dependent two-terminal resistance data of the constituting WSe_2 layer shows prominent resistive peaks as well as the background of increasing contact resistance at lower fillings (smaller carrier densities). Two resistive peaks are clearly observed with one at larger carrier density and the other at a half density value. The calibrated filling factor (ν, number of carriers per moiré unit cell, +/- for electrons/holes) for the resistive peak at higher density is $\nu = -2$ [2-fold degeneracy from valley degree] and confirms its nature of a band insulator when fully filled. The new peak at half filling ($\nu = -1$) indicates the presence of a Mott insulator at half filling, which is also shown in the modulation of the WSe_2 A-exciton peak amplitude. In the other research on twisted WSe_2 homobilayers [17], evidence of flat moiré valance miniband have been reported with a correlated insulator state at half filling and tunable with both twist angle (θ ranging from 4 to 5.1°) and electric displacement field (**Fig. 4.4b**). Shown in **Fig. 4.4c**, a representative temperature-dependent data (at $\theta = 4.2°$) clearly shows the insulating behavior at half filling with metallic states when doped away from that filling ($\nu = -0.54\ or\ -0.46$).

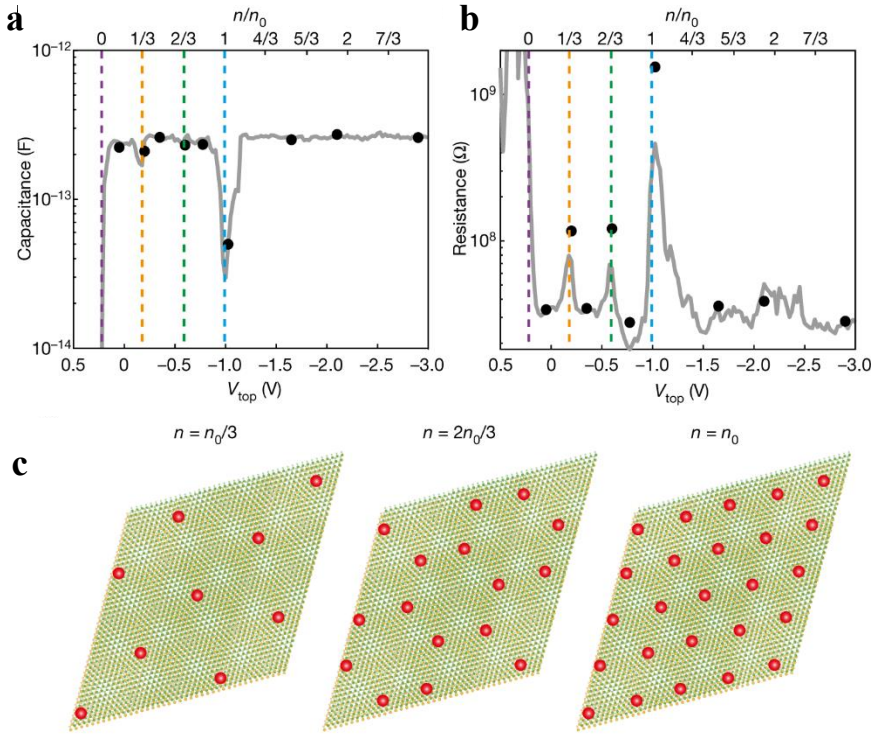

Figure 4.5 Generalized Wigner crystal states in a TMD hetero-bilayer. a, Capacitance and **b**, resistance of WSe_2/WS_2 moire superlattice as function of gate voltage and hole doping factor (2 for full filling). **c**, Illustrations of Mott insulating state ($n = -1$) generalized Wigner crystal states ($n = -\frac{1}{3}$ and $-\frac{2}{3}$). Panel **a-c** adapted from REF 18, copyright Springer Nature.

Excitons' extreme sensitivity to local carrier density and dielectric environment enables researchers to probe the electronic properties of WSe_2/WS_2 moiré systems [16,18]. In the research of Ref [18], researchers are able to optically detect the resistance and capacitance (Fig. 4.5) of the moiré system through WSe_2 exciton absorption. Besides the Mott insulating state at $\nu = -1$, insulator states are also shown at $\nu = -\frac{1}{3}$ & $-\frac{2}{3}$ which they assigned to generalized Wigner crystal states. Due to strong *e-e* interaction at neighboring superlattice sites, electrons form a crystalized state. The original idea of Wigner crystal talks about behaviors of electrons without any underlying lattice. When the electron densities are reduced, the *e-e* interaction will dominate its kinetic energy and the

system will have a chance form an electron crystal below a critical electron density. In a 2D case, electrons will form a crystal with a triangular lattice symmetry.

Recent progress has been achieved in transport measurement of TMD moiré systems in dual-gated structure. Heavily dope carriers in the contact region. Choice of suitable metal with work function matching that of TMD layers. Higher doping density but mainly at hole-doping side.

4.3 Observing a Series of Correlated Insulating States at Fractional Fillings of the WS_2/WSe_2 Moiré Superlattice by Microwave Impedance Microscopy

The content of this research was published in my co-first authored paper, in which my contribution includes MIM measurements, data analysis and input for manuscript writing.

Huang, X., Wang, T., Miao, S. et al. Correlated insulating states at fractional fillings of the WS2/WSe2 moiré lattice. Nat. Phys. 17, 715–719 (2021).

In this study, we report the observation of a series of correlated insulating states at both *e*- and *h*-doped regimes in a WS_2/WSe_2 hetero-bilayer moiré system, including Mott insulating states at fillings of $\nu = \pm 1$ and even states at fractional fillings of $\nu = +\frac{1}{6}, \pm\frac{1}{4}, \pm\frac{1}{3}, \pm\frac{1}{2}, \pm\frac{2}{3}, \pm\frac{3}{4}, +\frac{5}{6}$ & $\pm\frac{3}{2}$. Monte Carlo simulations of a Coulomb gas model suggest that these fractional-filling states correspond to long-range orderings of electrons in the moiré lattice with various spatial patterns (triangular and stripe phases). The transition temperature for $\nu = \pm\frac{1}{3}$ and $\pm\frac{2}{3}$ can be as high as 120 K. Additional correlated

insulators at fillings of $\nu = -\frac{8}{9}, -\frac{5}{6}, -\frac{7}{9}, +\frac{5}{9}$ and $+\frac{6}{7}$ also confirm the unexpected strong electron interaction in this moire system.

4.3.1 Device Fabrication and Measurement Setup

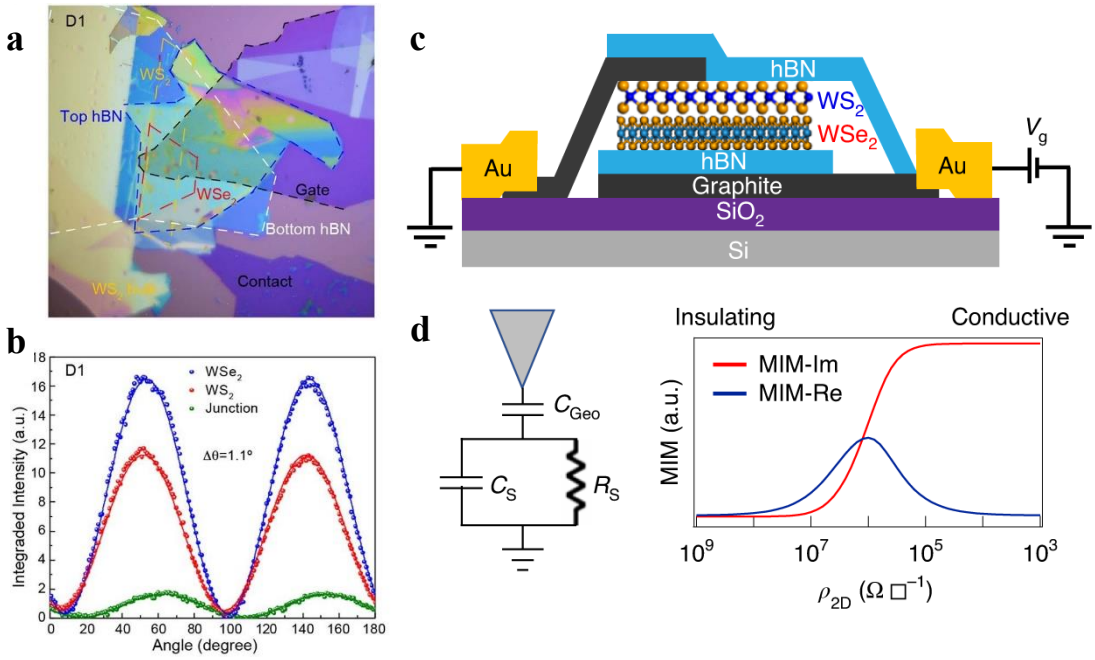

Figure 4.6 MIM on TMD hetero-bilayer moiré superlattice. a, Optical image for ***Dev1***. **b**, SHG signal for ***Dev1*** with a twist angle of ~1.1°. A much smaller SHG in the heterostructure region further indicating the alignment of ~60°. **c**, Illustration for device structure. **d**, Left: Effect circuit model for the tip-sample impedance (C_S and R_S) probed in MIM. Right: typical response curves for MIM-Im and MIM-Re as a function of sample 2D resistivity. Panel **a-d** adapted from REF 20, copyright Springer Nature.

The high-quality bulk crystals of WS_2 and WSe_2 were purchased from HQ Graphene and were used to exfoliate monolayers. The crystal axes are determined by optical second harmonic generation measurements (see **Fig. 4.6c** for angle alignment of ***Dev1***). Note that 0° device (***Dev2***) with a large SHG signal while 60° device (***Dev1***) with a small one [16]. A typical structure of the device studied is shown in **Fig. 4.6a**. Angle-

aligned (0 or 60°) monolayers WS_2 and WSe_2 are encapsulated by hBN flakes. Thin graphite flakes are used as both the electric contacts and bottom gate electrodes. Given the lattice constant for each layer (WS_2 : 3.15 Å; WSe_2: 3.28 Å and the lattice mismatch ~4%), the moiré periodicity will be around 8 nm in aligned hetero-bilayers (**Fig. 4.2b**). The hetero-bilayer has a type-II band alignment with the low energy valance band from WSe_2 and conduction band from WS_2 (**Fig. 4.2c**). In principle, moiré flat minibands should form on both the *e*- and *h*-doped sides with valance band maximum from WSe_2 and conduction band minimum from WS_2. We expect correlated insulating states from both doping sides, and we use scanning MIM to probe these insulating states through its capability to sense local sample resistivity. In MIM measurement, a microwave signal (from 1 – 10 GHz) is routed to a sharp metal tip and the reflected signal is analyzed to extract the imaginary and real parts of the complex tip-sample impedance, named as MIM-Im and MIM-Re, respectively. As the tip voltage oscillates, carriers in the sample move towards and away from the tip to screen the microwave a.c. electric fields. Such screening capability is characterized by the MIM-Im signal. The MIM-Re signal, on the other hand, characterizes the energy dissipation generated by the oscillating current induced in the sample. Normally, the samples we study experience a large change in its local resistivity while the change in permittivity is minimal. Thus, in the simulation with a fixed permittivity, the resistivity response curves for both channels are shown in **Fig. 4.6d**. Particularly, MIM-Im decreases monotonically with increasing resistivity within a finite sensitivity window and becomes saturated outside (saturates to a lower value at more insulating side and to a higher value at more metallic side). We performed MIM measurements by parking the tip at fixed

positions over the sample while sweeping the back gate voltage. The carrier density is tuned upon changing of the gate voltage.

4.3.2 Mott Insulator States and Generalized Wigner Crystal States at Both *e*- and *h*-Doped Sides

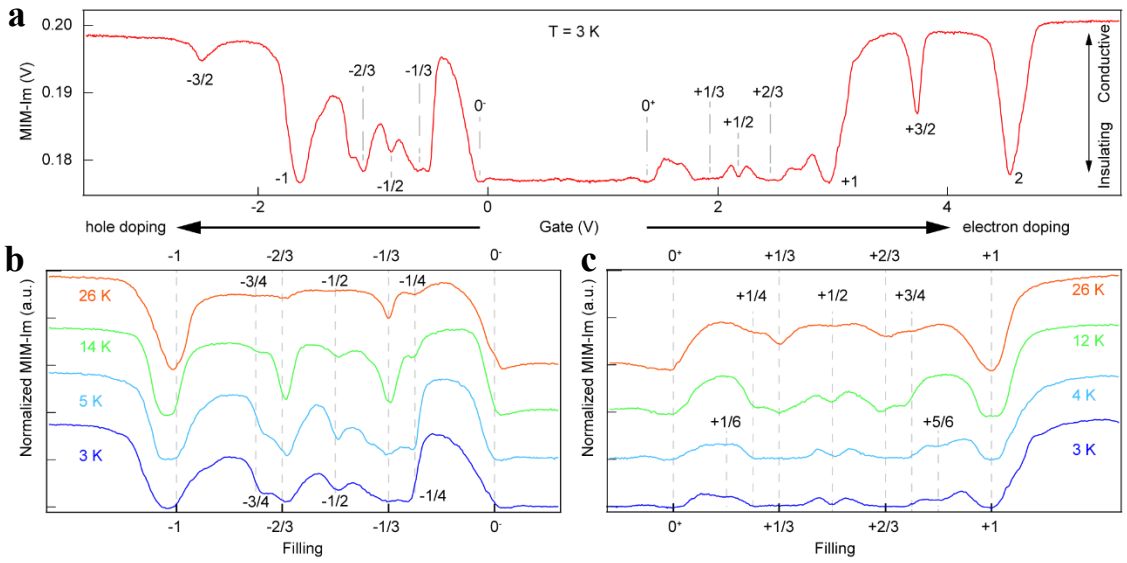

Figure 4.7 Spectrum of the correlated insulating states. a, MIM-Im curve as a function of back gate voltage taken on Dev1 at 3 K. **b**, and **c**, MIM-Im curves as a function of calibrated filling fraction at selected temperatures for *h*- and *e*-doping sides, respectively. Panel **a-c** adapted from REF 20, copyright Springer Nature.

A representative MIM-Im in ***Dev1*** is shown in Fig. 4.7a at a temperature of 3 K. At large gate voltages ($V_g > 5$ V or $V_g < -3$ V), the system is highly *e*- or *h*-doped and become very conductive. A saturated high MIM-Im signal is observed on both sides. As the gate voltage is reduced from either side with a reduced doping carrier density, the sample becomes more insulating with a decreasing MIM-Im signal. During this process, a series of insulating states manifest as dip features. With the device geometry, we can

determine the relative carrier density change in the gate voltage. The calculation is based on a parallel capacitor model and the relative change (Δn) in carrier density is

$$\Delta n = \varepsilon_0 \varepsilon_r \Delta V_g / ed,$$

where ε_0: the vacuum permittivity; ε_r: dielectric constant for dielectric material ($3-4$ for hBN); d: the thickness of dielectric material. Before assignment of the actual filling factor for these correlated insulating states, we need to first determine the band extrema.

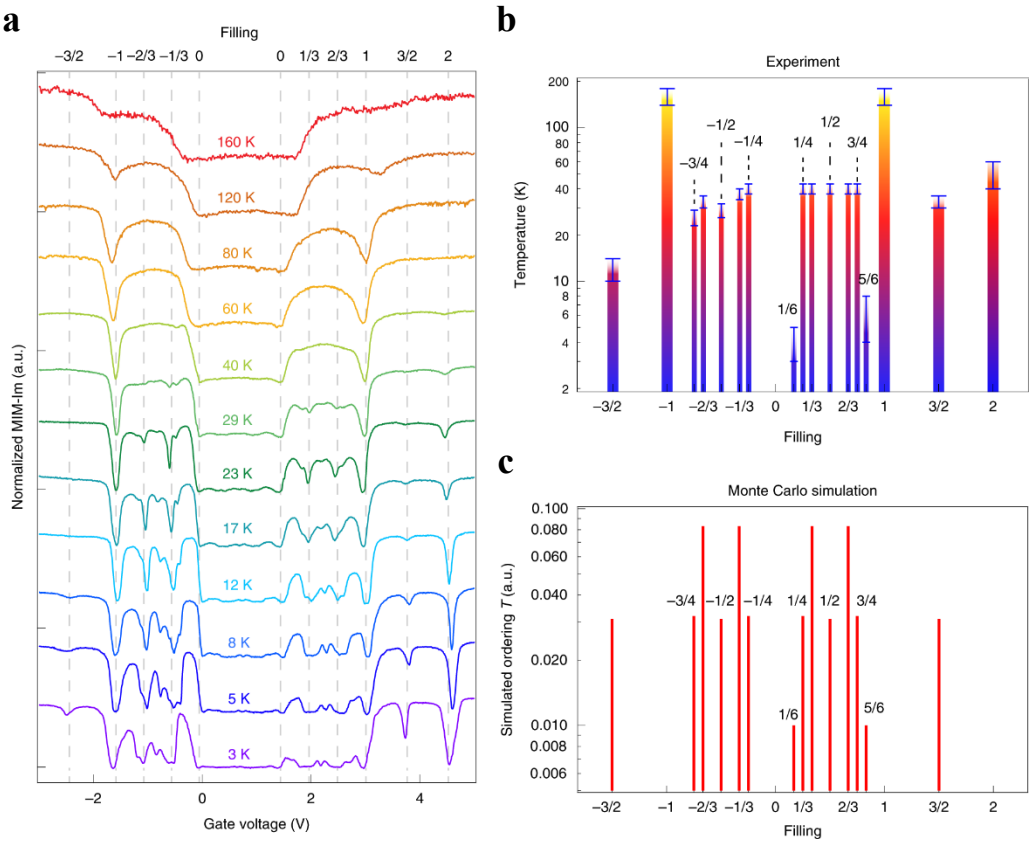

Figure 4.8 Temperature dependence of the correlated insulating states. a, MIM-Im data (***Dev1***) as a function of gate voltage at temperatures from 3 K to 160 K. **b**, Temperature range in which the correlated insulating states can be resolved by MIM. **c**, The melting temperature obtained by MC simulations at various filling fractions corresponding to experimentally observed values. Panel **a-c** adapted from REF 20, copyright Springer Nature.

Corelated insulating states should have thermal activation effect and disappear at relative high temperatures while the intrinsic band edge should not. We repeat the same measurement at temperatures up to 160 K as shown in **Fig**. 4.8a. When the temperature is increasing, there are two gate voltage thresholds ($\sim$0 and + 1.5 V) that do not disappear despite some shift in absolute voltage values (probably due to a remedied contact resistance and a better gating performance). The absence of gate voltage inbetween (from 0 to 1.5 V) could be due to charge carriers doped to in-gap defect states. Thus, we confidently assign the two thresholds as band edges beyond which ($V_g < 0$ V or $V_g > +1.5$ V) holes/electrons start to populate the TMD valance/conduction moire bands. At intermediate temperatures, such as 80 K, the insulating features (dips at -1.6 V and +3 V) are similar on both *e*- and *h*-doped sides. With the knowledge of the used hBN thickness ($\sim$17.4 nm), the corresponding carrier density for these features ($\Delta V_g = 1.5\,V$) are around $1.4 - 1.9 \times 10^{12} cm^{-2}$. This carrier density value corresponds to that of a WS_2/WSe_2 moire superlattice with periodicity of $\sim$8 nm. We assign these states as Mott insulator at half fillings ($\nu = \pm 1$). Meanwhile, we noticed that another group has observed same Mott insulator states in a similar hetero-bilayer [19]. At $V_g = 5$ V, an insulating state with doubled carrier density is observed when temperature is lower than 40 K. This state corresponds to full filling band insulator state of the conduction moiré flat band of the WS_2 layer ($\nu = +2$). Knowing the position of $|\nu| = 1, 2$, we can determine the other insulating dips by assuming a linear relationship between gate voltage and carrier density. For each observed features, the filling value is calculated based on the calibration and converted into the closest simple fraction. In **Fig. 4.7a**, the major dip features in 3 K data can be assigned

to $\nu = \pm\frac{1}{3}, \pm\frac{1}{2}, \pm\frac{2}{3}, \pm 1, \pm\frac{3}{2}$ and $+2$. Some other fine features are observed next to these major dips. To clearly resolve the existence of these additional features, temperature-dependent measurements are carried out and the data are shown in **Fig. 4.7a and 4.7b**. At temperatures from 3 K to 26 K, traces of MIM-Im unambiguously present the additional insulating features and the filling values are assigned as $\nu = \pm\frac{1}{4}, \pm\frac{3}{4}, +\frac{1}{6}$ and $+\frac{5}{6}$. Correlated insulating states at $\nu = \pm\frac{1}{3}, \pm\frac{2}{3}$, similar as in the previous study [18], are generalized Wigner crystal states.

4.3.3 Additional Correlated Insulating States at Fractional Fillings

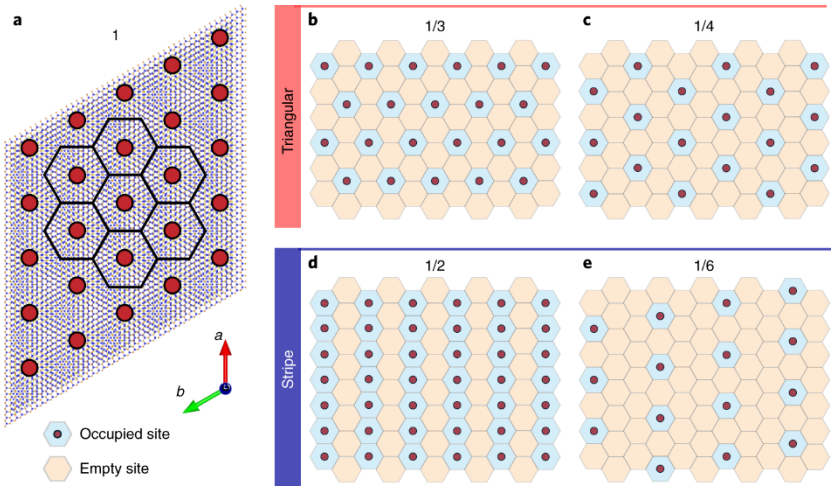

Figure 4.9 Ordering patterns at fractional fillings of the moiré lattice. a, Mott insulator state for the WS_2/WSe_2 moiré superlattice, filled by one carrier per moiré unit cell. **b**, and **c**, Patterns for the triangular lattice formed at fractional fillings of $n = \frac{1}{3}$ and $\frac{1}{4}$, respectively. **d**, and **e**, Patterns for the stripe phase formed at fractional fillings of $n = \frac{1}{2}$ and $\frac{1}{6}$, respectively. Panel **a-d** adapted from REF 20, copyright Springer Nature.

For the Mott insulator state, the whole moiré superlattice is uniformly filled with one carrier per moiré lattice site (shown in **Fig. 4.9a**). For the generalized Wigner states at $\nu = \pm\frac{1}{3}$, the carrier density is only $1/3$ of the Mott state and thus only one carrier fills

every three moiré unit cells (**Fig. 4.9b**). To preserve the rotational symmetry of the original moiré superlattice, charge patterns still form a triangular lattice but with a larger period of $\sqrt{3}\lambda_m$, where λ_m is the periodicity of the moiré superlattice. The $|\nu| = \frac{1}{3}$ states can also be understood by considering a non-negligible nearest-neighboring (NN) interaction between carriers besides the onsite Coulomb repulsion. Thus, charge carriers tend to avoid NN-site occupation. Correspondingly, charge patterns for $|\nu| = \frac{2}{3}$ can be achieved by simply exchanging the occupied and empty sites in $|\nu| = \frac{1}{3}$.

To understand the ordering patterns for all the other fractional fillings, we performed MC simulation on a Coulomb gas model with a triangular lattice at fillings $0 < n \leq 1/2$ (details of the MC simulation can be found in the Methods part of Ref [20]). Considering only the Coulomb interaction (neglect the kinetic energy), the corresponding Hamiltonian is

$$H = \frac{1}{2}\sum_{i,j} V_{ij}(n_i - n)\left(n_j - n\right),$$

where V_{ij} is the Coulomb interaction between electrons at *i*-th and *j*-th moiré sites and $n_i = 0$ or 1 for an occupied or empty *i*-th moiré site. n is the averaged filling factor. A state at filling of $1 - n$ can be obtained by swapping occupied and empty sites, i.e., particle-hole symmetry. In a 2D device with nearby metallic gate, the approximated Coulomb interaction with some screening effect is expressed as

$$V(r) = {}^{1}\!/_{r} - {}^{1}\!/_{\sqrt{r^2 + 4D^2}}$$

Where r: distance between charge carriers; D: distance between gate and charge carriers). Here we consider unscreened Coulomb interaction since D is large with

$$V(r) = {}^{1}/_{r} = {}^{1}/_{|\boldsymbol{R}_i - \boldsymbol{R}_j|}$$

The MC simulations search for filling factors through 0 to ½ to identify any stable charge ordering patterns. Two categories of robust ground-state configurations against perturbation, triangular or stripe phases, are obtained for specific filling fractions. For example, in **Fig. 4.9b and 4.9c**, localized charge carriers form a triangular phase at $n = \frac{1}{3}$ or $\frac{1}{4}$. They match the observed correlated insulating states at $\nu = \pm\frac{1}{3}, \pm\frac{2}{3}, \pm\frac{1}{4}$ and $\pm\frac{3}{4}$. These are considered as generalized Wigner crystal states, resulting from the long-range Coulomb interaction in the moiré superlattice. The rotational symmetry (C_3) is preserved but the translational symmetry is not. In general, the triangular lattice will form if the actual filling satisfies $n = {}^{1}/_{p}$, where p is an integer and $\sqrt{p}\lambda_m$ is the distance between two neighboring sites. This relation holds for $n = {}^{1}/_{3}$ with $\sqrt{3}\lambda_m$ as the 2nd NN-site distance and $n = {}^{1}/_{4}$ with $2\lambda_m$ as the 3rd NN-site distance.

Robust stripe phase ground-state has been observed for $n = \frac{1}{2}$ or $\frac{1}{6}$ and these match the experimental observations at $\nu = \pm\frac{1}{2}, +\frac{1}{6}$ and $+\frac{5}{6}$. Here the C_3 rotational symmetry is further broken in the stripe phase which contains partly filled rows along a same direction as shown in **Fig. 4.9d** and **4.9e**. For the experimentally observed correlated insulating states at $\nu = +\frac{3}{2}$, this state should share a similar charge pattern as $\nu = +\frac{1}{2}$ as can be understood by adding charge carriers on top of a uniformly filled background in the case of ($\nu =$

$+\frac{1}{2}$ plus $\nu = +1$). Here we ignore the specific occupation site within the moiré unit cell (different intra-cell high symmetric stacking site) or a charge-transfer insulator picture [21].

We performed temperature dependence of MIM-Im traces to examine the insulating states. The series of data are shown in **Fig. 4.8a**. The experiment disappearing temperatures of these correlated insulating states (above which the states cannot be resolved) are listed in **Fig. 4.8b**. Above these temperatures, charge carriers can easily hop to nearby empty sites at specific fillings, meaning charge carriers are no longer localized. Mott insulator states ($|\nu| = 1$) persist up to $120 - 160$ K, which corresponds a thermal activation energy of $10 - 20$ meV. Fractional filling states $\nu = \pm\frac{1}{3}, \pm\frac{2}{3}, \pm\frac{1}{2}, \pm\frac{1}{4}, \pm\frac{3}{4}$ and $+\frac{3}{2}$ disappear at $\sim 30 - 40$ K, while $\nu = -\frac{3}{2}$ at ~ 10 K and $\nu = +\frac{1}{6}$ and $+\frac{5}{6}$ at $4 - 6$ K. The experimental characteristic temperatures well match the melting temperatures of these charge ordering patterns from the MC simulation.

4.3.4 Even Stronger and Longer-Range Coulomb Interaction

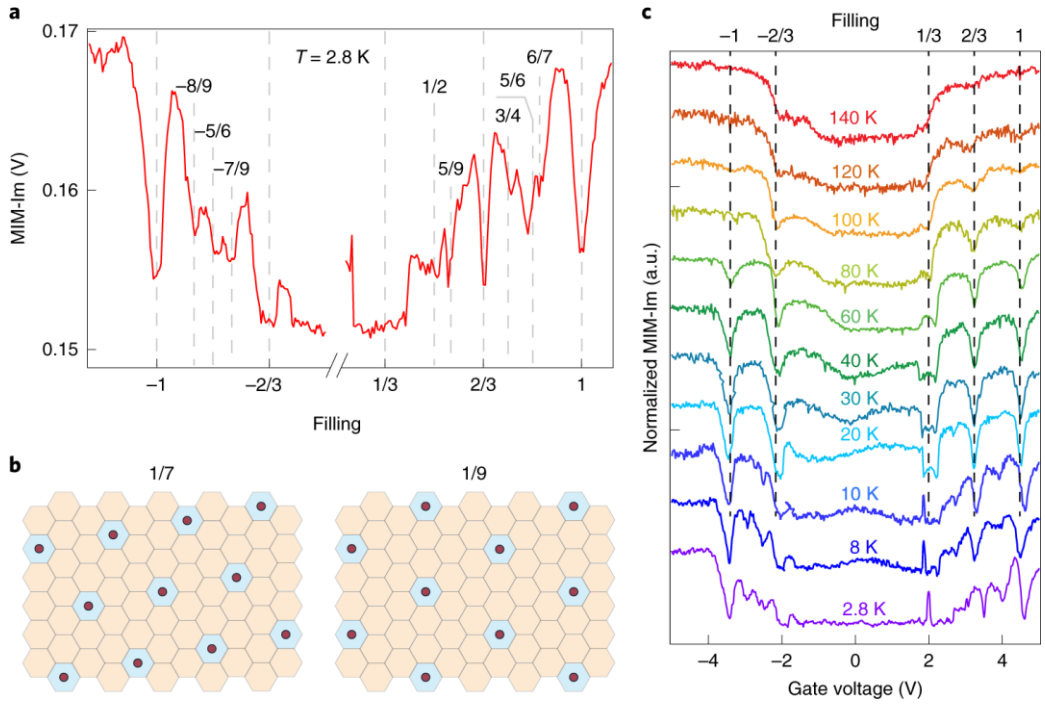

Figure 4.10 Correlated insulating states on device *Dev2*. a, MIM-Im in ***Dev2*** as a function of filling factor at 2.8 K. **b**, Filling pattern obtained by MC simulations for $n = \frac{1}{7}$ and $\frac{1}{9}$. c, Temperature dependence of MIM-Im data from 2.8 K to 140 K. Panel **a-c** adapted from REF 20, copyright Springer Nature.

In device ***Dev2***, an even stronger longer-range interaction has been observed as shown in Fig. 4.10, including new fractional-filling insulating states at $\nu = -\frac{8}{9}, -\frac{5}{6}, -\frac{7}{9}, +\frac{5}{9}$ and $+\frac{6}{7}$. The $\nu = -\frac{5}{6}$ state shares the similar stripe charge order configuration as $\nu = +\frac{5}{6}$ in ***Dev1***. Under particle-hole symmetry, $\nu = -\frac{6}{7}$ or $-\frac{8}{9}$ states are found to have triangular lattice same as $n = \frac{1}{7}$ or $\frac{1}{9}$. Same analysis for $n = \frac{1}{3}$ or $\frac{1}{4}$, $n = \frac{1}{7}$ stands for occupation with separating distance of 4^{th} NN neighbors and $n = \frac{1}{9}$

stands for that of 5th NN neighbors (Fig. 4.10b). The $\nu = +\frac{5}{9}$ and $-\frac{7}{9}$ are exceptions which don't have a well-defined transition to the ground states from our MC simulation.

In addition to these correlated states with longer range interaction, the $\nu = \pm\frac{1}{3}$ and $\pm\frac{2}{3}$ states persist to much higher temperatures ($100 - 120$ K). These enhanced insulating states indicate a much stronger interaction which also corroborates the observation of rich filling fraction states in ***Dev2***. Local strain or inhomogeneities may play a role in the enhancement of electron interaction but future study is required to address this question. Despite the large spatial inhomogeneities, the resolution of ~100 nm of MIM technique allows us to detect local electronic features in strongly correlated systems.

4.3.5 Probing Correlated Insulating States Using Exciton in a Close WSe_2 Sensing Layer by Another Group

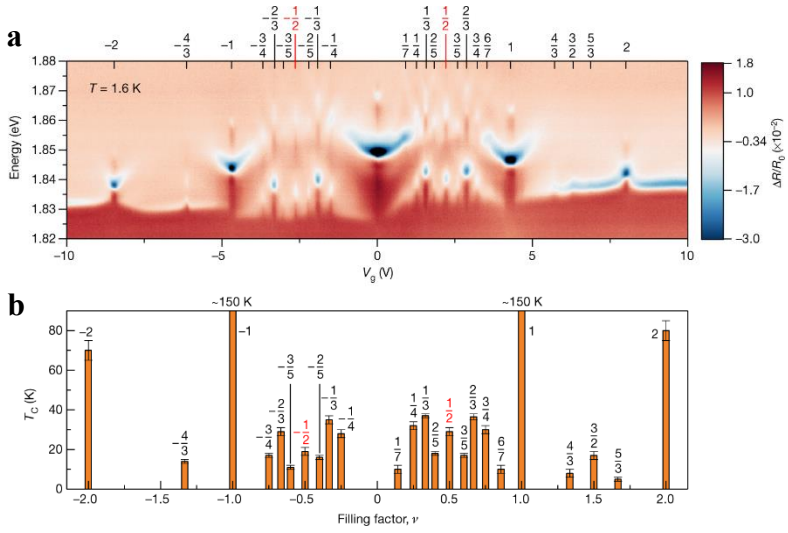

Figure 4.11 Correlated insulating states probed with exciton sensor. **a**, Observation of a series of correlated insulating states at fractional fillings in the WSe_2/WS_2 moire superlattice probed by the reflection contrast spectrum of a WSe_2 layer which is separated by a very thin hBN (~1 nm). **b**. Critical temperatures for the observed insulating states. Panel **a-b** adapted from REF 22, copyright Springer Nature.

Using the extreme sensitivity of A-exciton of WSe_2 layer, researchers have observed these correlated insulating states at fractional fillings in a similar WSe_2/WS_2 moire superlattice [22]. The main result is shown in **Fig. 4.11**. Including our research, the strong correlation effect with the formation of correlated insulating states at rich fractional fillings has been demonstrated in semiconducting TMD moire system.

4.4 Strong Interaction Between Interlayer Excitons Correlated Electrons in WSe_2/WS_2 Moiré Superlattice

The content of this research was published in my co-first authored paper, in which my contribution includes MIM measurements, data analysis and input for manuscript writing.

Miao, S., Wang, T., Huang, X. et al. Strong interaction between interlayer excitons and correlated electrons in WSe2/WS2 moiré superlattice. Nat Commun 12, 3608 (2021).

4.4.1 Interlayer Exciton PL Revealing Correlated Insulating States

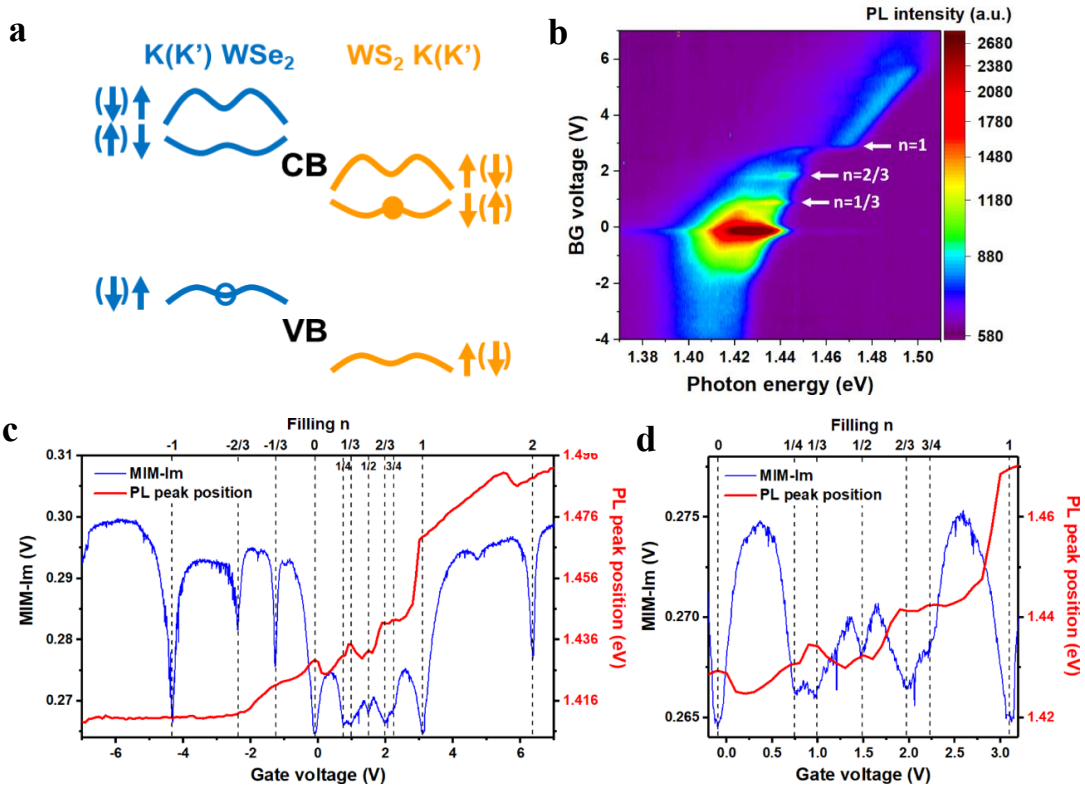

Figure 4.12 Interlayer exciton PL revealing correlated states. a, Type-II band alignment in WSe_2/WS_2 hetero-bilayer with inter-layer excitons at Brillouin zone corner. **b**, Gate-dependent photoluminescence (PL) around 1.4 eV of **D1** at 4.2 K. **c**, Comparison between PL peak position (extracted from **b**) and local conductivity probed by MIM (14 K). **d**, Zoom-in of **c**. Panel **a-d** adapted from REF 30, copyright Springer Nature.

The type-II band alignment in hetero-bilayer TMD moire system allows the formation of interlayer excitons, in which electrons and holes reside on different layers [23–26]. Interlayer excitons are a promising candidate for quantum emitters due to their long lifetime, valley degree of freedom and tunability. Here we further study how these interlayer excitons interact with the correlated electrons in WS_2/WSe_2 hetero-bilayer moire superlattice. The interaction strongly modifies the photoluminescence (PL) of the interlayer excitons. The modulation of exciton PL energy unravels the emergence of correlated insulating states in moire system, such as Mott insulator state ($\nu = 1$), generalized Wigner crystal states ($\nu = \frac{1}{3}, \frac{1}{4}, \frac{2}{3}, \frac{3}{4}$) and a strip phase state ($\nu = \frac{1}{2}$). At the correlated electron states, increasing optical excitation power will brighten up the PL intensity of interlayer exciton, suggesting reduced mobility of the excitons in the moire unit cell. Enhancement of valley polarization of interlayer excitons is also observed at certain filling states.

In angle-aligned WSe2/WS2 hetero-bilayer, the optically excited electrons will reside in WS2 layer with corresponding holes in WSe2 layer as shown in **Fig. 4.12a**. The strong Coulomb interaction enables the formation of interlayer excitons and has been reported [27]. The samples studied here have a same device geometry as shown in **Fig. 4.6b**. On a device **D1**, **Fig. 4.12b** shows the color plot of PL intensity as a function of photon energy and gate voltage at 4.2 K. The emission energy is around 1.4 eV which is much lower than A-exciton energy in isolated individual layer (WS_2:~2.07 eV, WSe_2: ~1.7 eV) [28]. A continuous wave laser (1.959 eV) is used with an excition power of 5 uW. A large blue energy shift (~20 meV) is observed for the PL peak at gate voltage of ~2.9 V.

To examine the fine features, we extracted the PL peak position as a function of gate voltage and compare it with local conductivity measured by MIM-Im on the same device, shown in Fig. 4.11c. In MIM-Im data, a series of insulating states ($\nu = \pm 1, \pm\frac{1}{3}, \pm\frac{2}{3}, \frac{1}{4}, \frac{1}{2}, \frac{3}{4}$ and 2) can be identified as dip features and have been labeled in the figure. Most of these features have some correspondence in the PL peak position curve. The most pronounced correspondences are at fillings of *e*-doping side with a blueshift for the PL peak position. Our result demonstrates that the interlayer exciton PL energy has a sensitivity to the correlated insulating states in the moire system. This can be understood as interlayer exciton has a large spatial extend which renders it a high sensitivity of the dielectric environment (same idea employed in Ref [22,29]). At these correlated insulating states, electrons are localized, and the system opens a gap. The dielectric constant is subsequently modified. This reflects on modification of interlayer exciton in its binding energy, leading to the change in emission energy (blueshift of PL peak position). For Mott insulator state ($\nu = +1$) with a large energy gap compared with other correlated insulating states, the blueshift effect is prominent.

4.4.2 Power-Dependent PL Spectra of Interlayer Exciton

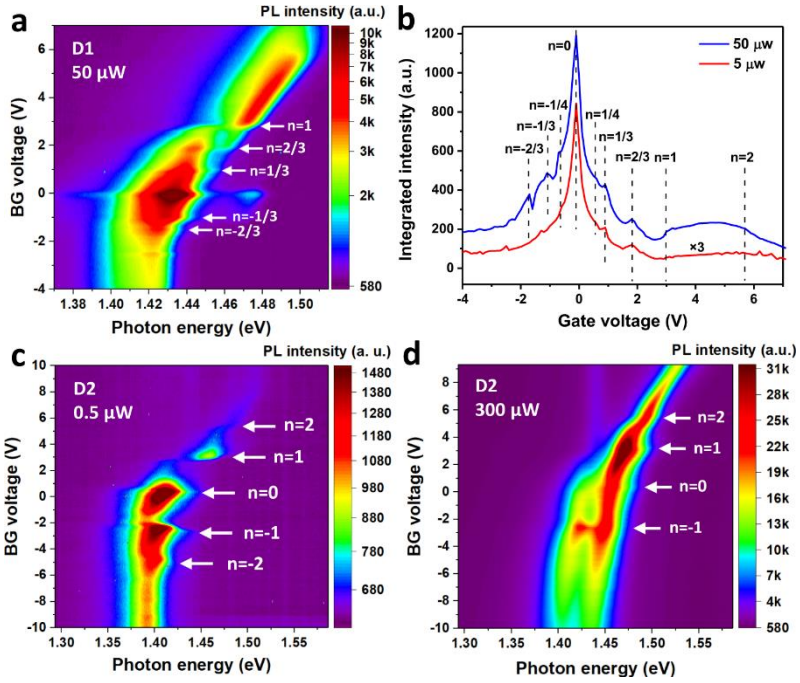

Figure 4.13 PL of interlayer excitons under increased optical excitation power. a, PL spectra of Dev3 at higher optical excitation power (50 uW). **b**, Integrated interlayer exciton PL intensity as a function of gate voltage for **D1** under different excitation power. **c, d** Gate-dependent PL spectra of **D2** under different excitation power. Panel **a-d** adapted from REF 30, copyright Springer Nature.

We further change excitation power by changing the interlayer exciton density. In Fig. 4.13a, a higher excitation power (50 uW) reveals the formation of correlated states at $\nu = -\frac{1}{3}$ and $-\frac{2}{3}$, which are missing in the spectra of 5 uW. Careful analysis of integrated PL intensity further reveals the state at $\nu = -\frac{1}{4}$ as shown in Fig. 4.13b. More drastic power dependence measurements are performed on another device D2 as shown in Fig. 4.13c and 4.13d as the excitation power is changed from 0.5 to 300 uW. Despite the huge increase of exciton density, the Mott states ($\nu = \pm 1$) remain intact which suggests that excitons do not destroy the underlying periodic electron solid. For the spectra map, there

is an asymmetric PL peak shift as a function of the gate voltage for *h*- and *e*-doping sides (prominent shift in e-doping side). This is due to the type-II band alignment and the device structure with WSe_2 layer closer to the back gate. At *h*-doping, holes accumulate the WSe_2 layer, and this significantly screens the electric field between WSe_2 and WS_2 layers. At *e*-doping, electrons accumulate in the WS2 layer and the screening effect from WSe_2 layer is negligible. Therefore, the blueshift effect due to the Stark shift is only pronounced at *e*-doping side. Another noticeable observation is the strongly enhanced PL intensity at $\nu = +1$ under much higher excitation power (comparing **Fig. 4.13c** and **4.13d**). This indicates reduced mobility of interlayer excitons at this state as the measured lifetime changed from 5.1 ns ($\nu = 0$) to 6.5 ns ($\nu = +1$) when electrons are localized at the Mott state (see Supplementary Note 3 of Ref [30]). Interlayer excitons can be polarized by the localized electrons and the attractive force between electrons and polarized excitons could reduce the exciton mobility compared to the charge neutral scenario ($\nu = 0$). With reduced nonradiative recombination, the PL intensity is thus enhanced. Our results raise the question to further study possible localization of interlayer excitons in a periodic electron solid of a moire system.

4.4.3 Enhanced Valley Polarization of Interlayer Exciton at Certain Fillings

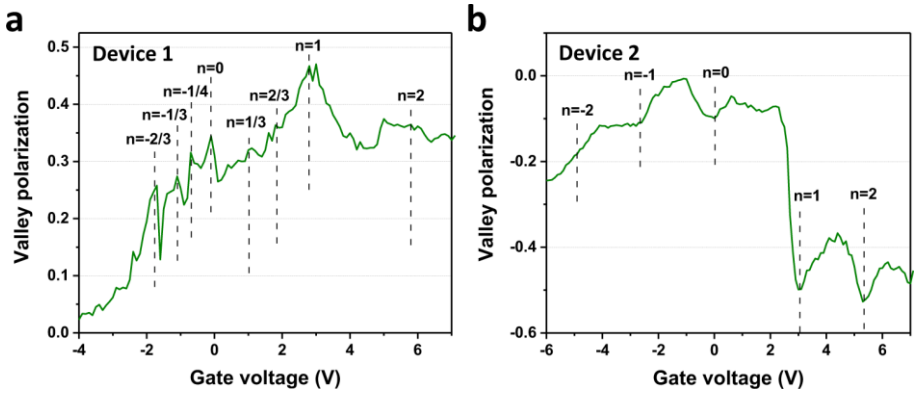

Figure 4.14 Valley polarization of interlayer excitons in the moiré superlattice. a, b Valley polarization of the interlayer excitons in **D1** (0°-twisted) and **D2** (60°-twisted) at 4.2 K. Panel **a-d** adapted from REF 30, copyright Springer Nature.

Helicity-resolved PL spectroscopy measurements provide access to study valley degree of freedom for interlayer excitons. Here we excite the two samples (R stacking, 0° for D1; H stacking, 60° for D2) using right circularly polarized light (σ^+) and detect the interlayer exciton PL of both helicity (σ^+ or σ^-). The valley polarization is calculated by the expression

$$P = {I(\sigma^+) - I(\sigma^-)}\Big/{I(\sigma^+) + I(\sigma^-)},$$

Where $I(\sigma^+)$ and $I(\sigma^-)$ are PL intensity with same and opposite helicity, respectively. The valley polarizations for the two samples are shown in **Fig. 4.14a, b**. The sign of valley polarization is consistent with stacking configuration as interlayer exciton at the atomic registry site of R_h^X (D1) and H_h^h (D2) [31]. In both samples, the correlated insulating states are associated with an enhanced valley polarization. In D2, this effect is most drastic at fillings of $\nu = 1$ and 2. Possible explanation could be due to the attraction between interlayer excitons and the localized correlated electrons. This significantly reduces the

valley depolarization process which requires annihilation of one exciton in one valley and creation of another exciton in the opposite valley. We noticed that similar results have been observed in a research by another group [29].

In summary, the interaction between correlated electrons and interlayer excitons enables the probing of these correlated insulating states in the moire superlattice. Furthermore, it can be utilized to control the mobility and valley polarization of the interlayer excitons.

Additional reference [32].

References

[1] A. L. Elías et al., *Controlled Synthesis and Transfer of Large-Area WS2 Sheets: From Single Layer to Few Layers*, ACS Nano **7**, 5235 (2013).

[2] C. Gong, H. Zhang, W. Wang, L. Colombo, R. M. Wallace, and K. Cho, *Band Alignment of Two-Dimensional Transition Metal Dichalcogenides: Application in Tunnel Field Effect Transistors*, Appl. Phys. Lett. **103**, (2013).

[3] J. Kang, S. Tongay, J. Zhou, J. Li, and J. Wu, *Band Offsets and Heterostructures of Two-Dimensional Semiconductors*, Appl. Phys. Lett. **102**, (2013).

[4] A. Splendiani, L. Sun, Y. Zhang, T. Li, J. Kim, C. Y. Chim, G. Galli, and F. Wang, *Emerging Photoluminescence in Monolayer MoS2*, Nano Lett. **10**, 1271 (2010).

[5] K. F. Mak, C. Lee, J. Hone, J. Shan, and T. F. Heinz, *Atomically Thin MoS2: A New Direct-Gap Semiconductor*, Phys. Rev. Lett. **105**, 2 (2010).

[6] E. C. Regan, J. Zhu, A. H. Macdonald, H. Deng, and F. Wang, *Emerging Exciton Physics in Transition Metal Dichalcogenide Heterobilayers*, Nat. Rev. Mater. **0123456789**, (2022).

[7] K. Kim et al., *Van Der Waals Heterostructures with High Accuracy Rotational Alignment*, Nano Lett. **16**, 1989 (2016).

[8] D. Edelberg et al., *Approaching the Intrinsic Limit in Transition Metal Diselenides via Point Defect Control*, Nano Lett. **19**, 4371 (2019).

[9] F. Wu, T. Lovorn, E. Tutuc, and A. H. Macdonald, *Hubbard Model Physics in Transition Metal Dichalcogenide Moiré Bands*, Phys. Rev. Lett. **121**, 26402 (2018).

[10] M. H. Naik and M. Jain, *Ultraflatbands and Shear Solitons in Moiré Patterns of Twisted Bilayer Transition Metal Dichalcogenides*, Phys. Rev. Lett. **121**, 266401 (2018).

[11] S. Shabani, D. Halbertal, W. Wu, M. Chen, S. Liu, J. Hone, W. Yao, D. N. Basov, X. Zhu, and A. N. Pasupathy, *Deep Moiré Potentials in Twisted Transition Metal Dichalcogenide Bilayers*, Nat. Phys. **17**, 720 (2021).

[12] Z. Zhang, Y. Wang, K. Watanabe, T. Taniguchi, K. Ueno, E. Tutuc, and B. J. LeRoy, *Flat Bands in Twisted Bilayer Transition Metal Dichalcogenides*, Nat. Phys. **16**, 1093 (2020).

[13] A. Weston et al., *Atomic Reconstruction in Twisted Bilayers of Transition Metal*

Dichalcogenides, Nat. Nanotechnol. **15**, 592 (2020).

[14] M. R. Rosenberger, H. J. Chuang, M. Phillips, V. P. Oleshko, K. M. McCreary, S. V. Sivaram, C. S. Hellberg, and B. T. Jonker, *Twist Angle-Dependent Atomic Reconstruction and Moiré Patterns in Transition Metal Dichalcogenide Heterostructures*, ACS Nano **14**, 4550 (2020).

[15] L. J. McGilly et al., *Visualization of Moiré Superlattices*, Nat. Nanotechnol. **15**, 580 (2020).

[16] Y. Tang et al., *Simulation of Hubbard Model Physics in WSe2/WS2 Moiré Superlattices*, Nature **579**, 353 (2020).

[17] L. Wang et al., *Correlated Electronic Phases in Twisted Bilayer Transition Metal Dichalcogenides*, Nat. Mater. **19**, 861 (2020).

[18] E. C. Regan et al., *Mott and Generalized Wigner Crystal States in WSe2/WS2 Moiré Superlattices*, Nature **579**, 359 (2020).

[19] Z. Chu et al., *Nanoscale Conductivity Imaging of Correlated Electronic States in WSe2/WS2 Moiré Superlattices*, Phys. Rev. Lett. **125**, 186803 (2020).

[20] X. Huang et al., *Correlated Insulating States at Fractional Fillings of the WS2/WSe2 Moiré Lattice*, Nat. Phys. **17**, 715 (2021).

[21] Y. Zhang, N. F. Q. Yuan, and L. Fu, *Moiré Quantum Chemistry: Charge Transfer in Transition Metal Dichalcogenide Superlattices*, Phys. Rev. B **102**, 1 (2020).

[22] Y. Xu, S. Liu, D. A. Rhodes, K. Watanabe, T. Taniguchi, J. Hone, V. Elser, K. F. Mak, and J. Shan, *Correlated Insulating States at Fractional Fillings of Moiré Superlattices*, Nature **587**, 214 (2020).

[23] T. Wang et al., *Giant Valley-Zeeman Splitting from Spin-Singlet and Spin-Triplet Interlayer Excitons in WSe2/MoSe2 Heterostructure*, Nano Lett. **20**, 694 (2020).

[24] K. Tran et al., *Evidence for Moiré Excitons in van Der Waals Heterostructures*, Nature **567**, 71 (2019).

[25] K. L. Seyler, P. Rivera, H. Yu, N. P. Wilson, E. L. Ray, D. G. Mandrus, J. Yan, W. Yao, and X. Xu, *Signatures of Moiré-Trapped Valley Excitons in MoSe2/WSe2 Heterobilayers*, Nature **567**, 66 (2019).

[26] P. Rivera et al., *Observation of Long-Lived Interlayer Excitons in Monolayer MoSe 2-WSe 2 Heterostructures*, Nat. Commun. **6**, 4 (2015).

[27] C. Jin et al., *Observation of Moiré Excitons in WSe2/WS2 Heterostructure*

Superlattices, Nature **567**, 76 (2019).

[28] W. Zhao, Z. Ghorannevis, L. Chu, M. Toh, C. Kloc, P.-H. Tan, and G. Eda, *Evolution of Electronic Structure in Atomically Thin Sheets of WS 2 and WSe 2*, ACS Nano **7**, 791 (2013).

[29] E. Liu, T. Taniguchi, K. Watanabe, N. M. Gabor, Y. T. Cui, and C. H. Lui, *Excitonic and Valley-Polarization Signatures of Fractional Correlated Electronic Phases in a WSe2/WS2 Moiré Superlattice*, Phys. Rev. Lett. **127**, 37402 (2021).

[30] S. Miao et al., *Strong Interaction between Interlayer Excitons and Correlated Electrons in WSe2/WS2 Moiré Superlattice*, Nat. Commun. **12**, 8 (2021).

[31] H. Yu, G. Bin Liu, and W. Yao, *Brightened Spin-Triplet Interlayer Excitons and Optical Selection Rules in van Der Waals Heterobilayers*, 2D Mater. **5**, (2018).

[32] Y. Li, K. A. N. Duerloo, K. Wauson, and E. J. Reed, *Structural Semiconductor-to-Semimetal Phase Transition in Two-Dimensional Materials Induced by Electrostatic Gating*, Nat. Commun. **7**, 1 (2016).

Chapter 5 Tuning Moiré Excitons and Correlated Electronic States through Layer Degree of Freedom

Moiré coupling in transition metal dichalcogenides (TMD) superlattices introduces flat minibands with strong electronic correlation and emergent correlated states. It also modifies the strong Coulomb-interaction-driven excitons and gives rise to moiré excitons. Here, through the layer degree of freedom to the WSe_2/WS_2 moiré superlattice by changing WSe_2 from monolayer to bilayer and trilayer, we observe systematic changes of optical spectra of the moiré excitons, which directly confirm the highly interfacial nature of moiré coupling at the WSe_2/WS_2 interface. The additional WSe_2 layers also modulate the strong electronic correlation strength, evidenced by the reduced Mott transition temperature with added WSe_2 layer(s). Our study presents a new method to tune the strong electronic correlation and moiré exciton bands in the TMD moiré superlattices, ushering in an exciting platform to engineer quantum phenomena stemming from strong correlation and Coulomb interaction.

The content of this research was adopted from my co-first authored paper, in which my contribution includes MIM measurements, data analysis and input for manuscript writing.

Dongxue Chen[#], Zhen Lian[#], Xiong Huang[#], Ying Su[#] et al. Tuning Moiré Excitons and Correlated Electronic States through Layer Degree of Freedom, *under view*

In semiconducting TMD moire system, the combination of large effective mass and strong moiré coupling renders the easier formation of flat bands and

stronger electronic correlation. This has been demonstrated with Mott insulating states in WSe_2/WS_2 moire superlattice at half filling with transition temperatures exceeding 150 K and correlated insulating states at fractional fillings [1–3]. Furthermore, it would be of great interest to tune the correlation strength in this TMD moire system. Recently [4,5], out-of-plane electric displacement field has been used to tune the moire band width hence the correlation strength in twisted homobilayer WSe_2 [4] or o°-aligned $MoTe_2/WSe_2$ heterobilayer [5]. Here, we approach the tuning of electronic correlation through the layer degree of freedom, by increasing the layer number of WSe_2 in aligned WSe_2/WS_2 heterostructure.

5.1 Determination of Layer Number by Optical Reflectance

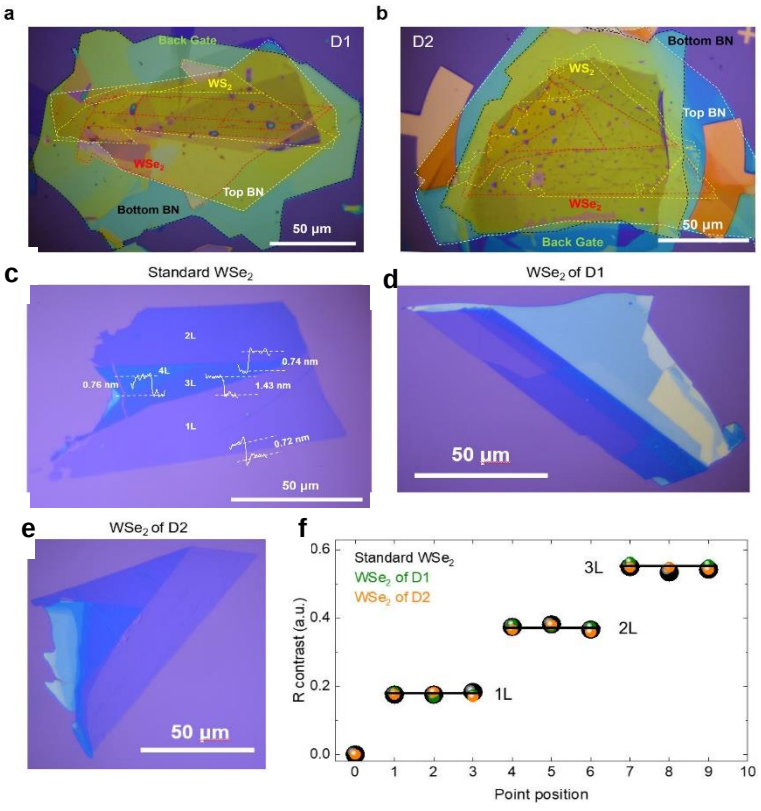

Figure 5.1 WSe_2 layer number determination. **a** and **b** Optical images of a back-gate WSe_2/WS_2 devices, D1 and D2 respectively. **c-e** Optical images of WSe_2-only layers and the reflectance contrast **f**. Additionally, layer thickness has been studied by AFM as plot in **c**.

The back-gated angle-aligned WSe_2/WS_2 heterojunction devices are shown in **Fig. 5.1a-b** using same fabrication technique as described in previous chapter. The device structure is explained in **Fig. 5.2a**. Three different regions: 1L/1L, 2L/1L, and 3L/1L WSe_2/WS_2, can be resolved in the same device. The three regions are expected to have a same twisted angle since WSe_2 layers are from the same flake.

The optical reflectance from a thin flake of 2D materials is related to its absorption [6,7] and thus provides a powerful method to determine the thickness of the 2D materials such as WSe_2. The microscope images of three WSe_2 flakes (including a standard WSe_2 flake, device D1, and device D2) are shown in **Fig. 5.1c-e**. Optical contrast analysis method is applied to realize thickness identification by numerically analyzing the RGB optical images of the samples. The reflectance contrast (R contrast, defined as $(R_{substrate} - R_{sample})/R_{substrate}$) for these three pieces of WSe_2 flakes is also calculated (the red channel), and the values for different layer regions are plotted in **Fig. 5.1f**. It is evident that WSe_2 regions with a certain layer number share similar R contrast, while the increase of one additional layer will increase the R contrast by one "step". Thus, by comparing with the R contrasts of standard WSe_2 flake and the WSe_2 flakes used in D1 and D2, we can accurately confirm the number of layers of WSe_2. The layer thickness is further confirmed through AFM[23] measurements (**Fig. 5.1c**). For the standard WSe_2 sample, we overlayer the AFM topography measurements with the microscope image. It is evident that each layer adds to about 0.74 ± 0.03 nm in height, consistent with previous reports [8].

[23] Atomic force microscopy.

5.2 Interfacial Moiré Potential Revealed by Optical Reflectance Measurements

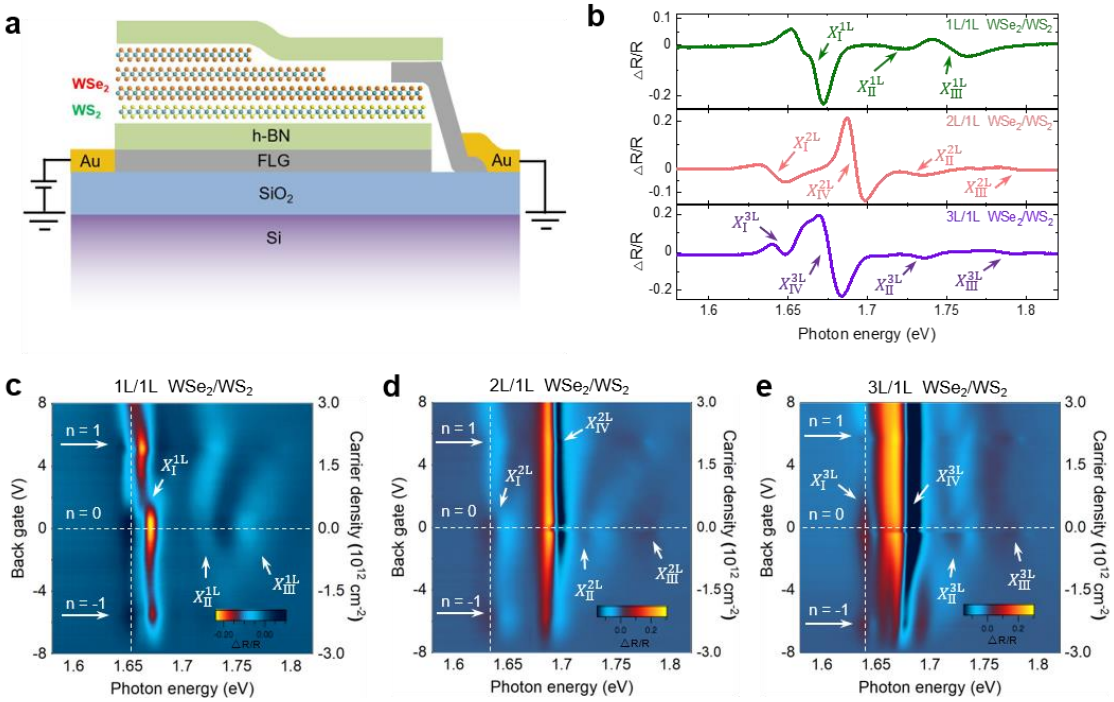

Figure 5.2 Angle-aligned multilayer WSe_2/monolayer WS_2 moiré superlattice. a, Schematic of the multilayer WSe_2/monolayer WS_2 heterojunction devices, encapsulated with BN on both sides with few-layer graphene as back gate electrode. **b**, Differential reflectance spectra of different regions at zero gate voltage. **c-e**, are the differential reflectance spectra as a function of the gate voltage (density of carriers) at the region of 1L/1L, 2L/1L, and 3L/1L WSe_2/WS_2. All data were taken at 4.5 K.

The 1L/1L WSe_2/WS_2 heterojunction has a type-II band alignment, with the conduction band minimum (CBM) located in the WS_2 layer and the valance band maximum (VBM) in the WSe_2 layer. Strong moiré coupling leads to a band folding in the mini-Brillouin zone and generates moiré exciton bands, which will split the A exciton resonance of WSe_2 into three moiré exciton peaks, as demonstrated in the previous experiments [9,10]. Here the reflectance spectra in the three different regions of the WSe_2/WS_2 multilayer heterojunction as a function of the gate voltage are shown in Fig.5.2c-e. There are two major differences between the moiré exciton spectra from the

1L/1L WSe_2/WS_2 and multilayer WSe_2/monolayer WS_2 (2L/1L or 3L/1L) heterojunction. First, it is evident that near the charge-neutral region (gate voltage ~ 0 V), there are three moiré exciton resonances in the 1L/1L WSe_2/WS_2 region (**Fig. 5.2c**) but four in other regions (2L/1L and 3L/1L). Second, the moiré exciton energy difference between the lowest and highest energy moiré excitons increases significantly in both 2L/1L (**Fig. 5.2d**) and 3L/1L (**Fig. 5.2e**) WSe_2/WS_2 regions. These observations are better illustrated in **Fig. 5.2b**, which plots the differential reflectance spectra at the gate voltage of 0 V for the three different regions (line cuts at zero gate voltage in **Fig. 5.2c-e**. The observed moiré exciton peaks are listed in the **Table 5.1** below for three regions:

WSe_2/WS_2	X_{IV}	X_I	X_{II}	X_{III}
1L/1L	--	1.662	1.715	1.753
2L/1L	1.693	1.642	1.728	1.793
3L/1L	1.677	1.645	1.730	1.785

Table 5.1 Moiré exciton peaks energy (eV) for three regions.

The largest moiré exciton energy difference, defined as the energy difference between X_{III} and X_I, is ~ 90 meV for the 1L/1L region but ~ 150 meV for 1L/2L region and ~140 meV for 1L/3L region, an increase of more than 50%.

The above observations suggest that the moiré potential is highly localized at the WSe_2/WS_2 interface and has a limited extension along the out-of-plane direction. As a result, the moiré coupling only significantly modifies the first WSe_2 layer in contact with the monolayer WS_2. The newly developed exciton resonances in the 2L/1L and 3L/1L WSe_2/WS_2 heterojunctions (X_{IV}^{2L} and X_{IV}^{3L}), therefore, arise from the barely modified intralayer A exciton in the additional WSe_2 layers away from the interface. This is

supported by the fact that the energies of X_{IV}^{2L} (1.693 eV) and X_{IV}^{3L} (1.677 eV) are close to the intralayer A exciton energy of monolayer WSe_2 (~1.70 eV), and it is further corroborated by the stronger reflectance intensity from the new moiré exciton in 3L/1L WSe_2/WS_2 (X_{IV}^{3L}) compared with that in 2L/1L WSe_2/WS_2 (X_{IV}^{2L}). Moreover, there is a redshift in the moiré exciton resonance X_I and blueshifts in X_{II} and X_{III} in both 2L/1L and 3L/1L WSe_2/WS_2 compared with those in 1L/1L WSe_2/WS_2 (Fig. 1b). And the shift of X_{II} and X_{III} is more significant in magnitude than that of X_I.

5.3 Theoretical Simulation of Moiré Excitons for Different Regions

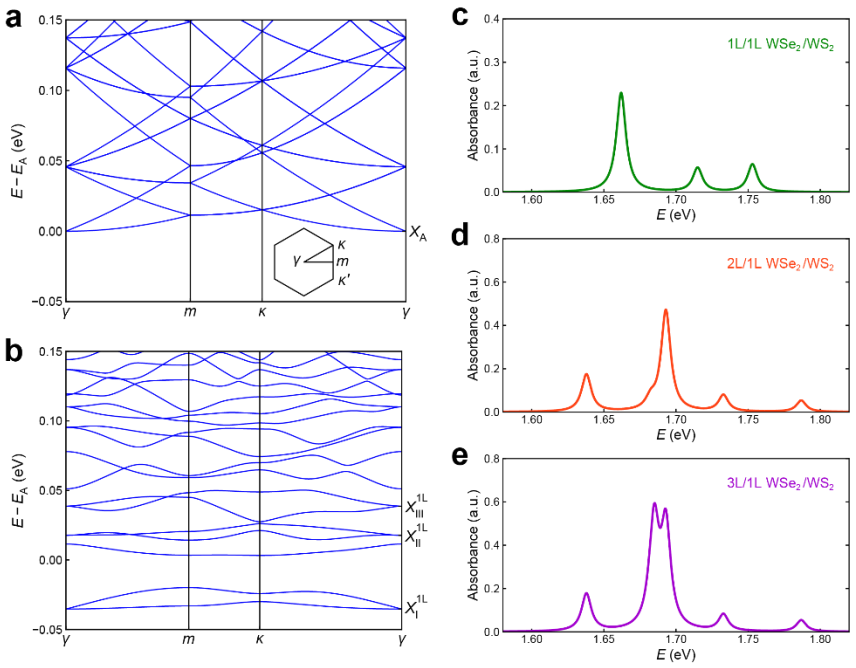

Figure 5.3 Theoretical simulation of moiré excitons. a and **b** are the energy bands of bare intralayer A excitons in 1L WSe_2 and moiré excitons in 1L/1L WSe_2/WS_2, respectively. In (a), the A exciton bands are folded into the mini Brillouin zone of the moiré superlattice for discussion. Inset of (a) shows the schematic of the mini Brillouin zone with high symmetry points. The WSe_2 bright intralayer A exciton state is marked by X_A in (a). (b) The three bright moiré exciton states (X_I^{1L}, X_{II}^{1L}, and X_{III}^{1L}). Here we set the energy E_A of X_A as the energy reference. **c-e** Optical absorption spectra in 1L/1L, 2L/1L, and 3L/1L WSe_2/WS_2 with interlayer hybridization between moiré exciton and intralayer A exciton considered in (d) and (e).

A phenomenological model can be used to understand the results, considering the moiré excitons in the first WSe_2 layer interacting with a exciton state in the added WSe_2 layer(s) that has the resonance energy between X_I and X_{II}. The resulting level repulsion naturally explains the red shift of X_I and blue shift of X_{II} and X_{III} in the 2L/1L (3L/1L) compared with 1L/1L WSe_2/WS_2. To understand the phenomenological model, we propose a possible microscopic mechanism by considering the hybridization between moiré excitons and interlayer-like hybrid exciton (iX) in multilayer WSe_2/1L WS_2. The

hybridization can increase the energy separation between moiré excitons and is enabled by the moiré-potential-induced Umklapp scattering. The interlayer-like hybrid exciton arises from the interlayer tunneling in multilayer WSe_2 that hybridizes the valence bands in different layers [11]. However, it has much weaker oscillator strength than the intralayer-like hybrid exciton and cannot be resolved in the experiment. In the absence of hybridization between different excitonic states, the energy dispersion of bare intralayer A excitons in 1L WSe_2 and moiré excitons in 1L/1L WSe_2/WS_2 are shown in **Fig. 5.3a** and **b**, respectively. Here we fold the energy bands of A excitons into the mini-Brillouin zone to compare directly with that of moiré excitons. The bright A exciton state at the mini Brillouin zone center (denoted as γ point in the inset of **Fig. 5.3a**) is marked as X_A in **Fig. 5.3a**, and the bright moiré exciton states are marked as $X_{\mathrm{I}}^{1\mathrm{L}}$, $X_{\mathrm{II}}^{1\mathrm{L}}$, and $X_{\mathrm{III}}^{1\mathrm{L}}$ in **Fig. 5.3b**. The optical absorption spectrum of moiré excitons in 1L/1L WSe_2/WS_2 is shown in **Fig. 5.3c**, with the three resonances corresponding to the three bright moiré exciton states. For the absorption spectrum of 2L/1L WSe_2/Ws_2 in **Fig. 5.3d**, we introduce the hybridization between moiré excitons and interlayer-like hybrid excitons. The hybridization induces a redshift in $X_{\mathrm{I}}^{2\mathrm{L}}$ and blueshifts in $X_{\mathrm{II}}^{2\mathrm{L}}$ and $X_{\mathrm{III}}^{2\mathrm{L}}$ compared with those of 1L/1L WSe_2/WS_2 in **Fig. 5.3c**. The larger shift in the magnitude of $X_{\mathrm{II}}^{2\mathrm{L}}$ and $X_{\mathrm{III}}^{2\mathrm{L}}$ indicates stronger hybridization with the interlayer-like hybrid exciton, which is consistent with the proposed mechanism. Moreover, the intralayer-like hybrid exciton in the second WSe_2 layer leads to another resonance $X_{IV}^{2\mathrm{L}}$ between $X_I^{2\mathrm{L}}$ and $X_{II}^{2\mathrm{L}}$, as shown in **Fig. 5.3d**, which is consistent with our experimental observation (**Fig. 5.2b, d**). In 3L/1L WSe_2/WS_2, additional hybrid excitons can be induced by the interlayer tunneling between valence bands in the 2nd and 3rd WSe_2

layers. In this case, the additional hybrid excitons away from the WSe_2/WS_2 interface do not affect the moiré excitons. Therefore, the moiré excitons in 3L/1L WSe_2/WS_2 are nearly identical to those in 2L/1L WSe_2/WS_2 (**Fig. 5.3d**), also consistent with our experimental results (**Fig. 5.2b**). On the other hand, the additional hybrid excitons from upper WSe_2 layers will contribute to the resonant peak $X_{\mathrm{IV}}^{3\mathrm{L}}$ which should be consisted of two sub-resonances. This is also consistent with our experimental data, as $X_{IV}^{3\mathrm{L}}$ (**Fig. 5.2e**) is broader than $X_{IV}^{2\mathrm{L}}$ (**Fig. 5.2d**). Interestingly, although these two resonances in $X_{IV}^{3\mathrm{L}}$ cannot be resolved at the charge-neutral region, likely due to linewidth broadening, they can be revealed in the p-doping region (**Fig. 5.2e**). Further study is required.

5.4 Electronic Band Structure for WSe_2/WS_2 Moiré Superlattices with Different WSe_2 Layer Numbers

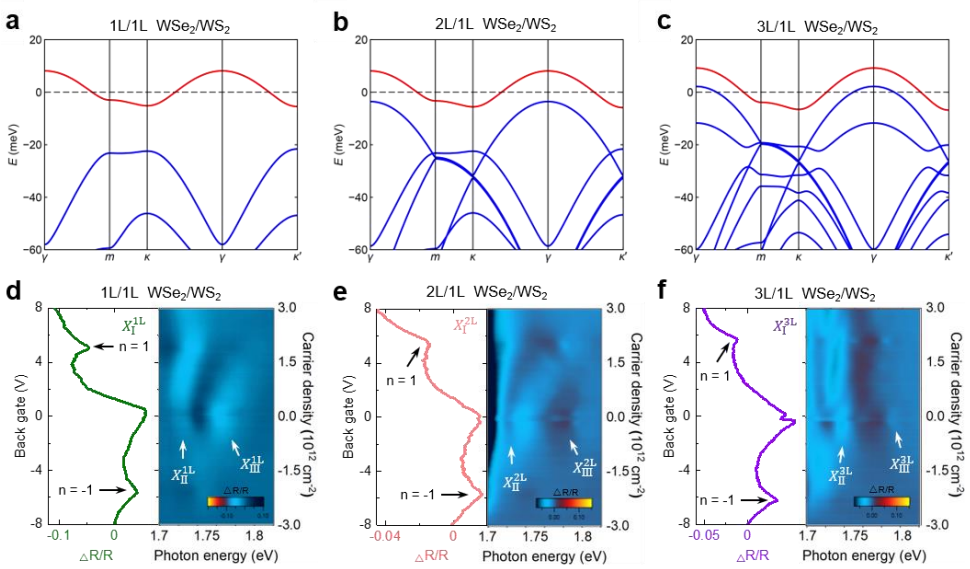

Figure 5.4 Layer dependence of the electronic flat miniband for WSe_2/WS_2 moiré superlattices. a-c are calculated electronic band structure of the valence bands in 1L/1L, 2L/1L and 3L/1L WSe_2/WS_2, respectively, with the moiré flat band from the 1st layer WSe_2 labelled in red. **d-f** are differential reflectance intensity of the moiré exciton (X_I) as a function of the back gate voltage (carrier density) in Fig. 5.2c-e, respectively (vertical dashed line cuts), with the inset showing the enhanced reflectance spectra near the moiré excitons X_{II} and X_{III}.

The moiré excitons in the three regions show distinct gate dependence, which also confirms the interfacial nature of the moiré coupling in the WSe_2/WS_2 superlattice. Our theoretical model, which considers the interfacial nature of the moiré coupling, shows that the valence bands due to the added layers are higher in energy than the moiré electronic flatband from the WSe_2/WS_2 interface, as shown in Fig. 5.4a-c. When carriers are added to the 1L/1L WSe_2/WS_2 heterostructure, they will fill the first moiré valence band in the WSe_2 layer and the first moiré conduction band in the WS_2 layer. The first flat moiré miniband has a strong electron correlation due to their narrow bandwidth, such as the formation of Mott insulator states at the half-fillings [1–3,10,12,13]. The optical

reflectance spectra are expected to be modulated by these correlated states. In the 1L/1L WSe_2/WS_2 region, all three excitons are modulated, with X_I^{1L} being the most obvious one (**Fig. 5.2c**). In the 2L/1L and 3L/1L WSe_2/WS_2 regions, the excitons at the lowest energy (X_I^{2L} and X_I^{3L}) are also strongly modulated (**Fig. 5.2d and e**). **Fig. 5.4d-f** plot the gate voltage dependence of the lowest energy moiré exciton for the three different regions (X_I^{1L}, X_I^{2L} and X_I^{3L}), which clearly shows intensity modulations at $|n| = 1$[24]. On the other hand, the additional excitons in 2L/1L (X_{IV}^{2L}) and 3L/1L (X_{IV}^{3L}) WSe_2/WS_2 regions are barely affected by the formation of the Mott states at $|n| = 1$ (**Fig. 5.2d and e**). These behaviors can also be explained by the interfacial nature of the moiré coupling, which confines the correlated electrons at the interface of WSe_2/WS_2. The modulation of the moiré excitons at the $|n| = 1$ is likely due to the dielectric constant change and gap opening associated with the Mott insulator states. Due to the small radius of the strongly bound exciton [14], only the moiré excitons in the first WSe_2 layer immediately interfacing with the WS_2 monolayer can sensitively detect the dielectric constant change at the interface. In the 2L/1L and 3L/1L regions, the additional excitons originated from intralayer excitons localized in the added layers, are thus barely affected.

[24] Total degeneracy is 2.

5.5 Tunable Electronic Correlation Revealed by MIM

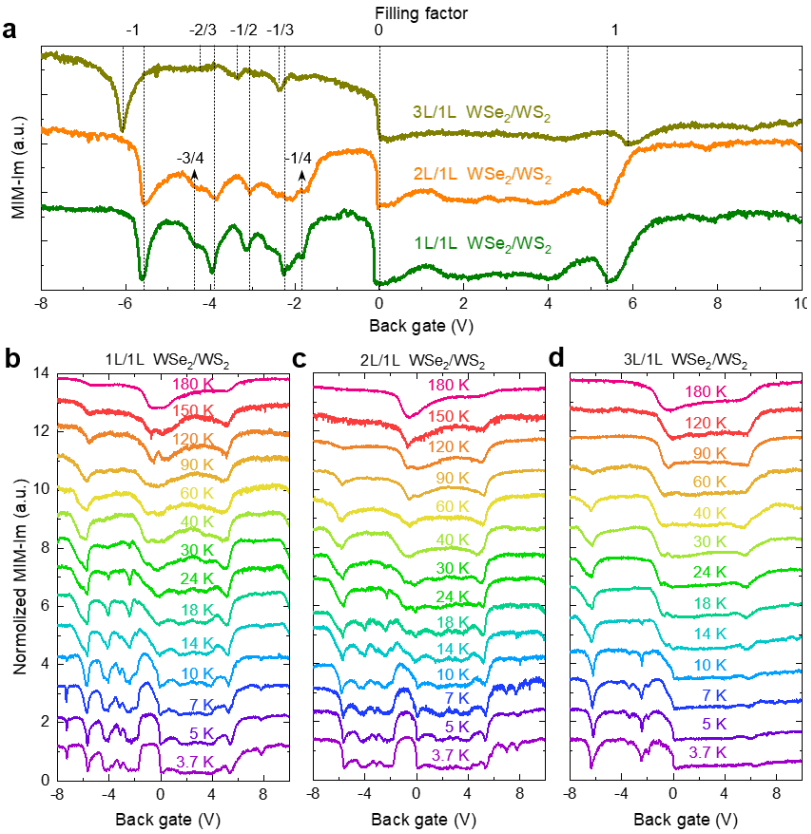

Figure 5.5 MIM measurements of correlated states in different moiré superlattices. a, MIM spectra as a function of gate voltage for the moiré superlattice of 1L/1L WSe_2/WS_2 (green), 2L/1L WSe_2/WS_2 (orange), and 3L/1L WSe_2/WS_2 (brown) at 10 K. **b-d** are the temperature dependent MIM spectra for the moiré superlattice of 1L/1L, 2L/1L, and 3L/1L WSe_2/WS_2, respectively.

To better investigate the tuning of the electron correlation by the layer degree of freedom, we perform MIM measurements to study the correlated insulating states in the three different heterostructure regions (Fig. 5.5a). In the multilayer WSe_2/1L WS_2 device, we primarily focus on the features on the hole-doping side, as the holes reside in the WSe_2 layer due to the type II alignment, and we introduce the layer degree of freedom by modulating the layer number of WSe_2. At temperature $T = 10\ K$, the MIM spectra in both 1L/1L and 2L/1L WSe_2/WS_2 regions show similar pronounced features at various fillings, including the Mott insulator states at $n = -1$, the generalized Wigner crystal states at fractional fillings of $n = -\frac{1}{3}, -\frac{2}{3}, -\frac{1}{2}, -\frac{1}{4}$ & $-\frac{3}{4}$, etc. The 3L/1L WSe_2/WS_2 data show fewer and less pronounced dips: other than the Mott insulator state at $n = -1$, only two fractional fillings $n = -\frac{1}{3}$ and $-\frac{1}{2}$ can be resolved. There is also a small difference in the twist angle in the 3L/1L WSe_2/WS_2 region (~1.3°) compared to that in the 1L/1L and 2L/1L

regions (~0.9°), which results in slightly different gate voltage positions for these insulating states in the 3L/1L WSe_2/WS_2 region[25]. Since the formation of the correlated insulating states at fractional fillings depends on long-range Coulomb interaction among electrons in neighboring moiré unit cells, our results suggest that the inter-site electron interaction strength is weaker in 3L/1L than in 1L/1L or 2L/1L WSe_2/WS_2. The difference in the on-site interaction, corresponding to the Mott insulator state at $n = -1$, can be further revealed in its temperature dependence. As shown in **Fig. 5.5b-d**, as the temperature is raised, the features at fractional fillings disappear at ~30 K in both 1L/1L and 2L/1L WSe_2/WS_2 regions and at ~15 K in the 3L/1L WSe_2/WS_2 region. The Mott insulator state at n=-1 survives at much higher temperatures in 1L/1L WSe_2/WS_2, persisting to above 180 K, the highest Mott transition temperature reported in all 2D moiré superlattice structures so far. In the 2L/1L WSe_2/WS_2 region, the Mott transition temperature is ~120 K, while it is much lower, ~60 K, in the 3L/1L region. As the correlation strength is determined by the ratio of the Coulomb interaction to the kinetic energy, the reduction of electron correlation strength from 1L/1L or 2L/1L WSe_2/WS_2 is likely due to the increased dielectric screening from the added WSe_2, which reduces the Coulomb interaction at the interface. However, the further reduced correlation strength in the 3L/1L WSe_2/WS_2 is facilitated by the additional increase of kinetic energy, which arises from the increased bandwidth of the flat band. We emphasize here that even the reduced electron correlation in the 2L/1L and 3L/1L WSe_2/WS_2 is still significantly stronger than that in graphene moiré systems, with the Mott transition temperature around 4 K. As a result, the layer degree of freedom can be utilized for engineering new correlated states.

5.6 Conclusion

In summary, we have demonstrated a new moiré superlattice system based on multilayer TMD heterojunctions. The added layers host additional intralayer excitons that interact with the moiré excitons residing at the moiré interface, and they can further modify the correlation strength of the correlated states. Considering the layer-valley-spin locking in TMD [15], this new TMDs moiré superlattices provide an exciting platform to

[25]Bottom BN has a thickness ~52 nm with dielectric constant chosen to be 3.5.

investigate emerging correlated valley and spin physics. In the next chapter, we will discuss the formation of an emergent quantum phase, excitonic insulator, in 1L/2L WS_2/WSe_2 moiré superlattice.

References

[1] Y. Xu, S. Liu, D. A. Rhodes, K. Watanabe, T. Taniguchi, J. Hone, V. Elser, K. F. Mak, and J. Shan, *Correlated Insulating States at Fractional Fillings of Moiré Superlattices*, Nature **587**, 214 (2020).

[2] E. C. Regan et al., *Mott and Generalized Wigner Crystal States in WSe2/WS2 Moiré Superlattices*, Nature **579**, 359 (2020).

[3] X. Huang et al., *Correlated Insulating States at Fractional Fillings of the WS2/WSe2 Moiré Lattice*, Nat. Phys. **17**, 715 (2021).

[4] A. Ghiotto et al., *Quantum Criticality in Twisted Transition Metal Dichalcogenides*, Nature **597**, 345 (2021).

[5] T. Li et al., *Continuous Mott Transition in Semiconductor Moir\'e Superlattices*, Nature **597**, (2021).

[6] N. S. Taghavi, P. Gant, P. Huang, I. Niehues, R. Schmidt, S. Michaelis de Vasconcellos, R. Bratschitsch, M. García-Hernández, R. Frisenda, and A. Castellanos-Gomez, *Thickness Determination of MoS2, MoSe2, WS2 and WSe2 on Transparent Stamps Used for Deterministic Transfer of 2D Materials*, Nano Res. **12**, 1691 (2019).

[7] D. Bing, Y. Wang, J. Bai, R. Du, G. Wu, and L. Liu, *Optical Contrast for Identifying the Thickness of Two-Dimensional Materials*, Opt. Commun. **406**, 128 (2018).

[8] A. Han et al., *Growth of 2H Stacked WSe 2 Bilayers on Sapphire*, Nanoscale Horizons **4**, 1434 (2019).

[9] C. Jin et al., *Observation of Moiré Excitons in WSe2/WS2 Heterostructure Superlattices*, Nature **567**, 76 (2019).

[10] Y. Tang et al., *Simulation of Hubbard Model Physics in WSe2/WS2 Moiré Superlattices*, Nature **579**, 353 (2020).

[11] W. T. Hsu, B. H. Lin, L. S. Lu, M. H. Lee, M. W. Chu, L. J. Li, W. Yao, W. H. Chang, and C. K. Shih, *Tailoring Excitonic States of van Der Waals Bilayers through Stacking Configuration, Band Alignment, and Valley Spin*, Sci. Adv. **5**, 1 (2019).

[12] S. Miao et al., *Strong Interaction between Interlayer Excitons and Correlated Electrons in WSe2/WS2 Moiré Superlattice*, Nat. Commun. **12**, 8 (2021).

[13] Z. Chu et al., *Nanoscale Conductivity Imaging of Correlated Electronic States in WSe2/WS2 Moiré Superlattices*, Phys. Rev. Lett. **125**, 186803 (2020).

[14] D. Y. Qiu, F. H. da Jornada, and S. G. Louie, *Optical Spectrum of <math Display="inline"> <msub> <mi>MoS</Mi> <mn>2</Mn> </Msub> </Math> : Many-Body Effects and Diversity of Exciton States*, Phys. Rev. Lett. **111**, 216805 (2013).

[15] A. M. Jones, H. Yu, J. S. Ross, P. Klement, N. J. Ghimire, J. Yan, D. G. Mandrus, W. Yao, and X. Xu, *Spin-Layer Locking Effects in Optical Orientation of Exciton Spin in Bilayer WSe 2*, Nat. Phys. **10**, 130 (2014).

Chapter 6 Correlated Excitonic Insulator in 1L/2L WS_2/WSe_2 Moiré Superlattice

Two-dimensional (2D) moiré superlattices provide a highly tunable platform to study strongly correlated physics. Here, we report the observation of excitonic insulator, a correlated state with strongly bound electrons and holes, in the angle-aligned monolayer WS_2/natural bilayer WSe_2 moiré superlattice. Due to the highly interfacial moiré coupling, a flat miniband on the valence band side is induced only in the 1^{st}-WSe_2 layer interfacing WS_2. The electrostatically introduced holes first fill this miniband and form a Mott insulator at filling factor $n = -1$, corresponding to one hole per moiré supercell. By applying a vertical electric field, the dispersive valence band in the 2^{nd}-WSe_2 layer can be tuned to overlap with the moiré miniband in the 1^{st}-WSe_2 layer, realizing the coexistence of electrons and holes at equilibrium, which are bound as excitons due to strong Coulomb interaction. Combining optical spectroscopy and microwave impendence microscopy measurements, we show that this new bound state at the total filling factor of $n = -1$ is an excitonic insulator with a transition temperature as high as 90 K. Our study demonstrates a new moiré system for the study of correlated many-body physics in 2D and inspires engineering of novel quantum phases.

The content of this research is from my co-first authored paper, in which my contribution includes MIM measurements, data analysis and input for manuscript writing. Dongxue Chen[#], Zhen Lian[#], Xiong Huang[#], Ying Su[#] et al. Robust Excitonic Insulator in Heterojunction Moiré Superlattice, accepted by *Nature physics*

An excitonic insulator (EI) is a bound state of electron and hole pairs due to strong Coulomb interaction [1–3]. Motivated by its relevance to the Bose-Einstein condensation

(BEC), researchers have long been looking for this exotic quantum state, while the study is often hindered by low transition temperatures or elusive experimental signatures. Recently, two-dimensional (2D) moiré superlattices have emerged as a controllable material platform with strong Coulomb interaction, enabled by the formation of flat minibands in which the kinetic energy of charge carriers is substantially reduced. Meanwhile, thanks to their small bandwidth, these minibands make it possible to realize the coexistence of electrons and holes via band engineering, a prerequisite to forming EIs. The strong Coulomb interaction further provides the glue for the strong binding of electron-hole pairs. Here we explore the possibility of EI in the highly tunable moiré superlattice of angle-aligned transition metal dichalcogenides (TMD), which has been shown to exhibit particularly strong electron correlation, evidenced by the Mott insulator state with high transition temperatures and various correlated insulating states at fractional fillings of the moiré superlattice [4–6].

In this work, we study the moiré superlattice of angle-aligned monolayer WS_2/bilayer WSe_2 (1L/2L WS_2/WSe_2). We focus on the hole-doping regime as the valence band of TMD heterobilayers has been readily modeled for the study of a single band Hubbard model [7]. In WS_2/WSe_2 heterojunctions, the holes reside in the WSe_2 layers due to the type II alignment [8], and it has been demonstrated that the moiré coupling in the monolayer WS_2/monolayer WSe_2 will form a flat miniband in WSe_2 that enables the Mott insulator state at $n = -1$, one hole per moiré unit cell [6,8–12]. In the 1L/2L WS_2/WSe_2 moiré superlattice that we study here, the 2nd WSe_2 layer in the natural bilayer WSe_2, away from the WS_2/WSe_2 interface, contributes a parabolic valence band (VB2) that is

energetically close to the moiré miniband (MB1) in the 1st-WSe_2 layer at the interface (**Fig. 6.1e**). By applying an out-of-plane electric field, these two bands can overlap in energy, and the electrostatic doping can be used to simultaneously populate electron-like carriers in MB1 and hole-like carriers in VB2 (**Fig. 6.1f**), experimentally revealed by the optical signatures of exciton-polarons from the 2nd-WSe_2 layer. Using microwave impedance microscopy (MIM), we further find that the system goes into an insulating state at $n = -1$, at which the electron density in MB1 is equal to the hole density in VB2, confirming that these electrons and holes form a strongly bound EI state. This EI state is robust and exhibits a transition temperature as high as 90 K.

6.1 Optical Reflectance Study of Angle-Aligned 1L/2L WS_2/WSe_2 Heterojunction

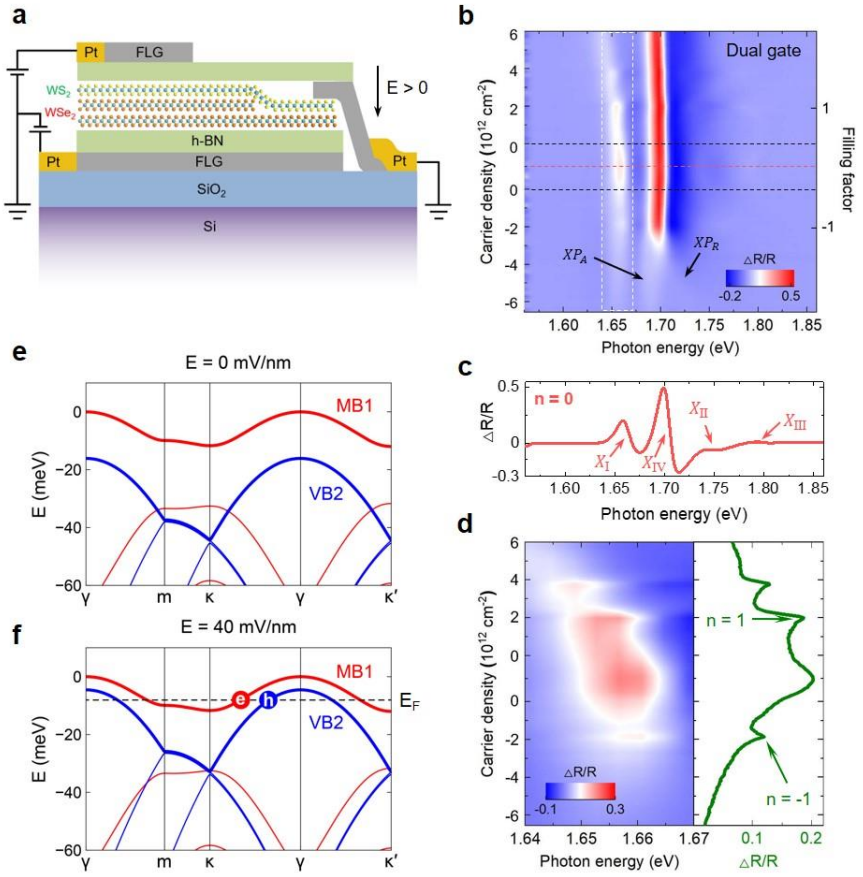

Figure 6.1 1L/2L WS_2/WSe_2 moiré superlattice. a, device structure for angle-aligned 1L/2L WS_2/WSe_2 heterojunction. **b**, Optical reflectance spectra as a function of carrier density (filling factor) with $E = 0$ at 5 K. **c**, Line cut of the optical spectra in (b) at charge neutral. **d**, Zoom-in of the white boxed region in (b) (left) and the peak intensity (right). **e** and **f** are calculations of the valence bands for the cases of E=0 (e) and E=40 mV/nm (f). MB1 is the flat miniband from the 1st-WSe_2 layer and the VB2 is the valence band from the 2nd-WSe_2 layer. When the Fermi level crosses both MB1 and VB2, carriers are electron-like in MB1 but hole-like in VB2.

As schematically shown in **Fig. 6.1a**, a typical device consists of a monolayer WS_2 angle aligned on top of a natural bilayer WSe_2, and the heterojunction is encapsulated with boron nitride (BN) flakes. The 1L/2L WS_2/WSe_2 (with the former layer on top) is dual-gated by few-layer graphene (FLG) electrodes on both top and bottom, which allows us to

independently control the doping density, n, and electric field, E which are determined by the following equations [13]:

$$n = C_{tg}V_{tg} + C_{bg}V_{bg} \qquad \& \qquad E = \frac{1}{2}\left(\frac{V_{tg}}{d_{tg}} - \frac{V_{bg}}{d_{bg}}\right)$$

where C_{tg} (C_{bg}) is the geometric capacitance of the top (back) gate, V_{tg} (V_{bg}) is applied voltage on top (back) gate electrode, and d_{tg} (d_{bg}) is the thickness for the top (back) hBN (dielectric constant chosen as 3.5).

We first investigate the optical signatures of the dual-gated heterojunction. Moiré coupling in TMD multilayer heterojunction has been shown to significantly modify the excitonic behaviors only at the moiré interface[26]. Therefore, the intralayer A exciton resonance in the 2nd WSe_2 layer remains at roughly the same energy and corresponds to the observed prominent X_{IV} peak.

The moiré exciton at the lowest energy, X_I, is sensitive to the carrier density and exhibits intensity resonances at electron or hole density of ~2.0×10^{12} cm^{-2}, which corresponds to the filling factor $n = +1/-1$ (one electron/hole per moiré unit cell), as shown in **Fig. 6.1d**. It is worth noting that, at $n = -1$, the moiré exciton X_{IV} remains the same as that in charge neural doping ($n = 0$). However, X_{IV} splits into attractive/repulsive exciton-polarons (XP_A/XP_R) at the increased doping around $n = -1.5$ (total hole density of ~3.0×10^{12} cm^{-2}). The exciton-polaron in TMDs arises from the many-body interaction between the intralayer exciton and the free carriers, with the exciton interacting with the Fermi sea of the opposite (same) valley leading to the red (blue) shifted attractive

[26] Please refer to study in the previous chapter for further reading.

(repulsive) exciton-polaron [14–17]. The doping dependence of X_{IV}, therefore, suggests that at $n = -1$ all the holes reside in the 1st-WSe_2 layer, and they start to fill the 2nd-WSe_2 layer at $n \sim -1.5$ for the $E = 0$ case. This observation inspires us to apply a vertical electric field to engineer the relative alignment of MB1 and VB2, which could allow holes to populate the 2nd-WSe_2 layer at much lower hole doping ($-1 < n < 0$). This is feasible according to our calculation (**Fig. 6.1f**), in which a positive electric field (pointing from WS_2 toward WSe_2) moves VB2 up relative to MB1. When E is large enough, VB2 can overlap with the flat MB1, which will allow hole carriers to transfer from the 1st-WSe_2 layer to the 2nd-WSe_2 layer. When the total doping is at a level such that both MB1 and VB2 are partially filled, i.e., the Fermi level lying in the overlap range, the carriers near the Fermi level in MB1 will be electron-like due to the positive band curvature near the bottom of the band. On the other hand, the carriers in VB2 are hole-like as they are near the top of the valence band. This band alignment creates an interesting scenario, in which electrons and holes can co-exist simultaneously but in different WSe_2 layers, setting up the stage for the formation of an EI.

6.2 Coexistence of Electrons and Holes in Bilayer WSe_2

We next experimentally demonstrate the coexistence of electrons and holes in separate WSe_2 layers by using an electric field to tune the band alignment. For each specific electric field, we measure the doping dependence of optical reflectance spectra, and the data for three characteristic electric fields are shown in **Fig. 6.2.** For all three cases, the moiré exciton X_I exhibits a resonance at a hole density of ~2.0×10^{12} cm^{-2}, corresponding to a total filling level of $n = -1$. However, the moiré exciton X_{IV}, which arises from the A

exciton response of the 2nd-WSe_2 layer, show different behaviors at different electric fields. At $E = -38$ mV/nm, the splitting of X_{IV} into two exciton-polarons XP_A and XP_R occurs at a high hole doping level corresponding to a total filling of $n\sim -2.3$. Before reaching this doping level, all the carriers should be in MB1. Therefore, the $n = -1$ state should correspond to the Mott insulator state at the half filling of MB1 with one hole per moiré unit cell. The strong on-site Coulomb repulsion splits the originally doubly degenerate MB1 into a lower Hubbard band (LHB) and an upper Hubbard band (UHB). For $n = -1$, the Fermi level lies just below the UHB, as illustrated in **Fig. 6.2g**. VB2, which starts to be filled at $n\sim -2.3$, should lie even below the LHB, consistent with the negative direction of the electric field that pushes holes to the 1st-WSe_2 layer (**Fig. 6.2d**). Under a positive electric field that moves VB2 up, the onset of the exciton-polaron is expected to occur at a lower hole doping. We find that at $E = 38$ mV/nm this onset occurs at roughly $n = -1$ (**Fig. 6.2b**). This suggests that the band maximum of VB2 is at the same energy level as the bottom of the UHB of MB1, as illustrated in **Fig. 6.2h**. The Fermi level at $n = -1$ should now touch both the bottom of the LHB and the top of VB2. As the electric field further increases, these two bands start to overlap, and when the total doping level is fixed at $n = -1$, some carriers will now transfer from the UHB to VB2 (**Fig. 6.2e and 2f**). From the perspective of electron-like carriers, the electron density in the UHB of MB1, n_e, is exactly the same as the hole density in VB2, n_h, i.e., $n_e = n_h$. The case of $E = 121$ mV/nm is such an example. The onset of exciton-polaron occurs clearly at a lower hole doping than $n = -1$ (**Fig. 6.2c**). Therefore, the $n = -1$ state corresponds to a state with

coexisting electrons in MB1 and holes in VB2 of equal densities, a potential candidate for an EI.

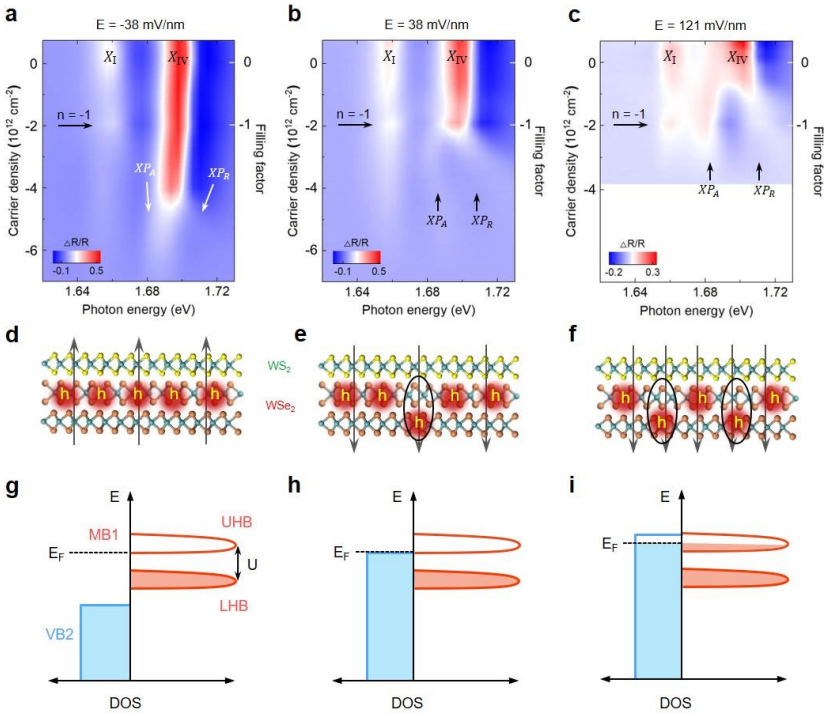

Figure 6.2 Electric field tuning of the band alignment in dual-gated 1L/2L WS_2/WSe_2. **a-c** the doping dependence of optical reflectance spectra at electric fields of -38 (a), 38 (b), and 121 (c) (mV/nm). **d-f** schematically show the distribution of holes in the two WSe_2 layers for (a)-(c), with the ellipse denotes the interlayer exciton formed. **g-i** show the schematics of the valence band alignment at total filling n=-1 corresponding to (a)-(c), respectively. The relative alignment between VB2 and MB1 is tuned by the electric field.

6.3 Excitonic Insulating States Probed by MIM

6.3.1 MIM on Dual-Gated 1L/2L WS_2/WSe_2 Heterojunctions

The remaining step is to show that this state is insulating, which we demonstrate by combining microwave impedance microscopy (MIM) and optical spectroscopy measurements. MIM measures the local conductivity in a small sample area (~100 nm) underneath the tip. For this measurement, we fabricated devices with a monolayer graphene (MLG) as the top gate in order to apply a vertical electric field (see schematics in Fig. 6.3a). We further apply a large magnetic field to form Landau levels (LLs) in MLG. In this

case, the bulk of MLG becomes much more insulating thus cannot completely screen the microwave electric fields from the tip. As a result, the penetrating fields are able to reach the WS_2/WSe_2 heterojunction and probe its conductivity through the top MLG gate. We then perform MIM measurement by tuning both the top MLG gate and bottom graphite gate to record a map of MIM signals. The MIM maps will exhibit features from both the top MLG (the LLs) and the WS_2/WSe_2 heterojunction (the correlated states).

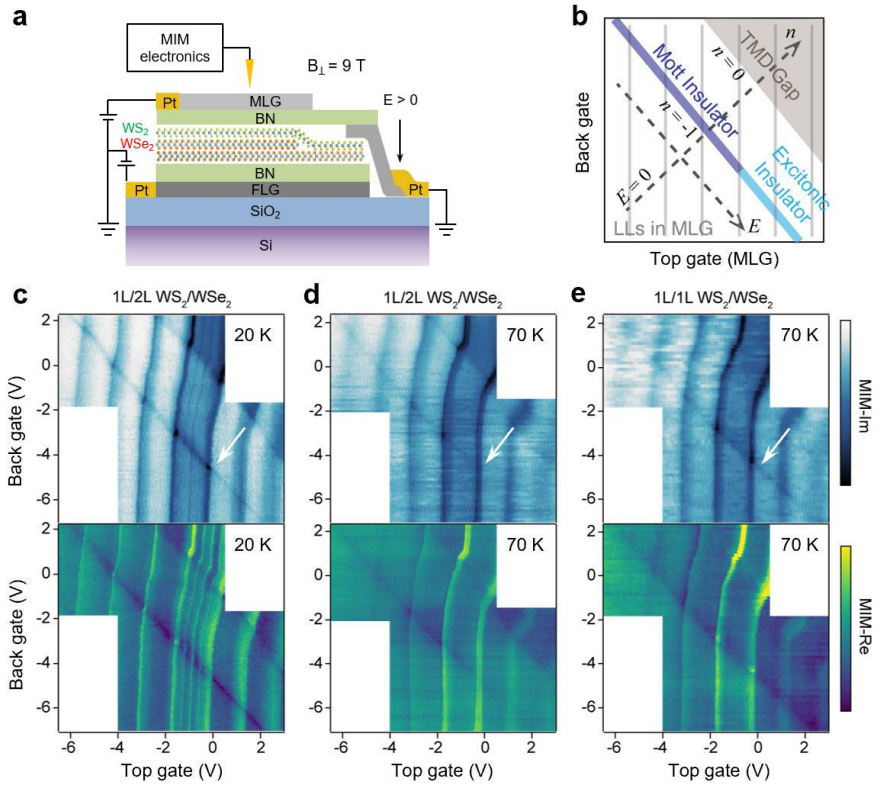

Figure 6.3 Transition between Mott insulator and EI states at $n = -1$ probed by MIM spectra. a, Schematic of a dual gated 1L/2L WS_2/WSe_2 device D1, same as the device in Fig. 1, but in a region with a monolayer graphene (MLG) as the top gate. **b**, Schematic of expected MIM features in a dual gate MIM map. (c)-(e) are color plots of MIM spectra as a function of top gate and back gate voltages for 1L/2L WS_2/WSe_2 region at 20 K (c) and at 70 K (d), and for 1L/1L WS_2/WSe_2 region at 70 K (e), respectively. The top panels are MIM-Im data and the bottom panels are MIM-Re data.

These two sets of features can be identified by their gate dependence. As illustrated in **Fig. 6.3b**, the LLs in the top MLG only depends on the potential difference between MLG and the sample but not on the bottom gate voltage, following the equation

$$n_G = C_{tg}(\frac{\mu_{moire}-\mu_G}{e} - V_{tg}),$$

where μ_{moire} is the chemical potential of TMD heterostructure and μ_G and n_G are chemical potential and carrier density of MLG. On the other hand, the correlated states in the heterobilayer should depend on both top and bottom gate voltages[27]. Indeed, the MIM maps show such two sets of features (**Fig. 6.3c - e**): the approximately vertical lines in the MIM maps correspond to the LLs which shift slightly as the TMD heterobilayer is driven near the charge neutral regions, likely due to changes in the chemical potentials in the sample and/or MLG; the diagonal lines correspond to features from the WS_2/WSe_2 heterojunction, and their directions are consistent with the dual gate geometry.

[27] Same analysis as in previous optical reflectance study.

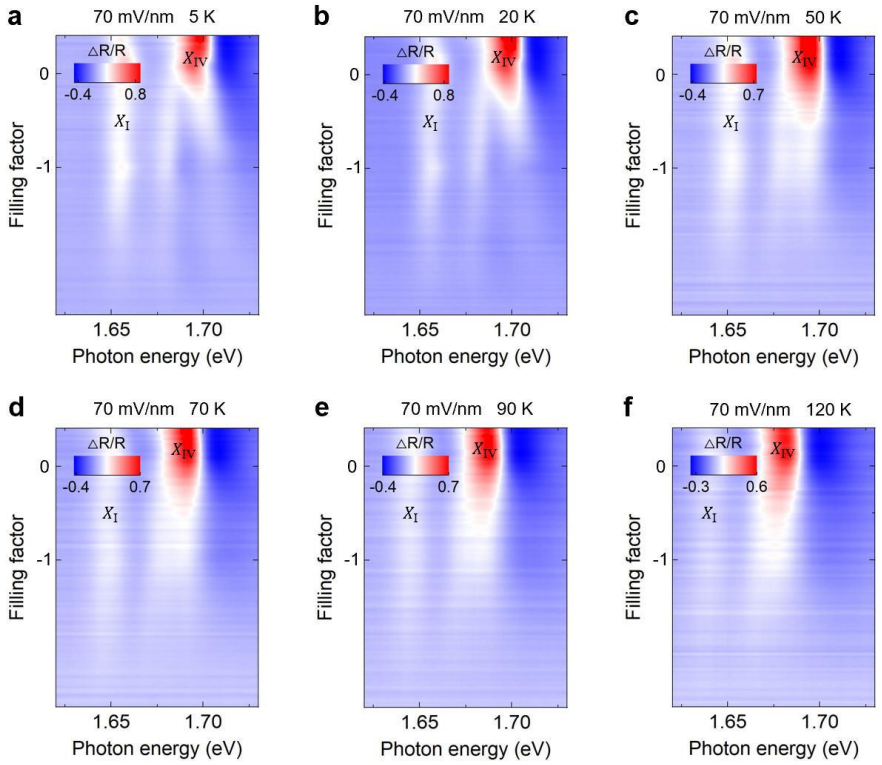

Figure 6.4 Doping-dependent reflectance spectra of the EI state for various temperatures. Under the electric field of 70 mV/nm, the dual-gated 1L/2L WS_2/WSe_2 (Device D1) is in the EI state at $n = -1$. It is evident that the resonance of moiré exciton X_I at $n = -1$ becomes less distinct as temperature increases, suggesting the melting of the EI state.

We clearly observe an insulating state at $n = -1$ which runs from the upper left to lower right corners. At 20 K (Fig. 6.3c), the $n = -1$ state remains insulating when the E field is varied in a range spanning from the Mott insulator to the expected EI states at the lower-right corner. The population of carriers in the second WSe_2 layer is confirmed by optical reflectance spectra in the same device shown in Fig. 6.4b at $E = 70\ mV/nm$. This suggests that the state at large positive electric fields, with both WSe_2 layers populated, is indeed insulating. But the Mott insulator and EI states are not readily distinguishable in the low temperature MIM map as both are insulating. On the other hand, the EI state is expected to have a lower transition temperature than the Mott insulator state due to the

further separation of interacting charges. We thus measure MIM maps at elevated temperatures. At 70 K, the insulating state disappears in the regime of large positive electric fields but persists through the rest of the E field range. As a comparison, the 1L/1L WS_2/WSe_2 region on the same device shows the $n = -1$ Mott insulator state clearly through the entire accessible E field range at 70 K, measured during the same experiment run.

These observations were also reproduced in another device with a reversed stacking order (2L/1L WSe_2/WS_2) (**Fig. 6.5**). Considering the device geometry, the MIM data map have a similar gate dependence as electric field with direction pointing from back gate to top gate can populate holes to 2^{nd}-WSe_2 layer and form an EI state (bottom corner in **Fig. 6.5**).

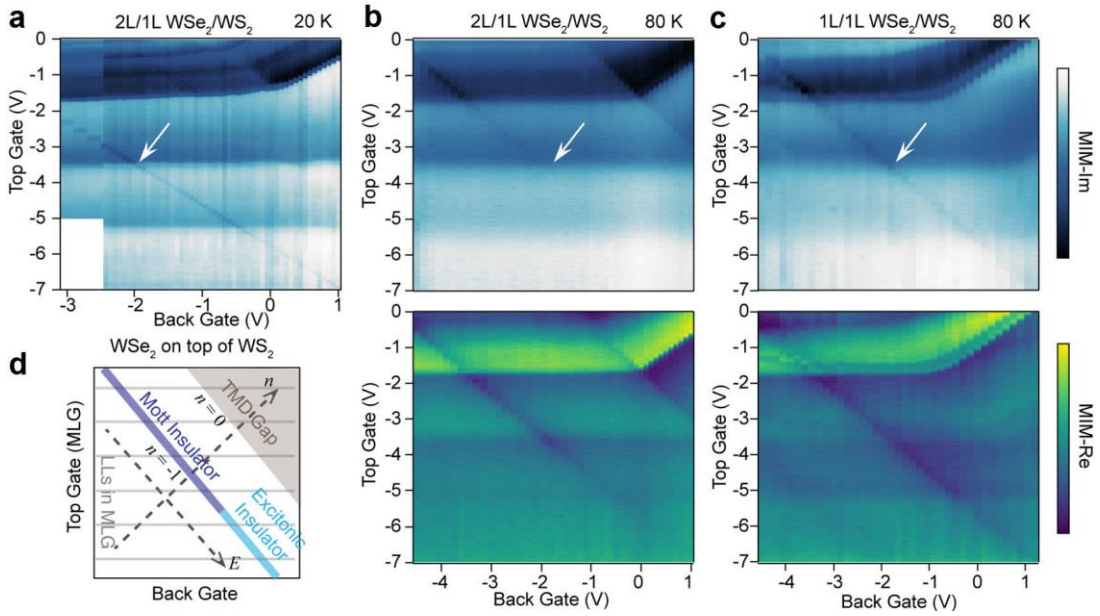

Figure 6.5 Electric field dependence of MIM spectra in 2L/1L WSe_2/WS_2 device. a-c are color plots of MIM spectra as a function of top gate and back gate voltages for 2L/1L WSe_2/WS_2 region at 20 K (a) and at 80 K (b), and for 1L/1L WSe_2/WS_2 region at 80 K (c), respectively. **d**, Schematic of expected MIM features in the dual gate MIM map. Note that the WSe_2 layer is on top of the 1L WS_2 layer in this device, therefore, the effects of top and back gates are opposite to that of device D1 presented in **Fig. 6.3**.

6.3.2 Excitonic Insulating State in Single-Gate Sample

We have also measured back-gate only devices with the same and reversed WS_2/WSe_2 stacking orders, as shown in **Fig. 6.6a**. In these device structures, the carrier density and electric field are coupled together as the back gate voltage is tuned. Since we focus on the hole-doping side of the heterojunctions, negative back gate voltages are applied which result in an E field pointing from the heterojunction to the back gate electrode as indicated by the arrows. As illustrated in **Fig. 6.6**, the $n = -1$ state corresponds to the EI state in the 1L/2L WS_2/WSe_2 structure and the Mott insulator state in the 2L/1L WSe_2/WS_2 structure, respectively (the configurations of carrier population in both cases are verified by optical reflectance measurement, see **Fig. 6.6c and e**). The T-

dependent MIM spectrum clearly show the insulating behavior in the EI state which has a transition temperature of 90 K in this device (Fig. 6.7b), consistent with the dual-gate device, and the slight difference might be due to sample variations and/or the weaker sensitivity of MIM to probe the insulating state through the MLG top gate.

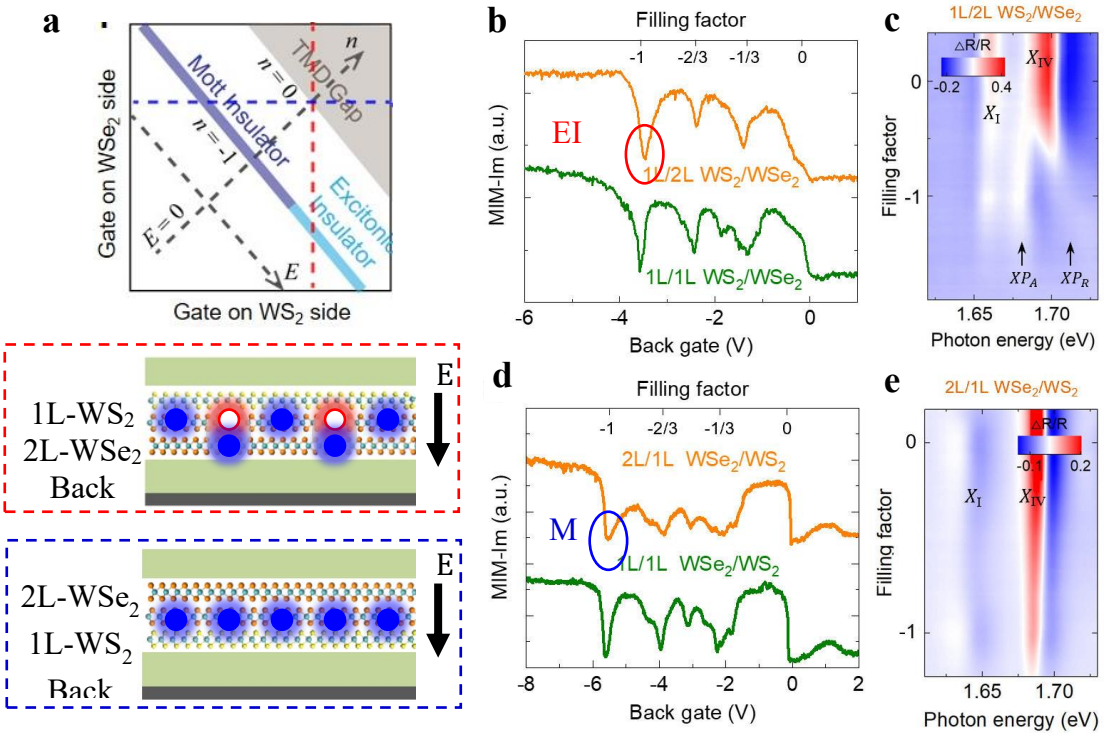

Figure 6.6. The insulating states at $n = -1$ in single gated WSe_2/WS_2 devices. a, Upper: expected single-gate MIM features (red and blue dash lines) in the dual gate MIM map. Lower: geometry for two single-gate devices studied. **b** and **d** are normalized MIM as a function of back gate voltage in WS_2/WSe_2 and heterojunctions at a temperature of 8 K. **c** and **e** are the gate-dependent optical reflectance spectra for 1L/2L WS_2/WSe_2 and 2L/1L WSe_2/WS_2 in **b**, respectively.

The combined MIM and optical spectroscopy data, therefore, support that this state $n = -1$, when holes partially populate the 2nd-WSe_2 layer, is an EI state. The equal number of electrons in MB1 and holes in VB2 are tightly bound as charge-neutral excitons due to the strong Coulomb interactions considering the small physical van der Waals (vdW) gap

between the 1st and 2nd layer WSe_2 (~0.3 nm)[28]. Since no free carriers are left behind, and the charge-neutral excitons do not contribute to any charge transport, the system is in an insulating state. This insulating state should be rather sensitive to the imbalance of electron and hole densities, which is reflected as the width of the insulating feature in the MIM spectra. We indeed find that the insulating feature at $n = -1$ becomes sharper in the EI regime compared to the Mott insulator regime (see **Fig. 6.3c**). The width of the conductance dip at $n = -1$ reflects the sensitivity to the $e - h$ imbalance. From our MIM data at 20 K (**Fig. 6.3c** and **Fig. 6.5a**), it does appear that the dip width in the EI state becomes narrower than that in the Mott insulator state. Our estimate is that the EI state exists for a density variation of $\delta n = 0.06$ while the Mott state has a variation of $\delta n = 0.10$ based on data in **Fig. 6.3c**. However, local inhomogeneity, such as variation in the twist angle or local doping, could also contribute to the broadening of the conductance dip. Therefore $\delta n = 0.06$ is an upper bound of the $e - h$ imbalance that can be tolerated for the EI state.

[28] Two recent study use a thin BN (~1 nm) to separate 1L/1L WS_2/WSe_2 and WSe_2 layers, which will result in a further separated electrons and holes, hence a weaker exciton binding energy [24,25].

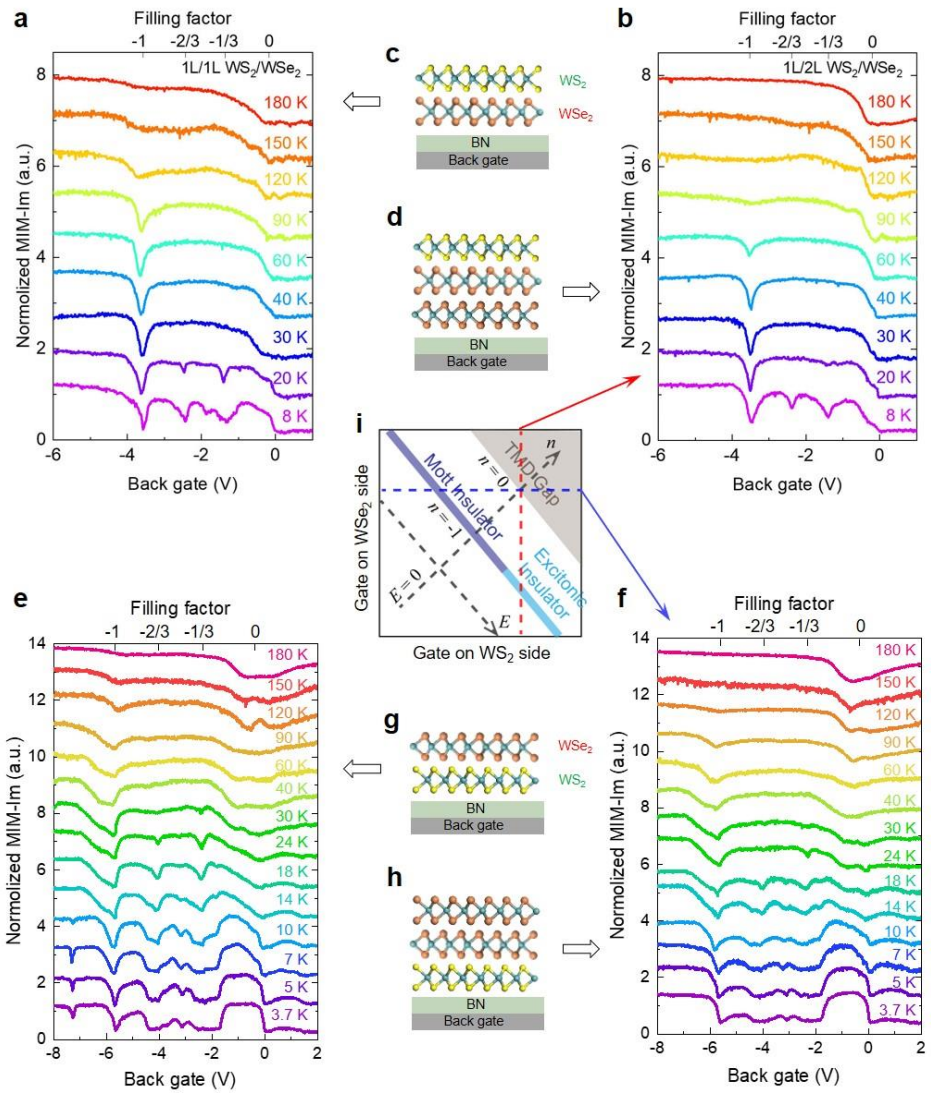

Figure 6.7 Temperature dependent MIM spectra of single-gated monolayer-WS_2/multilayer-WSe_2 devices with opposite stacking orders. a and **b** MIM spectra as a function of the hole doping for the single gated 1L/1L and 2L/1L WS_2/WSe_2 regions. **e** and **f** are doping dependent MIM spectra for the 1L/1L and 2L/1L WSe_2/WS_2 regions. The MIM spectra in **b** and **f** are equivalent to the red and blue linecuts in the schematic of the dual gate map in (i). Therefore, the $n = -1$ states in **b** and **f** correspond to the EI and Mott insulator state, respectively.

We note that the EI transition temperatures in this system are much higher than what was reported in two-dimensional electron gas (2DEG) based EI systems [18,19] or the EI in bilayer graphene [20,21]. The robustness of the EI originates from the strong

correlation in the flat moiré miniband and the strong Coulomb interaction that leads to the large binding energy of the interlayer excitons across the vdW bilayer WSe_2.

6.4 Exciton-Polarons Confirmed by Helicity-Resolved Magneto-Reflectance Spectroscopy

Finally, we use helicity-resolved magneto-reflectance spectroscopy to further confirm the exciton-polarons and the correlation of holes from the 1st and 2nd layer WSe_2 in the EI state. The exciton-polarons arise from the interaction between the intralayer exciton and the carriers in the same (attractive exciton-polaron) or opposite valley (repulsive exciton-polaron). An out-of-plane magnetic field lifts the valley degeneracy and leads to an energy difference between valence bands from K and K' valleys. As a result, the hole doping will start to first fill one particular valley, say K valley, the screening of the excitons in the opposite (K') or the same valley (K) will result in the attractive (repulsive) exciton polaron [14–17]. To confirm this, we excite the device with right (left) circularly polarized light, σ^+ (σ^-), and probe the reflectance contrast in the right (left) circularly polarized channel. The data obtained from an out-of-plane magnetic field of 4 T is shown in **Fig. 6.8**. Under the electric field of 69 mV/nm, the 1L/2L WS_2/WSe_2 heterojunction is at the EI state, and it is obvious that the intralayer exciton from the 2nd layer WSe_2 (X_{IV}) behaves as an attractive exciton polaron (**Fig. 6.8a**) in the $\sigma^-\,\sigma^-$ measurement configuration and repulsive exciton polaron in the $\sigma^+\,\sigma^+$ configuration (**Fig. 6.8b**) at $n = -1$.

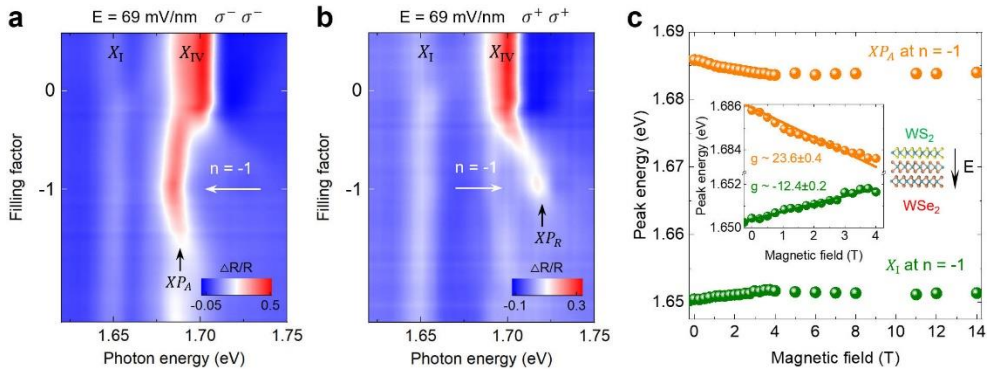

Figure 6.8 Helicity-resolved magneto-reflectance spectra under an out-of-plane magnetic field. a and **b** are doping-dependent reflectance spectra from K' and K valley for an angle-aligned 1L/2L WS_2/WSe_2 device at $E = 69$ mV/nm and $B = 4$ T, showing the XP_A and XP_B, respectively. **c** Energy of XP_A and X_I at $n = -1$ as a function of B field. Inset shows the g factor obtained by fitting the Zeeman shift below the saturation field (~4 T).

We further measure the Zeeman shifts of both the attractive exciton polaron, XP_A, and the moiré exciton X_I at the EI state ($n = -1$ in **Fig. 6.8a**). The Zeeman splitting [22] of the absorption peaks are defined by $E = E_0 \pm \frac{1}{2} g\mu_B B$, where g is the Landé g-factor and μ_B is the Bohr magneton. The "+" and "–" signs are for the absorption peak energies from the K and K′ valleys, respectively. As shown in **Fig. 6.8c**, both XP_A and X_I exhibit unique dependence on the magnetic field: a large Zeeman shift in the relatively low magnetic field regime, characterized by a g-factor much larger than 4, which then saturate at high magnetic field. In contrast, when 1L/2L WS_2/WSe_2 is in the Mott insulator state ($n = -1$), the X_{IV} intralayer exciton in the 2nd WSe_2 layer shows a Zeeman splitting expected for a typical intralayer exciton in WSe_2, with a g-factor value about 4. The magnetic field dependence of the moiré exciton X_I at $n = -1$ has been reported previously [5], which was ascribed to the magnetic properties of the ground state of the Mott insulator [5,7] in 1L/1L WS_2/WSe_2. Here, in the EI state of the 1L/2L WS_2/WSe_2, although part of the holes is moved to the 2nd-WSe_2, these holes are still strongly correlated

magnetically with the holes in the 1st-WSe_2, therefore the associated exciton polaron exhibits a similar Zeeman splitting behavior. On the other hand, when the 1L/2L WS_2/WSe_2 is tuned to the Mott insulator state, all the correlated holes are confined in the 1st-WSe_2. The X_{IV} is essentially the A exciton from the 2nd-WSe_2, with an expected "normal" g-factor of intralayer exciton, ~4. Only the holes in the 1st-WSe_2 form a Mott insulator state, thus giving rise to the Zeeman shift of moiré exciton X_I that show the magnetic properties of the ground state.

6.5 Conclusion

In summary, we have demonstrated a new heterojunction moiré system exploiting the layer degree of freedom in the angle-aligned monolayer WS_2/bilayer WSe_2 device. The highly interfacial nature of the moiré coupling effectively decouples the two WSe_2 layers, creating two neighboring bands that are spatially separated but energetically close. Their energy proximity allows flexible tuning of the band alignment using an electric field. The flat miniband, with its small bandwidth and low carrier density, provides a knob to manipulate carrier polarity by band filling. The spatial proximity enables strong Coulomb interactions as the bonding glue. All these factors are essential for the realization of EI in this moiré system and provide highly flexible means for engineering new quantum states under strong electron interaction, such as the superfluidity in an EI system [23].

References

[1] B. I. Halperin and T. M. Rice, *Possible Anomalies at a Semimetal-Semiconductor Transition,* Rev. Mod. Phys. **40**, (1968).

[2] N. F. Mott, *The Transition to the Metallic State*, Philos. Mag. **6**, 287 (1961).

[3] D. Jérome, T. M. Rice, and W. Kohn, *Excitonic Insulator*, Phys. Rev. **158**, 462 (1967).

[4] E. C. Regan et al., *Mott and Generalized Wigner Crystal States in WSe2/WS2 Moiré Superlattices*, Nature **579**, 359 (2020).

[5] Y. Tang et al., *Simulation of Hubbard Model Physics in WSe2/WS2 Moiré Superlattices*, Nature **579**, 353 (2020).

[6] X. Huang et al., *Correlated Insulating States at Fractional Fillings of the WS2/WSe2 Moiré Lattice*, Nat. Phys. **17**, 715 (2021).

[7] F. Wu, T. Lovorn, E. Tutuc, and A. H. Macdonald, *Hubbard Model Physics in Transition Metal Dichalcogenide Moiré Bands*, Phys. Rev. Lett. **121**, 26402 (2018).

[8] S. Miao et al., *Strong Interaction between Interlayer Excitons and Correlated Electrons in WSe2/WS2 Moiré Superlattice*, Nat. Commun. **12**, 8 (2021).

[9] Z. Chu et al., *Nanoscale Conductivity Imaging of Correlated Electronic States in WSe2/WS2 Moiré Superlattices*, Phys. Rev. Lett. **125**, 186803 (2020).

[10] E. C. Regan et al., *Mott and Generalized Wigner Crystal States in WSe2/WS2 Moiré Superlattices*, Nature **579**, 359 (2020).

[11] Y. Xu, S. Liu, D. A. Rhodes, K. Watanabe, T. Taniguchi, J. Hone, V. Elser, K. F. Mak, and J. Shan, *Correlated Insulating States at Fractional Fillings of Moiré Superlattices*, Nature **587**, 214 (2020).

[12] Y. Tang et al., *Simulation of Hubbard Model Physics in WSe2/WS2 Moiré Superlattices*, Nature **579**, 353 (2020).

[13] M. Sui et al., *Gate-Tunable Topological Valley Transport in Bilayer Graphene*, Nat. Phys. **11**, 1027 (2015).

[14] D. K. Efimkin and A. H. MacDonald, *Many-Body Theory of Trion Absorption Features in Two-Dimensional Semiconductors*, Phys. Rev. B **95**, 1 (2017).

[15] D. K. Efimkin and A. H. Macdonald, *Exciton-Polarons in Doped Semiconductors in a Strong Magnetic Field*, Phys. Rev. B **97**, 1 (2018).

[16] T. Wang et al., *Observation of Quantized Exciton Energies in Monolayer WSe_2 under a Strong Magnetic Field*, Phys. Rev. X **10**, 021024 (2020).

[17] T. Smoleński et al., *Interaction-Induced Shubnikov-de Haas Oscillations in Optical Conductivity of Monolayer MoSe2*, Phys. Rev. Lett. **123**, 97403 (2019).

[18] L. Du, X. Li, W. Lou, G. Sullivan, K. Chang, J. Kono, and R. R. Du, *Evidence for a Topological Excitonic Insulator in InAs/GaSb Bilayers*, Nat. Commun. **8**, 1 (2017).

[19] J. P. Eisenstein, *Exciton Condensation in Bilayer Quantum Hall Systems*, Annu. Rev. Condens. Matter Phys. **5**, 159 (2014).

[20] X. Liu, Z. Hao, K. Watanabe, T. Taniguchi, B. I. Halperin, and P. Kim, *Interlayer Fractional Quantum Hall Effect in a Coupled Graphene Double Layer*, Nat. Phys. **15**, 893 (2019).

[21] J. I. A. Li, T. Taniguchi, K. Watanabe, J. Hone, and C. R. Dean, *Excitonic Superfluid Phase in Double Bilayer Graphene*, Nat. Phys. **13**, 751 (2017).

[22] Z. Li et al., *Momentum-Dark Intervalley Exciton in Monolayer Tungsten Diselenide Brightened via Chiral Phonon*, ACS Nano **13**, 14107 (2019).

[23] M. M. Fogler, L. V. Butov, and K. S. Novoselov, *High-Temperature Superfluidity with Indirect Excitons in van Der Waals Heterostructures*, Nat. Commun. **5**, 1 (2014).

[24] J. Gu, L. Ma, S. Liu, K. Watanabe, T. Taniguchi, J. C. Hone, J. Shan, and K. F. Mak, *Dipolar Excitonic Insulator in a Moiré Lattice*, Nat. Phys. **18**, 395 (2022).

[25] Z. Zhang et al., *Correlated Interlayer Exciton Insulator in Double Layers of Monolayer WSe2 and Moir\'e WS2/WSe2*, *arXiv:2108.07131 (2021)*.

Chapter 7 Intertwined Topological and Magnetic Orders in Atomically Thin Chern Insulator

Strong correlation and topology are two central threads for modern condensed matter physics research [1]. In the previous chapter, we talk about electron strong correlation and emergent correlated insulating states in semiconducting TMD moire system. In this chapter, I will talk about our recent research on intrinsic magnetic topological insulator system. The content of this research was published in my co-first authored paper, in which my contribution includes MIM measurements, data analysis and input for manuscript writing.

Ovchinnikov, D., **Huang, X.**, Lin, Z., Fei, Z. *et al.* Intertwined Topological and Magnetic Orders in Atomically Thin Chern Insulator MnBi2Te4. *Nano Lett.* **21**, 2544–2550 (2021). [2]

$MnBi_2Te_4$, a van der Waals magnet, is an emergent platform for exploring Chern insulator physics. Its layered antiferromagnetic order was predicted to host even-odd layer number dependent topological states. Furthermore, it becomes a Chern insulator when all spins are aligned by an external magnetic field. Here, we explore how the evolution of bulk electronic structure as the magnetic state is continuously tuned and its dependence on layer number (even or odd). Employing multimodal probes, we establish one-to-one correspondence between bulk electronic structure, magnetic state, topological order, and layer thickness in atomically thin $MnBi_2Te_4$ devices. As the magnetic state is tuned through the canted magnetic phase, we observe a band crossing, i.e., the closing and reopening of the bulk band gap, corresponding to the concurrent topological phase

transition in both even- and odd-layer-number devices. Our findings shed new light on the interplay between band topology and magnetic order in this newly discovered topological magnet.

7.1 Introduction to Intrinsic Magnetic Topological Insulator: $MnBi_2Te_4$

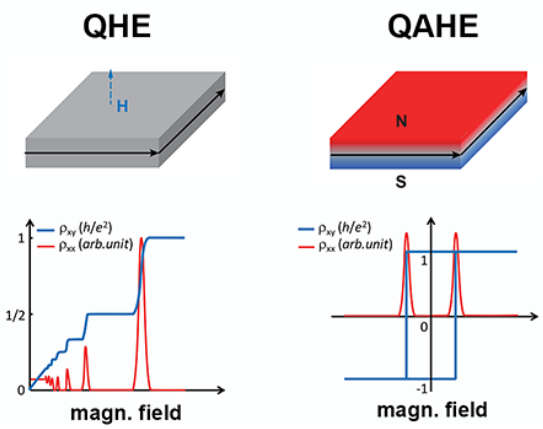

Figure 7.1 Quantized version of Hall effect and anomalous Hall effect. a, The quantum Hall effect (QHE) occurs in a 2D electron system subjected to an applied magnetic field. **b**, The quantum anomalous Hall effect with quantized Hall resistance without an applied magnetic field. From *The Quantum Hall Effect Gets More Practical*, APS ViewPoint.

In 1980, von Klitzing et al. discovered a fully quantized Hall resistance for a 2D electron system in the inversion layer of a MOSFET (metal-oxide-semiconductor field-effect transistor) when subjected a strong magnetic field (18 T) [3]. The unexpected integer quantum Hall effect (IQHE) was later awarded the 1985 Nobel Prize in Physics[29]. In two dimensions, electrons will follow cyclotron orbits and form landau levels when subjected to a magnetic field at low temperatures. As shown in **Fig. 7.1a**, the Hall resistance shows plateaus of quantized values of $h/\nu e^2$ with a vanishing longitudinal resistance when the ν-th Landau level is fully filled (h is Plank's constant and e is the elementary charge constant). Later, it was realized that ν is a topological invariant which is insensitive to the actual geometry of the system. The topological invariant (the Chern number, also known

[29] https://en.wikipedia.org/wiki/Quantum_Hall_effect

as the Thouless–Kohmoto–Nightingale–Nijs invariant), is expressed by the integral of Berry curvature in the 2D Brillouin zone,

$$C = \frac{1}{2\pi}\sum_m d^2k(\nabla_k \times A_m),$$

where $\nabla_k \times A_m$ is the Berry curvature for the m-th occupied band A_m. Usually, a 2D electron system can be classified as topologically trivial ($C = 0$) or nontrivial ($C \neq 0$). Vacuum is a topologically trivial insulator. There exist topologically nontrivial insulators with different band topology ($C \neq 0$). At the boundary between topological nontrivial materials and trivial insulators (*e.g.*, vacuum), gapless edge states emerge due to the distinct band topology. Electrons in these edge modes travel unidirectionally along the boundary and has certain chirality. Elastic backscattering by non-magnetic impurities is forbidden since there is no available electronic states. Therefore, these chiral edge states are dissipation-less and propose a concept for low-power-consumption electronics and also spintronics application [4,5].

Symmetry plays an important role in topological materials. The Chern number is zero for a material with time-reversal symmetry [6,7]. For time-reversal invariant systems, another type of topological invariant was proposed as the Z_2 invariant by Kane and Mele in 2005 [6,7]. $Z_2 = 0$ or 1, depending on the parity of the intersection number between the edge states and the fermi level. A 2D time-reversal invariant system is considered topologically trivial ($Z_2 = 0$) when edge states intersect the fermi level at even number of times. When $Z_2 = 1$, the system is considered a topological insulator (TI) with edge states intersecting fermi level at odd number of times and persist within the bulk energy gap. The first discovered 2D TIs are $HgTe/CdTe$ [8] and $InAs/GaSb$ [9] quantum wells as well as

monolayer $1T'$- WTe_2 [10–12]. The Z_2 classification can be extended to 3D systems as distinguishing 3D TIs (weak or strong). A weak 3D TI can be considered as stacked 2D TIs with easily destroyed gapless surface states where a strong 3D TI has robust gapless surface states at all surfaces. In a strong 3D TI, 2D surface states exhibit helical spin texture with spin-momentum locking. Backscattering is also forbidden. One representative 3D TI is the Bi_2Te_3 family whose helical gapless surface states have been confirmed by angle-resolved photoemission spectroscopy [13,14].

Magnetism can be introduced to break the time-reversal symmetry and the magnetic exchange interaction can open an energy gap in the otherwise gapless surface states. A chiral edge mode can form at the boundary and contributes quantized Hall conductance (e^2/h). This is known as the quantum anomalous Hall effect (QAHE) or quantum Hall effect without Landau levels [15], no requirement of an external magnetic field in the case of IQHE (**Fig. 7.1b**). There are two ways to introduce magnetism, such as magnetic doping and magnetic proximity effect. The first experimental realization of QAHE is in a Cr-doped $(Bs, Sb)_2Te_3$ TI film [16]. In this system, a precise control of the ratio of the multiple elements in this nonstoichiometric material is required. The randomly distributed magnetic dopants could act as impurities which limit the sample quality with non-ferromagnetic (FM) regions even below the Curie temperature. Electrons in the topological channel can be scattered by electrons from the surface states or bulk band of the non-FM regions. As a result, QAHE can only be observed at very low temperatures ($\sim$30 mK), which is much lower than the actual Curie temperature (a few tens of kelvin) [17] and the exchange gap

(hundreds of kelvin) [18] in the material. On the other hand, the QAHE is yet to be confirmed through magnetic proximity effect.

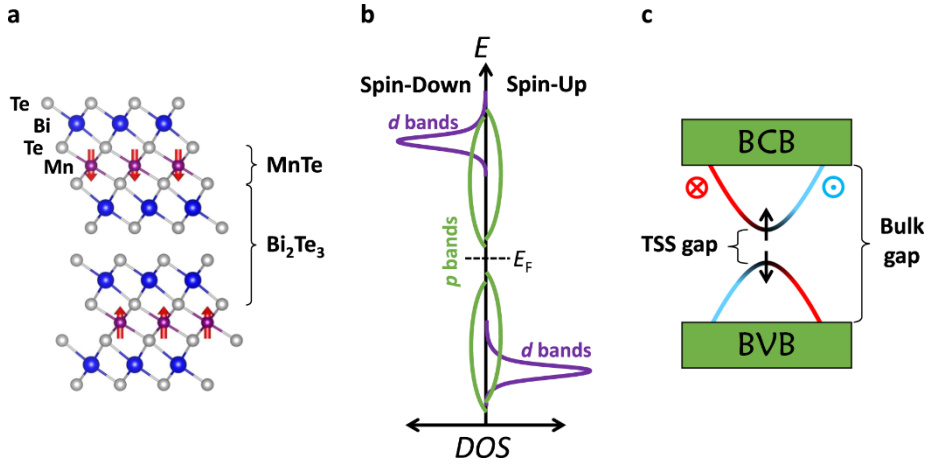

Figure 7.2 Lattice and electronic structures for $MnBi_2Te_4$. a, Lattice structure for $MnBi_2Te_4$. **b**, Electronic band structure for different orbitals. **c**, Magnetically induced energy gap for the topological surface states. Adapted from REF 22, Copyright ACS.

In a recent work in 2017, first-principles calculation predicted experimentally feasible septuple layers of the tetradymite-type compounds [19]. When a magnetic MnTe bilayer is inserted into a quintuple layer of Bi_2Te_3, a $MnBi_2Te_4$ septuple layer is formed with a large magnetic exchange gap ($\sim$77 meV) opening at the topological surface states. This promises that $MnBi_2Te_4$ can be a robust QAHE candidate. Using molecular beam epitaxy technique, researchers found that the magnetic doping process (Mn) in Bi_2Te_3 thin film spontaneously forms a stoichiometric $MnBi_2Te_4$ septuple layers (SL) rather than the chemical substitution of Bi by Mn atoms [20]. This leads an experimental realization of intrinsic magnetic topological insulator. Soon the single crystal $MnBi_2Te_4$ was experimentally realized [21]. This van der Waals magnet consists of $Te-Bi-Te-Mn-Te-Bi-Te$ septuple layers as shown in Fig. 7.2a. The Mn^{2+} ions with a high spin of $S=$

$5/2$ and a large magnetic moment of $\sim 5\ \mu_B$ (Bohr magneton) contribute the intrinsic magnetism. Below its Neel temperature (~ 25 K), the material has a ferromagnetically coupled spins within each SL and a magnetic anisotropy with an out-of-plane (z) easy axis. The adjacent SLs are anti-ferromagnetically coupled which makes a bulk $MnBi_2Te_4$ an antiferromagnet (AFM). As calculated (**Fig. 7.2b**), the energy bands near the fermi level are dominated by the *p* orbitals of Bi and Te which contribute the TI property [22]. The energy bands of Mn atoms are several eV away from fermi level but the hybridization between these *p* and *d* bands are still strong enough to induce a magnetic exchange gap for the topological surface states as shown in **Fig. 7.2c**. This AFM state can be further driven into canted antiferromagnetic (cAFM) and FM phases by applying a magnetic field. The coupling of different magnetic configurations to the topological properties can lead to a variety of topological phenomena. Importantly, few -layer $MnBi_2Te_4$ can have a net layer of uncompensated magnetization when the layer number is odd together with zero-magnetization even-layer samples. It is predicted that, in the AFM ground state without applying B field, an odd-layer sample will host the QAHE while the even-layer samples are expected to be axion insulators [23–25]. Recent progress has been made on exfoliated few-layer $MnBi_2Te_4$ devices and QAHE has been reported in one 5-SL device at zero magnetic field [26] (note [30]). Chern insulators have been observed in both odd- and even-layer samples in the magnetic-field-driven FM states [26–29]. These promising results point to few-layer $MnBi_2Te_4$ as a desirable platform to study the correlation between magnetic order and band topology. In these reported studies, corresponding magnetic states

[30] Only one odd-layer device shows QAHE to our best knowledge.

are usually inferred from Hall measurements. A direct correlation between magnetic and topological orders is yet to be established. It is also important to unravel the evolution of the bulk electronic band structure as the magnetic state is tuned (between AFM, cAFM and FM). The unique layer number effect should be carefully examined during this process.

7.2 Sample Preparation: Layer Number Assignment and Device Fabrication

Bulk $MnBi_2Te_4$ crystals from Oak Ridge National Lab were grown out of a $Bi-Te$ flux [6]. Scotch-tape exfoliation method is used to obtain few-layer $MnBi_2Te_4$ onto 285 nm thick SiO_2/Si substrates. Standard electron beam lithography, employing 300 nm PMMA[31] resist and thermal evaporation of Cr (5 nm) and Au (50 nm) is used after lift-off[32] process. The transport devices[33] were covered by PMMA during all measurements to prevent degradation.

[31] Also known as polymethyl-methacrylate.
[32] See wiki-pedia for lift-off process.
[33] Note that device 5SL-2 is made from another crystal grown by Y. Wu at Tsinghua University, Beijing, China.

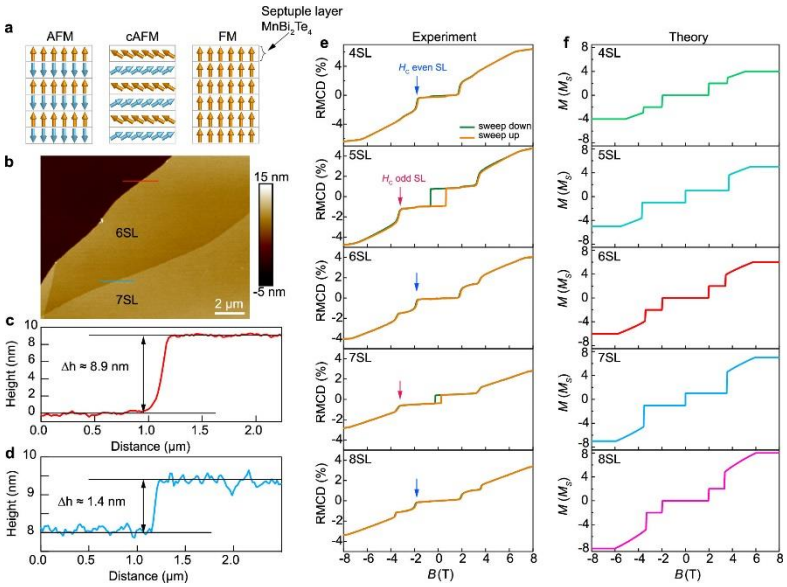

Figure 7.3 Layer-dependent magnetic order in thin flakes of $MnBi_2Te_4$. a, Different magnetic configurations for $MnBi_2Te_4$. **b**, Atomic force microscopy image of freshly exfoliated flake (with regions containing 6SL and 7SL). **c** and **d**, Height profiles across the step edges marked by colored arrows. **e**, Reflective magnetic circular dichroism (RMCD) measurements on freshly exfoliated flakes at 2K. **f**, Theoretical modeling for the magnetic response for total magnetization of $4-8$ SL flakes. Adapted from REF 2, Copyright ACS.

The total magnetization behavior should be distinct between even- and odd-layer samples. First, we use reflective magnetic circular dichroism (RMCD)[34] to investigate this even-odd effect on freshly exfoliated flakes. By exfoliation, we have flakes with regions having different thickness as measured by atomic force microscopy. The layer numbers can be assigned by dividing the total thickness to a single SL height (~1.4 nm) as shown in **Fig. 7.3 b-d**. We performed RMCD measurements on a series of flakes with thickness ranging from 4 to 8 SL as shown in **Fig. 7.3e**. The overall shape for each curve shows a B-field dependent magnetization when the sample is tuned from AFM phase to cAFM and FM, eventually (**Fig. 7.3a**). Two major differences are observed between even and odd

[34] Refer to Appendices for details on RMCD experiments.

layers. First, a pronounced hysteresis loops and significant remanent RMCD signal around zero field indicate the uncompensated magnetic moments in odd (5SL and 7SL) layers in the AFM state. For even (4SL, 6SL and 8SL) samples, the RMCD signals and hysteresis loops are vanishingly small, consistent with the zero net magnetization around zero magnetic field. The switching field (labeled by the arrows, red and blue) for the spin-flop transition (from AFM to cAFM phases) are different: $\sim$1.8 T for even-layer samples and $\sim$3.8 T for odd-layer samples. Notice that these observations are qualitatively consistent with a recent report [30]. The larger H_C for odd SL can be explained by the Zeeman energy of the uncompensated magnetization, which stabilizes the AFM state. Our theoretically modeling of magnetization vs applied magnetic fields well captures the odd-even layer dependent RMCD signal. Thus, we have demonstrated RMCD as a complementary and reliable method to distinguish the even and odd SL flakes.

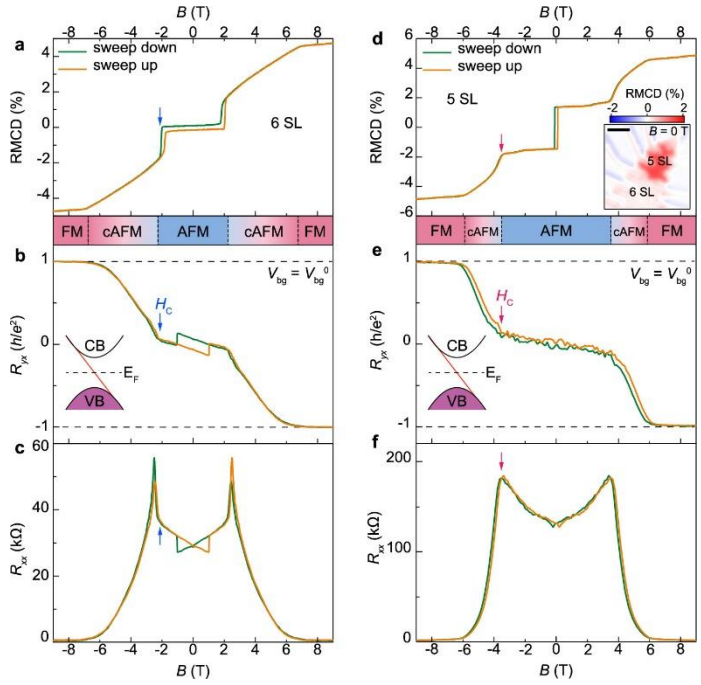

Figure 7.4 Correlation of magnetic order and topological properties of even- (6SL-1) and odd-layer (5SL-1) devices. RMCD signal (**a** and **d**), anti-symmetrized Hall resistance (R_{yx}, **b** and **e**) and symmetrized longitudinal resistance (R_{xx}, **c** and **f**) as a function of magnetic field at 2 K for 6SL and 5SL devices, respectively. Adapted from REF 2, Copyright ACS.

7.3 The Interplay Between Magnetic State and Topological Order

We then focus on investigation of the correlation between magnetic states and topological orders in both 5-SL and 6-SL MBT devices with back gate electrodes to tune the carrier density. The RMCD and transport data are plotted side-by-side in **Fig 7.4**. To be noticed, a back gate voltage (V_{bg}^0) is applied for these two devices to keep the fermi level within the bulk gap, which is confirmed from the analysis later. The RMCD signals of these devices after fabrication (**Fig 7.4 a** and **d**) are almost consistent with freshly cleaved flakes. For the 6SL-2 device, a tiny hysteresis loop together with a nearly vanishing signal is observed when the sample is in AFM state around zero magnetic field. It could be a result of uncompensated magnetization initiated by fabrication (similar behavior has been

reported on 2D layered AFM CrI_3 [31]). Spatial dependence of RMCD is performed on this 6-SL device as shown in Fig. 7.5. We notice additional hysteresis transitions on both natural and pre-cut edges. On the other side (Fig. 7.4d), the odd-layer device (5SL-1) clearly shows an expected hysteresis loop centered around B = 0 T with remnant RMCD signals (~28% of the saturated magnetization in FM state). A spatial RMCD map at 0 T (inset of Fig. 7.4d) shows a uniform signal, suggesting large magnetic domains. The magnetic phases information is labeled at the bottom of the RMCD plot for each device in Fig. 7.4a and 7.4d.

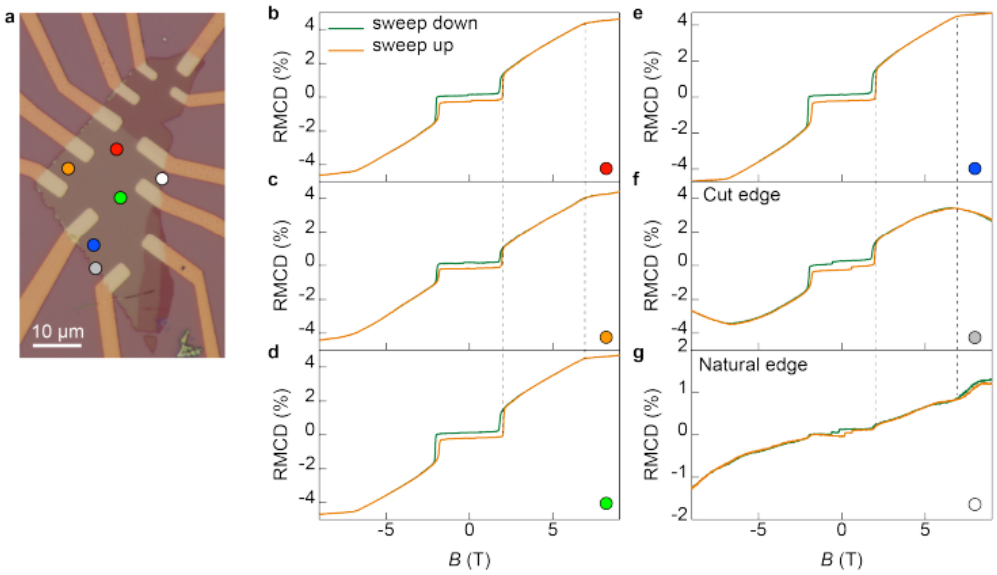

Figure 7.5 RMCD for selected spots of 6SL-1. a, optical image of device 5SL-1 and 6SL-1 with spots marking the spatial locations of spectra (**b** - **g**). **b** – **g**, RMCD signals as a function of applied magnetic field at selected positions as indicated in **a**. Adapted from REF 2, Copyright ACS.

The transport data also shows rising points for the spin-flop fields which are consistent with the RMCD measurements. Note that the Hall resistance data have been anti-symmetrized while the longitudinal resistance have been symmetrized to remove the

mixing of the two components. The symmetrization and anti-symmetrization procedures are as the followings:

$$R_{yx}^{\uparrow(\downarrow)}(B) = \frac{1}{2}[R_{yx}^{\uparrow(\downarrow)}(B) - R_{yx}^{\downarrow(\uparrow)}(-B)],$$

$$R_{xx}^{\uparrow(\downarrow)}(B) = \frac{1w}{2l}[R_{xx}^{\uparrow}(B) + R_{xx}^{\downarrow}(-B)],$$

where ↑ (↓) for field sweep up (down). w and l are the estimated width and length of the transport channel, respectively. For both devices, a Chern insulator ($C = -1$) is observed in the magnetic-field-induced FM state ($B > 6$ T) with a quantized Hall resistance ($R_{yx} = -{}^{h}/_{e^2}$) and a vanishing longitudinal resistance (R_{xx}). As shown in **Fig. 7.4b**, in the AFM state of the even sample (6SL-1), R_{yx} is small while R_{xx} is large. Despite a nearly identical RMCD signal compared with freshly cleaved flakes, R_{yx} has a small hysteresis loop with a coercive field at lower magnetic field than the spin-flop value. From our spatially resolved RMCD spectra in **Fig. 7.5**, small hysteresis loops like that in R_{yx} are observed for spectra taken at spots near the sample edges. This suggests contributions for the tiny hysteresis loop from imperfections near the edge of the device. The RMCD curve for the odd layer device (**Fig. 7.4d** for 5SL-1) is similar to that for a freshly cleaved flake (see **Fig. 7.3f**). Unexpectedly, in the AFM state ($B < H_C$ ~3.8 T), both R_{yx} and the hysteresis loop nearly vanish (**Fig. 7.4 e**) despite the uncompensated magnetic moment and pronounced hysteresis resolved by RMCD. In addition, R_{xx} (**Fig. 7.4 e**) reaches a large value of about 7 h/e^2. Our results suggest that the AFM state ($|B| < H_C$) in both devices is a trivial magnetic insulator ($C = 0$) in which a small R_{yx} is

expected. We note that existing experimental works report different results regarding odd-even-layer-number devices [26–29]. This requires further investigation.

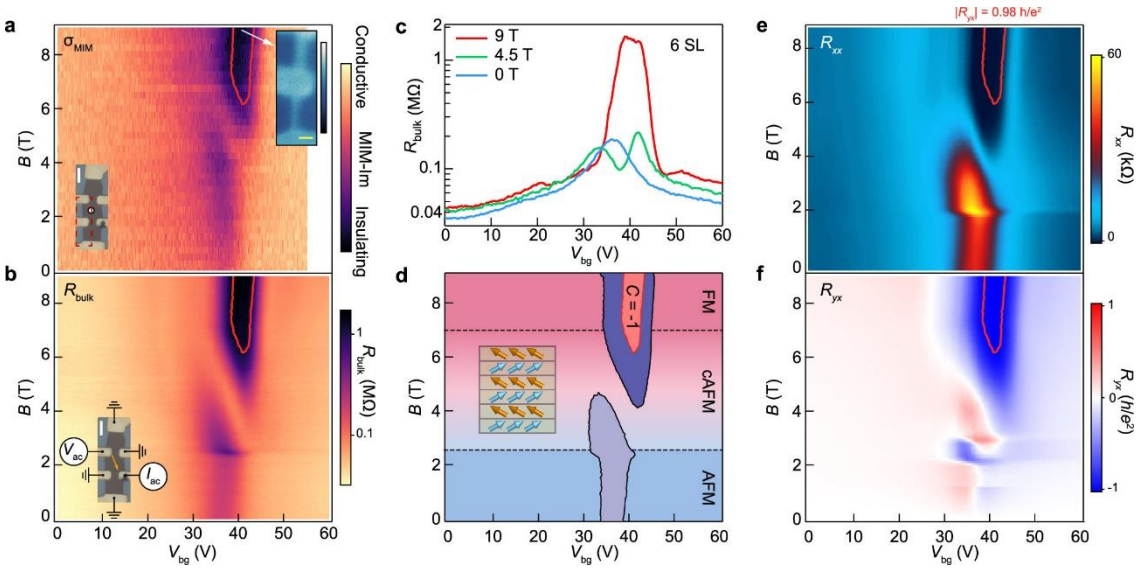

Figure 7.6 Probing band crossing during the topological phase transition and imaging of Chern gap in a 6 SL device. a, $V_{bg} - B$ maps of MIM − Im signal σ_{MIM} (**a**), bulk resistance R_{bulk} (**b**), longitudinal resistance R_{xx} (**e**), Hall resistance R_{yx} (**f**) and phase diagram of the topological transition (**d**). **c**, Selected data of R_{bulk} at $\mathrm{B} = 0, 4.5$ and 9 T, extracted from **b**. All for device 6SL-2. Scale bar is 2 um for the upper inset of (**a**) and 5 um for lower insets of (**a**) and (**b**). Adapted from REF 2, Copyright ACS.

7.4 Band Crossing and Topological Edge States During the Topological Phase Transition

Then we study how the bulk electronic structure evolves as the magnetic state is tuned. First, we use microwave impedance microscopy (MIM)[35] to probe the local conductivity of the sample bulk region. As demonstrated in another even layer sample (6SL-2), the MIM tip is parked near the center of the flake (~4 um away from the sample edges). Fig. 7.6a shows the intensity plot of the MIM − Im signal, σ_{MIM}, as a function of

[35] Refer to Chapter 2 for details on MIM measurements. Importantly, MIM − Im characterizes the local conductivity.

back gate voltage and magnetic field. In addition, we measure the bulk resistance, a $V_{bg} - B$ map of R_{bulk}, via transport using the configuration illustrated in the inset of **Fig. 7.6b**. A small AC voltage bias is applied between a pair of electrodes on the opposite of the Hall bar while grounding all other electrodes to eliminate edge conductions. The measured resistance from the two electrodes thus represents the sample bulk property. The two maps (σ_{MIM} and R_{bulk}) match well and demonstrate the robustness of our measurements on the bulk electronic properties. They both show resistive states at specific gate ranges both in the AFM ($B < 2$ T) and FM ($B > 6$ T) regimes, as shown as by the dark regions in the two maps. The fermi level of the bulk is tuned within the bulk energy gap in these resistive states, so a low (high) bulk conductance (resistance) is observed.

To correlate the bulk electronic structure with the topological order, the $V_{bg} - B$ maps of R_{yx} and R_{xx} are also measured and shown here (**Fig. 7.6f** and **7.6e**). These four maps show striking similarities which suggest a correspondence between the bulk electronic structure during the magnetic-field-induced topological phase transition. Compared with the Hall measurements, the insulating gap feature in the AFM state corresponds to the trivial insulator state ($C = 0$), implying its trivial topological nature. In contrast, the highly insulating feature in the FM state coincides with the gate range in which the quantized R_{yx} and vanishing R_{xx} are observed ($C = -1$). Overlaying the contour of R_{yx} at a threshold of 98% of $-h/e^2$ on all four maps displays an excellent correlation. The correlation marks the observation of the Chern insulator gap here.

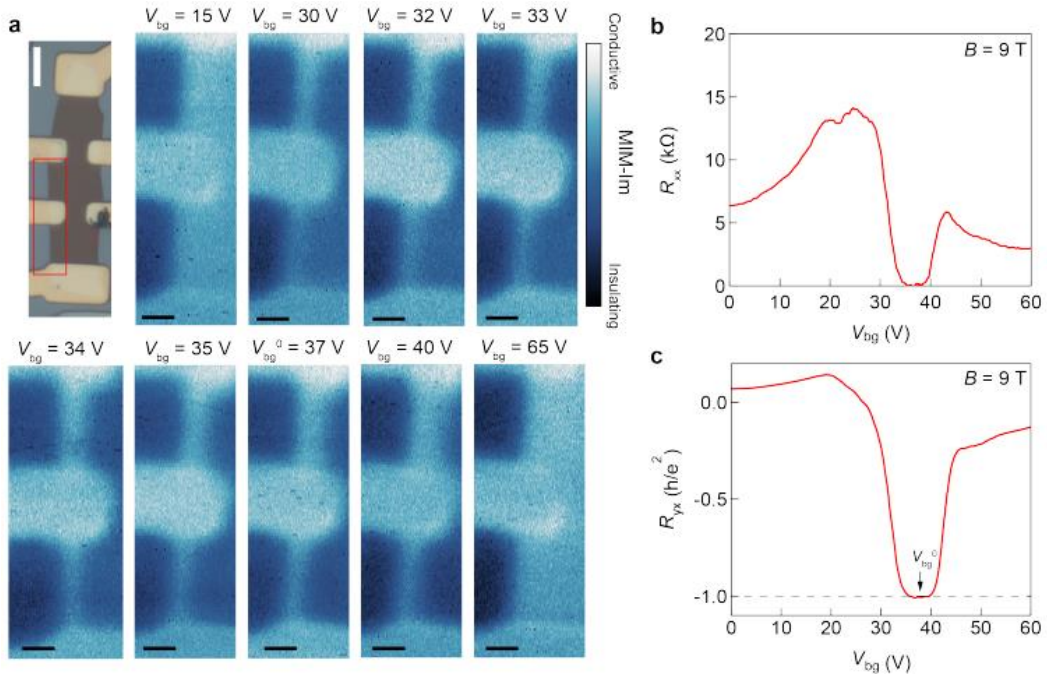

Figure 7.7 Evolution of edge states in 6SL-2 as a function of gate voltage. a, Optical image of 6SL-2 device and MIM images to demonstrate the evolution of edge states. The scan range is indicated by the red box. Scale bar is 5 um for the optical image and 2 um for the MIM images. **b**, **c**, R_{xx} and R_{yx} of 6SL-2 as a function of gate voltage at 3 K and 9 T. Adapted from REF 2, Copyright ACS.

To further support the Chern insulator state ($C = -1$), we performed a spatial MIM scan to image any topological edge conductions at 9 T with a temperature of 3 K. The scan range is shown in **Fig. 7.7a** which coves a sample edge with some metal contacts. The scan images are taken while the bulk carrier density is varied by the back gate. All scan images are calibrated using the metal-contact region as a high-conductance limit and the substrate region as a low-conductance limit[36]. With a small gate voltage, the sample is highly hole-doped and a large bulk conductance is observed as can be seen as a uniform and white sample region ($V_{bg} = 15$ V). When fermi level is tuned within the bulk energy gap

[36] See Chapter 2 for details on MIM analysis.

(V_{bg} ~30 − 40 V), the bulk becomes highly insulating with a low conductance (dark). However, the edge conduction is always high (bright) which indicates the existence of a topological edge states. When a large gate voltage is applied ($V_{bg} = 65$ V), the sample becomes electron-doped with a high bulk conductance restored. We notice some variation in the MIM-Im intensity map for the bulk regions which could be due to imhomogeneous local defect doping (the conductivity of upper bulk region is turned on before the lower part as can be seen in the scan at $V_{bg} = 40$ V of **Fig. 7.7a**). Thus, the series of spatial scan images at different back gate voltages clearly demonstrate the formation of a robust topological edge conduction in the $C = -1$ state.

Ther is a cAFM phase which connects the AFM trivial insulating state ($C = 0$) and the FM Chern insulator state ($C = -1$). From the σ_{MIM} and R_{bulk} maps, the gate regime for the $C = 0$ state starts to shrink when B increases above ~2 T. An incipient Chern insulator gap appears and increases (from Hall measurements, **Fig 7.6e** and **7.6f**) with a conductive state separating the two regimes. As B increases, one part of the conduction band from the AFM phase splits off and moves toward the bulk valance band. Eventually, this band branch crosses the entirely band gap and merges with the bulk valance band at B ~7 T in the FM phase. Meanwhile, the Chern insulator gap increases and eventually fully opens, accompanied by a gradually increasing R_{yx} to the quantized value of $-R_{yx}$ and a decreasing R_{xx} toward zero. The observation falls in the picture of band crossing process during a quantum phase transition which we draw a phase diagram in **Fig. 7.6d**. The canting of magnetic moment is responsible for the energy shift of the crossing energy band via

magnetic exchange interaction. We observe same band-crossing process in odd-layer devices with data shown in **Fig. 7.8**. Same analysis can be achieved.

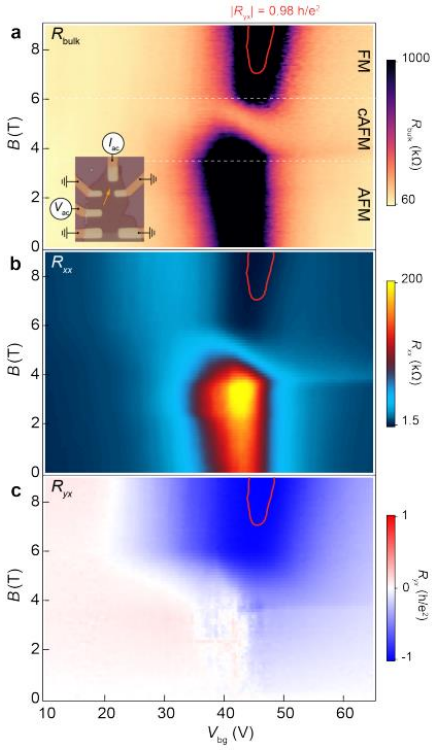

Figure 7.8 Band crossing during the topological phase transition in a 5-SL device. **a,** $V_{bg} - B$ maps of bulk resistance R_{bulk} (**a**), longitudinal resistance R_{xx} (**b**), Hall resistance R_{yx} (**c**), respectively. A contour of $R_{\mathrm{yx}} = 0.98\ {}^{h}/_{e^2}$ is overlaid for all three maps. Scale bar in the inset of (**a**) is 5 um. All data here are for device 5SL-1 at 2 K. Adapted from REF 2, Copyright ACS.

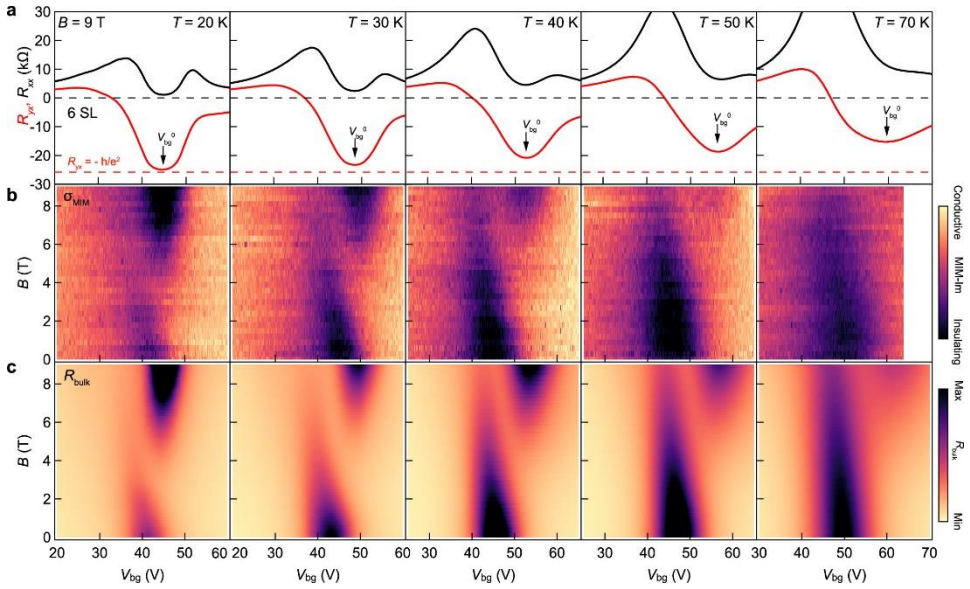

Figure 7.9 Temperature dependence of the band crossing and Chern insulator state. a, Longitudinal resistance R_{xx} and Hall resistance R_{yx} as a function of gate voltage at B = 9 T and selected temperatures. Corresponding $V_{bg} - B$ maps of MIM − Im signal σ_{MIM} (**b**), bulk resistance R_{bulk} (**c**). All data are from device 6SL-2. Adapted from REF 2, Copyright ACS.

Finally, we investigate the temperature dependence of the band crossing process and Chern insulator gap. Example data are shown for the 6SL-2 device (Fig. 7.9). The Néel temperature (T_N) below which the magnetic order starts to develop is determined to be around ~23 K (shown in **Fig. 7.11**). Fig. 7.9a shows the R_{yx} and R_{xx} at selected temperatures. σ_{MIM} and R_{bulk} are shown in Fig. 7.9b and 7.9c. The correspondent spin-flop B-field above which the band crossing process starts is changing to higher values as can be seen by a gradual shift of the overall patterns at these temperatures. For example, at 30 K, the splitting of the conduction band starts at a higher B field. At 9 T, the crossing band touches the bulk valance band without a complete merge. A close-to-quantization region is observed in which R_{yx}~0.9 h/e^2 and R_{xx} remains low (see transport data at 30 K in Fig. 7.9a), indicating the persistence of the chiral edge state. At 40 K, the close-to-

quantization region shrinks further with a maximum R_{yx}~0.8 $^{h}/_{e^2}$ with a barely touched crossing band at 9 T. To visualize the edge state evolution, we perform MIM line-scan across a sample edge as indicated by the arrow in **Fig. 7.10** at 9 T at different temperatures. As the gate voltage changes the conductance of bulk region, the contrast between sample edge and bulk shows up when fermi level is tuned within bulk energy gap. This contrast gradually decreases when temperature is increased. Same as our analysis from the R_{yx} at different temperatures. The large Hall angle R_{yx}/R_{xx} at temperatures above T_N is similar to a recent report [29], which is consistent with the observed incipient but not fully developed Chern insulator gap. For T = 50 K and above, R_{yx} significantly deviates from the quantized value and the crossing branch is completely detached from the bulk valence band at 9 T. The contrast between the edge and bulk regions are hard to resolve.

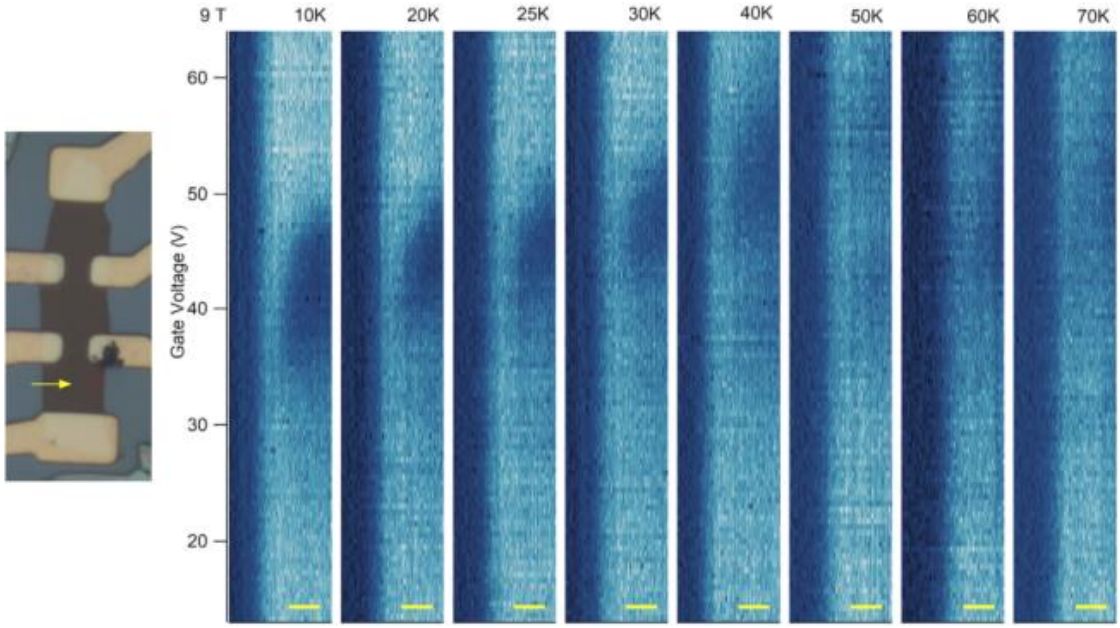

Figure 7.10 Temperature dependence of MIM-Im line scans at B = 9 T in device 6SL-2. Line-scan images at selected temperatures along the direction indicated by the arrows in the optical image (left). At each temperature, repeated line scans are performed (x-axis as the spatial position) while the gate voltage is varied (y-axis). Scale bars: 2 um. Adapted from REF 2, Copyright ACS.

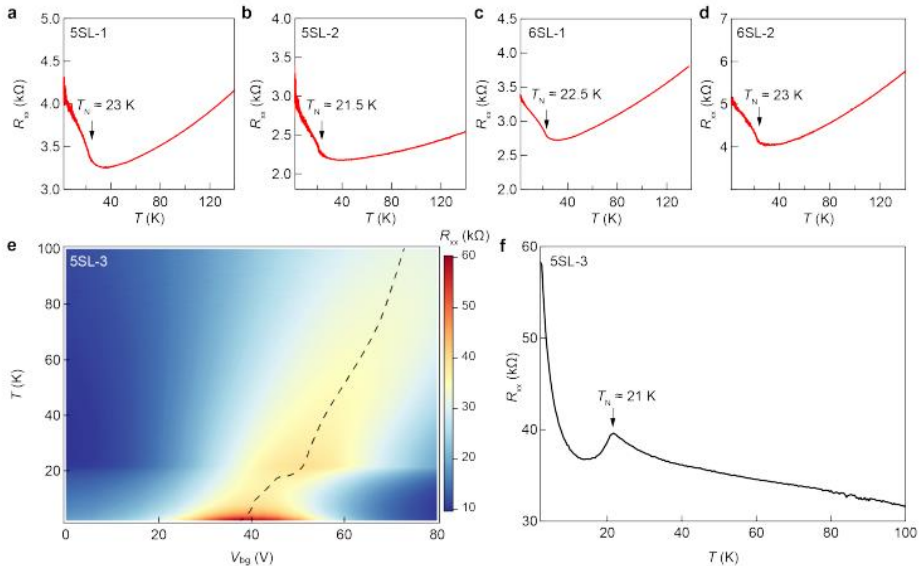

Figure 7.11 Determination of Néel temperature TN from transport measurements. a-d, Longitudinal resistance R_{xx} as a function of temperature for all the devices (labeled). Kinks around 21-23 K indicate the transition temperature from paramagnetic to antiferromagnetic state. **e**, R_{xx} for as a function of temperature and back gate voltage for device 5SL-3. **f**, Temperature dependent R_{xx} extracted at the charge neutral point as indicated by the dashed line in (**e**). All data are taken at 0 T. Adapted from REF 2, Copyright ACS.

Our results suggest that below the Néel temperature, the FM ordered magnetic moments induce a large exchange interaction in a conduction sub-band, which fully crosses the bulk valance band at high field (above 7 T), leading to a robust Chern insulator gap. While the long-range ordering of Mn moments disappears at temperatures slightly above Néel temperature, sufficiently large magnetic field can still align these Mn moments to introduce an incipient Chern insulator state, albeit one much weaker that the state existing below the Néel temperature. To achieve a comprehensive understanding of the topological physics in this new Chern magnet, it is necessary to combine measurements of local and bulk electronic properties with a careful examination of the magnetic states. With a multitude of possible topological phases and magnetic orders in $MnBi_2Te_4$, our work paves

the way toward a full realization of their potential as a platform to study topological phase transitions and to engineer Chern numbers in Chern insulators via external control knobs.

References

[1] T. Li et al., *Quantum Anomalous Hall Effect from Intertwined Moiré Bands*, Nature **600**, 641 (2021).

[2] D. Ovchinnikov et al., *Intertwined Topological and Magnetic Orders in Atomically Thin Chern Insulator MnBi2Te4*, Nano Lett. **21**, 2544 (2021).

[3] K. V. Klitzing, G. Dorda, and M. Pepper, *New Method for High-Accuracy Determination of the Fine-Structure Constant Based on Quantized Hall Resistance*, Phys. Rev. Lett. **45**, 494 (1980).

[4] M. Z. Hasan and C. L. Kane, *Colloquium: Topological Insulators*, Rev. Mod. Phys. **82**, 3045 (2010).

[5] P. Wang, J. Ge, J. Li, Y. Liu, Y. Xu, and J. Wang, *Intrinsic Magnetic Topological Insulators*, Innov. **2**, 100098 (2021).

[6] C. L. Kane and E. J. Mele, *Z2 Topological Order and the Quantum Spin Hall Effect*, Phys. Rev. Lett. **95**, 3 (2005).

[7] C. L. Kane and E. J. Mele, *Quantum Spin Hall Effect in Graphene*, Phys. Rev. Lett. **95**, 1 (2005).

[8] M. König, S. Wiedmann, C. Brüne, A. Roth, H. Buhmann, L. W. Molenkamp, X. Qi, and S. Zhang, *Quantum Spin Hall Insulator State in HgTe Quantum Wells*, Science (80-.). **318**, 766 (2007).

[9] I. Knez, R.-R. Du, and G. Sullivan, *Evidence for Helical Edge Modes in Inverted <math Display="inline"> <mi>InAs</Mi> <mo>/</Mo> <mi>GaSb</Mi> </Math> Quantum Wells*, Phys. Rev. Lett. **107**, 136603 (2011).

[10] S. Tang et al., *Quantum Spin Hall State in Monolayer 1T'-WTe 2*, Nat. Phys. **13**, 683 (2017).

[11] S. Wu, V. Fatemi, Q. D. Gibson, K. Watanabe, T. Taniguchi, R. J. Cava, and P. Jarillo-Herrero, *Observation of the Quantum Spin Hall Effect up to 100 Kelvin in a Monolayer Crystal*, Science (80-.). **359**, 76 (2018).

[12] Z. Fei, T. Palomaki, S. Wu, W. Zhao, X. Cai, B. Sun, P. Nguyen, J. Finney, X. Xu, and D. H. Cobden, *Edge Conduction in Monolayer WTe 2*, Nat. Phys. **13**, 677 (2017).

[13] Y. Xia et al., *Observation of a Large-Gap Topological-Insulator Class with a Single Dirac Cone on the Surface*, Nat. Phys. **5**, 398 (2009).

[14] Y. L. Chen et al., *Experimental Realization of a Three-Dimensional Topological Insulator, Bi 2 Te 3*, Science (80-.). **325**, 178 (2009).

[15] F. D. M. Haldane, *Model for a Quantum Hall Effect without Landau Levels: Condensed-Matter Realization of the "Parity Anomaly,"* Phys. Rev. Lett. **61**, 2015 (1988).

[16] C. Z. Chang et al., *Experimental Observation of the Quantum Anomalous Hall Effect in a Magnetic Topological Insulator*, Science (80-.). **340**, 167 (2013).

[17] M. Mogi, R. Yoshimi, A. Tsukazaki, K. Yasuda, Y. Kozuka, K. S. Takahashi, M. Kawasaki, and Y. Tokura, *Magnetic Modulation Doping in Topological Insulators toward Higher-Temperature Quantum Anomalous Hall Effect*, Appl. Phys. Lett. **107**, (2015).

[18] I. Lee et al., *Imaging Dirac-Mass Disorder from Magnetic Dopant Atoms in the Ferromagnetic Topological Insulator Cr x (Bi 0.1 Sb 0.9) 2-x Te 3*, Proc. Natl. Acad. Sci. **112**, 1316 (2015).

[19] M. M. Otrokov et al., *Highly-Ordered Wide Bandgap Materials for Quantized Anomalous Hall and Magnetoelectric Effects*, 2D Mater. **4**, (2017).

[20] Y. Gong et al., *Experimental Realization of an Intrinsic Magnetic Topological Insulator*, Chinese Phys. Lett. **36**, (2019).

[21] M. M. Otrokov et al., *Prediction and Observation of an Antiferromagnetic Topological Insulator*, Nature **576**, 416 (2019).

[22] K. He, *MnBi2Te4-Family Intrinsic Magnetic Topological Materials*, Npj Quantum Mater. **5**, 2 (2020).

[23] M. M. Otrokov, I. P. Rusinov, M. Blanco-Rey, M. Hoffmann, A. Y. Vyazovskaya, S. V. Eremeev, A. Ernst, P. M. Echenique, A. Arnau, and E. V. Chulkov, *Unique Thickness-Dependent Properties of the van Der Waals Interlayer Antiferromagnet MnBi2Te4 Films*, Phys. Rev. Lett. **122**, 107202 (2019).

[24] D. Zhang, M. Shi, T. Zhu, D. Xing, H. Zhang, and J. Wang, *Topological Axion States in the Magnetic Insulator MnBi2Te4 with the Quantized Magnetoelectric Effect*, Phys. Rev. Lett. **122**, 206401 (2019).

[25] J. Li, Y. Li, S. Du, Z. Wang, B. L. Gu, S. C. Zhang, K. He, W. Duan, and Y. Xu, *Intrinsic Magnetic Topological Insulators in van Der Waals Layered MnBi2Te4-Family Materials*, Sci. Adv. **5**, 1 (2019).

[26] Y. Deng, Y. Yu, M. Z. Shi, Z. Guo, Z. Xu, J. Wang, X. H. Chen, and Y. Zhang, *Quantum Anomalous Hall Effect in Intrinsic Magnetic Topological Insulator MnBi2Te4*, Science (80-.). **367**, 895 (2020).

[27] C. Liu, Y. Wang, H. Li, Y. Wu, Y. Li, J. Li, K. He, Y. Xu, J. Zhang, and Y. Wang, *Robust Axion Insulator and Chern Insulator Phases in a Two-Dimensional Antiferromagnetic Topological Insulator*, Nat. Mater. **19**, 522 (2020).

[28] C. Liu et al., *Magnetic-Field-Induced Robust Zero Hall Plateau State in MnBi2Te4 Chern Insulator*, Nat. Commun. **12**, 6 (2021).

[29] J. Ge, Y. Liu, J. Li, H. Li, T. Luo, Y. Wu, Y. Xu, and J. Wang, *High-Chern-Number and High-Temperature Quantum Hall Effect without Landau Levels*, Natl. Sci. Rev. **7**, 1280 (2020).

[30] S. Yang et al., *Odd-Even Layer-Number Effect and Layer-Dependent Magnetic Phase Diagrams in MnBi2Te4*, ArXiv **011003**, 1 (2020).

[31] B. Huang et al., *Layer-Dependent Ferromagnetism in a van Der Waals Crystal down to the Monolayer Limit*, Nature **546**, 270 (2017).

Chapter 8 Outlook

In conventional MIM study of 2D materials, tip "talks" to the sample through microwave radiation since all the protective capping layers are "transparent" (very insulating). There lacks a top gate electrode, and the only tuning parameter is the carrier density for the sample besides temperature and magnetic field. In Chapter 6, we report a newly designed experimental setup which enables us to employ a new tuning parameter—electric displacement field. The system we want to study is a dual-gate device and an electric displacement field can be used to tune the relative energy bands in the different layers (see Fig. 8.1). Two independent parameters can be tuned, the total carrier density and the applied displacement field. An example is the Mott insulating state will be observed as a continuous line feature (fixed carrier density).

In this device with a metallic top gate, we use monolayer graphene with reduced conductivity compared to bulk metal or thick graphite layers. An external magnetic field can be applied to further reduce the conductivity. Microwave electric field can penetrate this "semi-transparent" top graphene layer and the impedance contribution of the sample could be probed. Then a MIM map of the sample will be measuring the impedance with contributions from both the top graphene and the buried sample. An expected data will be shown in the right panel of Fig. 8.1. Since the carrier density of the top graphene layer is determined by the top gate voltage and the chemical potential of the sample, we could predict that the LLs (when B field is applied) will primarily depend on the top gate voltage since the change of chemical potential of sample is small compared with top gate voltage. Thus, it should be easy to distinguish two contributions of impedance and then one can

focus on effect that the applied electric field brings to the sample. One straightforward example is to check whether this applied displacement field could cause any modulation of the moiré potential. In this way, the correlation strength could be tuned to see if a metal-to-insulator transition exists.

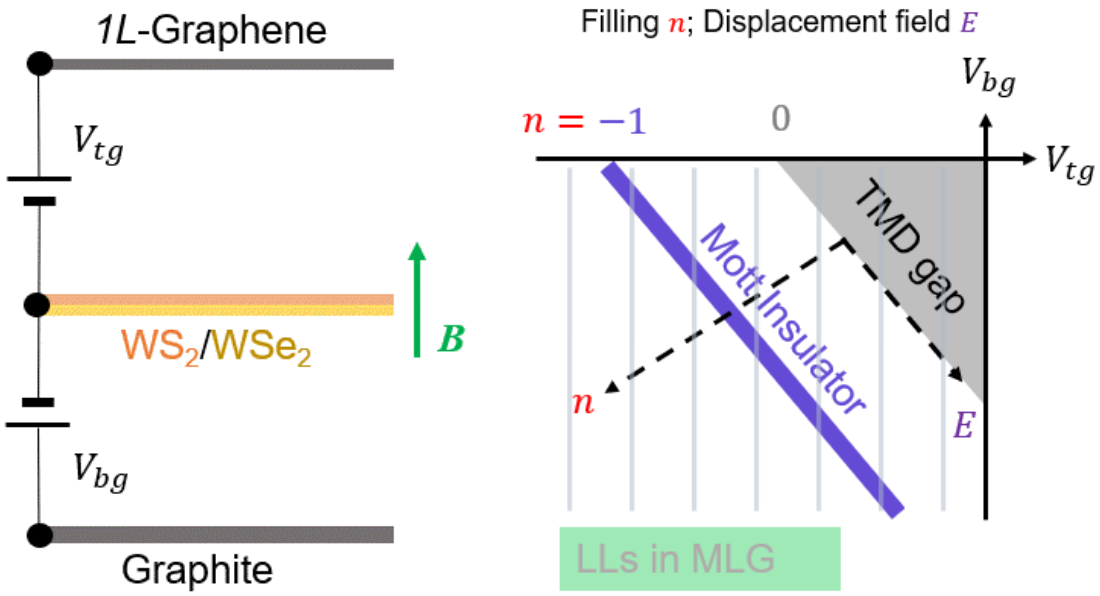

Figure 8.1 Dual-gate device structure for MIM study. Left, a dual-gate WS_2/WSe_2 moiré superlattice. Specifically, we use a monolayer graphene as the top gate material. **Right**, the phase diagram (carrier density and displacement field) for the dual-gate moiré superlattice. Landau levels (LLs) will form in the graphene and show as vertical lines (see analysis in the maintext).